Estimation and assessment of differential and specific differential phase with the IDRA X-band Doppler polarimetric radar

Sotirios Georgiou

IRCTR, Delft University of Technology
June 2010

Thesis Committee
Prof. Dr. H.W.J. Russchenberg
Prof. Dr. F. Le Chevalier
Dr. H. Leijnse
MSc. C.M.H. Unal

Contents

Acknowledgments

I am grateful that my choice to work on my MSc thesis within the ATMOS/IRCTR group was proven to be a much satisfactory and rewarding experience. Therefore, I wish to express my deep appreciation and thankfulness equally to all the members of the ATMOS group for providing me with an exemplary scientific and work environment. Furthermore, I would like to mention those that were kind enough to supervise or provide direct assistance to my project:

- **Herman Russchenberg**, for the trust he showed in my abilities by assigning me this project and his kind patience and encouragement.
- **Christine Unal**, for her extended supervision and scientific support which I personally value as mentorship. I am personally indebted to her genuine interest to provide assistance during the whole duration and under all circumstances, as if the first day. Also, for her thorough and discerning review of my present report.
- **Jordi Figueras i Ventura**, for making my project available through his successful PhD work on IDRA, his supervision, and providing me with documents and software material in perfect condition which was an inspiration for setting my own standards.
- **Tobias Otto**, for his guidance and effort to compile and maintain the FIM Matlab toolbox without which the present report would be missing chapters 6 and 7 altogether.

Reaching the end of my project, I deeply appreciate all the kind of knowledge and experience I gained through my work. On the other hand, I feel disappointed as I also realized my shortcomings, on which I did not improve to the extend I wish. I can only accept this as a factor of motivation for all my future work, hoping to reach the same level of competency and maturity as my past and present teachers.

Chapter 1

Introduction

The issue of climate change is steadily becoming of increased concern due to its critical implications. The earth's ecosystem is constantly irradiated by the sun and a part of this incoming power is reflected by the atmosphere before even reaching the surface, while another part is reflected back afterwards; the rest remains within the ecosystem. In other words, the earth's ecosystem can be thought of as an open system characterized by a radiative balance at its boundary. The actual point of the equilibrium is set by all the factors that affect the absorption and reflection of the incoming sun power. The composition and characteristics of clouds and atmosphere, which define the boundary, is obviously the key point. This can be further analyzed in individual components as shown in Fig. 1.1. The **radiative forcing** expresses the contribution to the thermal budget, with positive values imply warming of the earth system. Regarding aerosols, there is uncertainty not only as to the actual magnitude of their radiative forcing but the underlying physical mechanisms as well. It could be said that there is indication that they could very well affect the thermal equilibrium significantly, yet there is limited knowledge on how this takes place thus any prediction is difficult. It is apparent that some effort should be focused on that direction so that more knowledge on their physical interaction is obtained.

IDRA (IRCTR drizzle radar) is a X-band Doppler polarimetric radar that was designed in this context. More information about IDRA and its objectives can be found in [1] and [2] while detailed technical information is available in [3]. IDRA is located in Cabauw, the Netherlands, where there are installed many other observation instruments allowing for synergy. The main objective is the observation of drizzle, through which conclusions upon the aerosol effects can be drawn [4]. In particular, the presence of aerosols is pronounced at the Cabauw site due to the industrial areas nearby, and their spatial concentration can be monitored by installed sensors. On the other hand, IDRA is able to monitor the spacial distribution of drizzle at a local scale; by studying the statistics of these two kind of measurements over a long time frame, the mechanism of their relationship may be understood. Next to this climate objective, IDRA was designed for the characterization of precipitation at small temporal and space scale from drizzle to heavy precipitation. IDRA has been in operation since April 2008 and apparently a good understanding of its products and performance is essential prior to attempting studies closely relevant to its objectives; precipitation and aerosol effect observation is not a straightforward procedure

as it involves long-term detailed measurements. This sets the context of the current thesis: although no mention is given to the climatic objective of IDRA, the estimation and assessment of the polarimetric observables Φ_{dp} and K_{dp} in the current state is the next step towards understanding and qualifying IDRA performance. Moreover, these observables are directly related to rain rate estimation which falls well within the extended IDRA objectives and intended use. Therefore, it is hoped that the current work will contribute to an increased body of knowledge regarding IDRA, which once being complete will allow for further atmospheric studies.

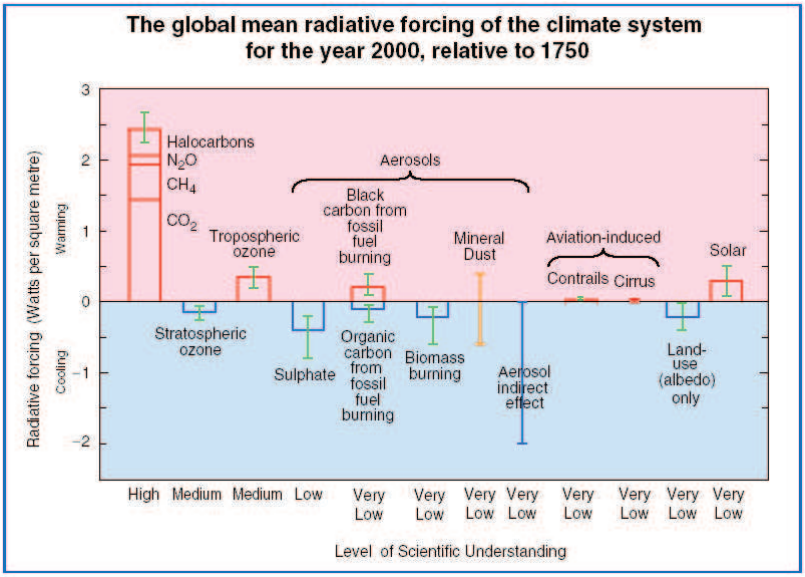

Figure 1.1: The radiative forcing of various factors. Regarding aerosols, there is great uncertainty as to the magnitude of their contribution combined with low understanding of the underlying mechanisms (source: IPCC, Working Group I, Summary for Policy Makers, figure 3).

With the previous in mind, it is now stated that the objective of this thesis is to discuss the estimation of the **differential phase** (Φ_{dp}) and **specific differential phase** (K_{dp}) based on IDRA data, with a view to their usefulness for rain estimation. Being phase-based observables in contrast to the amplitude-based and more commonly used Z and Z_{dr}, they present valuable advantages such as independence from absolute calibration errors and attenuation effects. For this reason, it comes as no surprise that K_{dp} is needed in order to apply a rain rate estimation relationship as accurate as possible and Φ_{dp} is key for attenuation correction schemes. On the other hand, Φ_{dp} was attempted to be estimated with a spectral polarimetry approach in contrast to the established time-domain method. Above all, emphasis was given on explaining and understanding the expected and obtained results from a physical point of view in order to gain integrated confidence in all the products of IDRA, which is necessary for the progressive study of meteorological phenomena.

In Chapter 2 an essential theoretical background is given mainly about Φ_{dp} and K_{dp}, so that the discussion in Chapters 3 and 4 dealing with their estimation

can be clearly understood. In Chapter 5, two case studies are discussed in detail while the next one focuses on the assessment of the obtained results. Finally, in Chapter 7 the issue of attenuation, which is expected to affect X-band radars, is addressed. Additional material is included in the appendices.

Chapter 2

Theoretical Background

A monostatic radar emits electromagnetic waves towards a medium that are subsequently scattered in all directions. Backscattered waves are propagated in the opposite direction towards the radar and received by it. The backscattered signal is referred to as the echo of the medium. By studying the signal characteristics of the echo, such as its power, a variety of conclusions can be drawn regarding the medium itself. In short, a radar is a tool for observing media by distance by analyzing the received echoes; this is the concept of remote sensing applications.

In the case of a weather radar, the medium is the atmosphere and the scattering occurs due to the particles contained in it (rain drops, hail stones etc). The objective is acquiring information such as the composition of the atmosphere in terms of particles, their dimensions, their velocities etc. This information is essential either for weather forecasting or for general studies on the behavior and progressive changes of the atmosphere.

A detailed theoretical treatment for weather radars is available in [5]. The limited theoretical information given here pertains only to the kind of measurements and studies conducted and presented in the following chapters so that they can be clearly understood. But before that, it is useful to expand on two key terms relevant to IDRA: the Doppler radar and the polarimetric radar:

- a **Doppler radar** exploits the Doppler frequency shifting phenomenon. The scattered electromagnetic waves are of the same frequency as the transmitted ones. However, if the radar and the medium are in relative motion then the received echo will be shifted in frequency, depending on the relative radial velocity. For horizontally profiling weather radars, the relative velocity is due to the motion of the atmospheric particles by local wind or turbulence. In other words, the velocity of the particles is translated into frequency shifting and vice versa. The advantage of Doppler radars is that they offer additional information on the velocities of the particles which is essential for dynamic studies. On the other hand, this entails that the received signal is no longer monochromatic (assuming the transmitted was) so it can be filtered in the frequency domain, or equivalently the domain of particle velocities. This is useful for clutter suppression since the unwanted clutter signal comes in the most cases from stationary targets of zero velocity, while the desired signal originated from

the particles is frequency shifted.

- a **polarimetric radar** transmits pulses of different polarization (usually horizontal and vertical). This is motivated by the anisotropy of the precipitation medium; since the particles are not spherical, processing their echoes for different polarizations provides extended information on their microphysical properties.

- a Doppler polarimetric radar utilizes both mechanisms and provides the particle velocities along with information as to their anisotropic characteristics. IDRA is an example of such a radar.

2.1 Derivation of Φ_{dp} and K_{dp}

In this section, the derivation for the radar observables **differential phase** (Φ_{dp}) and **specific differential phase** (K_{dp}) is given (based on [5], Chapter 4). They are first derived for simple, ideal cases that are progressively generalized in order to end up with a realistic model of the **radar resolution volume** which is the part of the atmospheric volume that collectively scatters a certain transmitted pulse.

We begin with the case where the medium is simply a collection of identical spherical particles. It can be shown ([5], p21) that the medium can be considered as being equivalent to a homogeneous medium of **effective wave number** k_{eff}, where $Im(k_{eff})$ is the **attenuation constant** affecting the attenuation of the amplitude of the electromagnetic wave, $Re(k_{eff})$ is the **propagation constant** affecting the rate of phase change and k_{eff} itself is an eigenvalue from a mathematical point of view (Eq. 2.1, 2.2). If the particles are spheroid instead of spherical and their **canting angle** is zero, meaning that their axis of revolution is vertical with respect to the earth surface, the medium they comprise becomes anisotropic as to the horizontal and vertical plane. In other words, a wave polarized in a direction which belongs in one of these polarization planes will encounter different effective wave numbers, k^h_{eff} and k^v_{eff} respectively, as the h-polarized wave 'sees' a different medium than the v-polarized. The propagation of a linearly horizontally polarized and a linearly vertically polarized plane wave can be described by Eq. 2.3 which has the solution given in Eq. 2.4, where $\lambda_1 = -jk^h_{eff}$ and $\lambda_2 = -jk^v_{eff}$.

$$\vec{E} = \hat{e}E_0 \exp(-jk_{\text{eff}}z) \tag{2.1}$$

$$\frac{d\vec{E}}{dz} = (-jk_{\text{eff}})\vec{E} \tag{2.2}$$

$$\frac{d}{dz}\begin{bmatrix} E_h \\ E_v \end{bmatrix} = \begin{bmatrix} -jk^h_{\text{eff}} & 0 \\ 0 & -jk^v_{\text{eff}} \end{bmatrix}\begin{bmatrix} E_h \\ E_v \end{bmatrix} \tag{2.3}$$

$$\begin{bmatrix} E_h(z) \\ E_v(z) \end{bmatrix} = \begin{bmatrix} e^{\lambda_1 z} & 0 \\ 0 & e^{\lambda_2 z} \end{bmatrix}\begin{bmatrix} E_h(0) \\ E_v(0) \end{bmatrix} = \begin{bmatrix} T_{\text{l1}} & 0 \\ 0 & T_{22} \end{bmatrix}\begin{bmatrix} E_h(0) \\ E_v(0) \end{bmatrix} \tag{2.4}$$

The differential behavior of the medium can be expressed quantitatively by considering the difference between the phase constants for each polarization, taking into account that $\mathrm{Im}(\lambda) = -Re(\mathrm{k}_{eff})$. This gives rise to **specific differential phase** K_{dp} $[radkm^{-1}]$ defined as[1]:

$$K_{\mathrm{dp}} = -(10^3)\mathrm{Im}(\lambda_1 - \lambda_2) \tag{2.5}$$

An important conclusion from Eq. 2.4 is that since the **transmission matrix T** is diagonal, the h-polarized and the v-polarized waves remain uncoupled: transmission of an h-polarized wave will not generate at any point within the medium a v-polarized wave and vice versa.

If we now consider the generalization for a **polydisperse** distribution of particles (meaning that they can be of different size, shape, orientation, phase etc) it was shown ([6]) that again the medium can be mathematically described by two eigenvalues as before. Eq. 2.3 is now replaced by Eq. 2.6, which involves the elements of a matrix **P** defined in Eq. 2.7. The essence of the Oguchi's solution, as it is called, is that a polydisperse distribution of particles implies that each particle may have its own scattering matrix[2] according to its own state, but they are all accounted for by **ensemble averaging** over them as denoted by the $< . >$ operator.

$$\frac{d}{dz}\begin{bmatrix} E_h(z) \\ E_v(z) \end{bmatrix} = \begin{bmatrix} -jk_0 + P_{hh} & P_{hv} \\ P_{vh} & -jk_0 + P_{vv} \end{bmatrix}\begin{bmatrix} E_h(z) \\ E_v(z) \end{bmatrix} \tag{2.6}$$

$$\mathrm{P} = -j\frac{2\pi}{k_0}\langle n\mathrm{S}_{\mathrm{FSA}}(\hat{i},\hat{i})\rangle \tag{2.7}$$

In the above equation, k_0 is the complex wave number of the material (here assumed to be vacuum), n is the concentration of the particles, and $S_{FSA}(\hat{i},\hat{i})$ is the scattering matrix in the forward direction under the FSA convention. Eq. 2.6 has a solution of the form of Eq. 2.8 where the transmission matrix T is now non-diagonal. The importance of the non-diagonal elements is that they give rise to coupling of the h- and v-polarized modes: an h-polarized transmitted wave will generate a v-polarized echo and vice versa. These types of echoes are called **cross-polar** in contrast to **co-polar** ones.

$$\begin{bmatrix} E_h(z) \\ E_v(z) \end{bmatrix} = \begin{bmatrix} T_{hh} & T_{hv} \\ T_{vh} & T_{vv} \end{bmatrix}\begin{bmatrix} E_h(0) \\ E_v(0) \end{bmatrix} \tag{2.8}$$

Even though the model of medium is realistic since it allows for any type and number of particles (provided that it remains 'sparse'), the analysis so far is only relevant to the propagation of a wave through the medium. In the case of the radar, there is transmission and reception and the process is described by the **radar equation** (Fig. 2.1, Eq. 2.9).

$$\begin{bmatrix} V_h \\ V_v \end{bmatrix} = \frac{\lambda G}{4\pi r^2}[\mathrm{T}][\mathrm{S}_{\mathrm{BSA}}][\mathrm{T}]\begin{bmatrix} M_h \\ M_v \end{bmatrix} \tag{2.9}$$

In Eq 2.9, M_h and M_v are the transmitted voltages at the h and v port respec-

[1] as defined above, K_{dp} is positive for oblate particles which is actually the expected shape of rain drops

[2] the scattering matrix completely describes a particle's interaction with the transmitted electromagnetic field

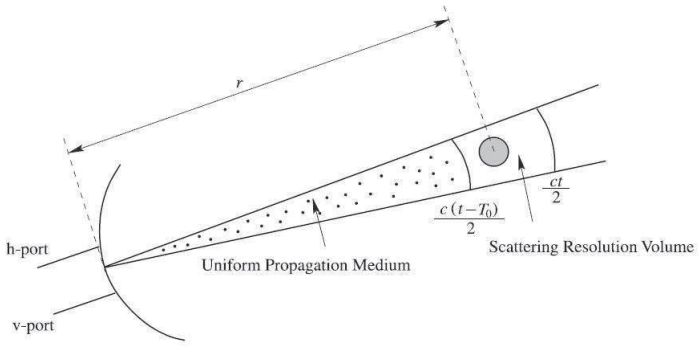

Figure 2.1: Scattering of the radar beam by a target in the resolution volume, which is preceded by the propagation medium ([5], p177).

tively and Vh and V_v the received ones. The transmission matrix [T] accounts for the two-way propagation through the medium[3] while the scattering matrix [S] characterizes the target (in general the radar resolution volume). In this case, in order to express the scattering matrix the BSA convention is used instead. Let us assume that the medium is composed of **oriented spheroids** (zero canting angle). In this case, it can be shown ([5],p173) that

$$T = \begin{bmatrix} e^{\lambda_1 z} & 0 \\ 0 & e^{\lambda_2 z} \end{bmatrix} \tag{2.10}$$

Also, let us assume that the scattering matrix of the target is diagonal:

$$\mathrm{S_{BSA}} = \begin{bmatrix} S_{hh} & 0 \\ 0 & S_{vv} \end{bmatrix} = e^{j\delta_{hh}} \begin{bmatrix} |S_{hh}| & 0 \\ 0 & |S_{vv}|e^{j(\delta_{vv}-\delta_{hh})} \end{bmatrix} \tag{2.11}$$

If we consider the transmission of an h-pulse ($M_h = 1, M_v = 0$) then the received voltage at the h-port is

$$V_h^{10} = \frac{\lambda G}{4\pi r^2} e^{2\lambda_1 r} S_{hh} \quad , \tag{2.12}$$

while upon transmission of a v-pulse ($M_h = 0, M_v = 1$) the received voltage at the v-port is

$$V_v^{01} = \frac{\lambda G}{4\pi r^2} e^{2\lambda_2 r} S_{vv} \quad . \tag{2.13}$$

The argument of their product takes the following form, recalling Eq. 2.5 and that $\lambda = -jk_{eff}^h$:

$$\begin{aligned} \arg[(V_h^{10})^*(V_v^{01})] = \Psi_{\mathrm{dp}} &= \arg[e^{2(\lambda_2-\lambda_1)r}] + \arg(S_{hh}^* S_{vv})_{\mathrm{BSA}} \\ &= 2K_{\mathrm{dp}} r + \delta_{\mathrm{co}} = \Phi_{\mathrm{dp}} + \delta_{\mathrm{co}} \end{aligned} \tag{2.14}$$

In the above equation, the following terms appear:

1. the **total differential phase** Ψ_{dp} [deg] being the addition of

[3]assumed uniform so it may be represented by a constant [T]

2. the **differential propagation phase** (Φ_{dp}, [deg]), being the two-way range integral of K_{dp} (Φ_{dp}=2K_{dp}r), and

3. the **differential scattering phase** (δ_{co}, [deg])

Eq. 2.14 is fundamental because it shows clearly the interrelationship of all the above terms. At this point, some basic characteristics of the two components of Ψ_{dp} are given.

- Φ_{dp} and δ_{co} differ in one important aspect: Φ_{dp} is due to *propagation* through the medium while δ_{co} originates in the resolution volume (target) itself and only. This means that δ_{co} is not a cumulative function with respect to the range as opposed to Φ_{dp}, so it may change abruptly from rain cell to rain cell. This property will be recalled later trying to separate them, so that only Φ_{dp} is left which is connected directly to the desired K_{dp}.

- If δ_{co} is zero, then Ψ_{dp}=Φ_{dp}. However, δ_{co} is only zero for scattering under the Rayleigh approximation and non-zero for the Mie solution, as it can be seen by inspection of the respective scattering matrices. For X-band, the Rayleigh approximation is no longer valid as the size of the rain drops (0.2-8mm in equivolumetric diameter) become significant compared to the wavelength (for IDRA λ=3.2cm). Hence, δ_{co} cannot be ignored in principle and Ψ_{dp} is not equal to Φ_{dp}.

- It is useful to underline that the nature of δ_{co} is deterministic rather than random. As it has been said, δ_{co} 'sits' on top of the desired Φ_{dp} range profile thus biasing the subsequent estimation of K_{dp}. Regarding K_{dp} estimation it presents itself as a noisy signal, however this does not mean that δ_{co} is random in nature; it can be completely defined in terms of the drop size distribution, and rain cells having identical distributions will always result in the same δ_{co} [4]. If the drop size distribution is somehow known then δ_{co} will be known as well.

We now consider generalizations over the simplifications assumed. First of all, the radar resolution volume is not expected to contain only one target of diagonal scattering matrix [S]; in reality it contains a distribution of particles which can be described by a general, non-diagonal scattering matrix [S] being the ensemble average of the individual ones. In this case, Eq. 2.9 becomes

$$\begin{bmatrix} V_h \\ V_v \end{bmatrix} = \frac{\lambda G}{4\pi r^2} \begin{bmatrix} S_{hh}e^{2\lambda_1 r} & S_{hv}e^{(\lambda_1+\lambda_2)r} \\ S_{vh}e^{(\lambda_1+\lambda_2)r} & S_{vv}e^{2\lambda_2 r} \end{bmatrix} \begin{bmatrix} M_h \\ M_v \end{bmatrix}$$

It is obvious that regarding arg$[(V_h^{10})^*(V_v^{01})]$, it is the same as before so the previous conclusions apply in this generalized case as well; the propagation medium expressed by λ_1 and λ_2 will result in Φ_{dp}, being the two-way integral of K_{dp}, and the resolution volume will result in the δ_{co} on top of Φ_{dp}. The difference lies only in the cross-polar products which are not of our concern. Secondly, in reality the propagation path is seldom homogeneous so that it can be described in its whole range by a single transmission matrix [T]. However,

[4] in a particle ensemble-averaging sense

it can be segmented into small homogeneous paths corresponding to diagonal $[T_1]$, $[T_2]$, ... hence

$$\begin{bmatrix} V_h \\ V_v \end{bmatrix} = \frac{\lambda G}{4\pi r^2}[\mathrm{T}_1][\mathrm{T}_2]\cdots[\mathrm{T}_n][\mathrm{S}_{\mathrm{BSA}}][\mathrm{T}_n][\mathrm{T}_{n-1}]\cdots[\mathrm{T}_1]$$

Since the multiplication of diagonal matrices result in a diagonal matrix it is obvious that the previous definitions and conclusions still apply, the difference being that all the quantities now become functions of range.

What is now left is to consider the case where the precipitation particles are canted so [T] is non-diagonal. If [S] describes spherical particles, then Eq. 2.9 becomes

$$\begin{bmatrix} V_h \\ V_v \end{bmatrix} = \frac{\lambda G}{4\pi r^2} S \begin{bmatrix} T_{hh}^2 + T_{hv}^2 & T_{hv}(T_{hh} + T_{vv}) \\ T_{hv}(T_{hh} + T_{vv}) & T_{hv}^2 + T_{vv}^2 \end{bmatrix} \begin{bmatrix} M_h \\ M_v \end{bmatrix}$$

since [S] is proportional to the identity matrix. The elements of matrix [T] are given in [5],page 173 where it can be seen that $T_{hv} = T_{vh}$ so their phases will be cancelled out in $\arg[(V_h^{10})^*(V_v^{01})]$ while $\arg[(T_{hh}^2)^*(T_{vv}^2)]$ will give the familiar Φ_{dp}. Again only the crosspolar products are affected. Finally, for non-diagonal [S] the expressions become too complex, but due to $T_{hv} = T_{vh}$ eventually the definitions and interrelationships of Φ_{dp}, K_{dp} and δ_{co} are the same as before.

In brief, K_{dp} can be thought to be as the equivalent to the Z_{dr}, but for the phases of h- and v-channel signal rather than their magnitude. The reason that it is derived indirectly through Φ_{dp} is because the phase of the signal is cumulative, so the derivative has to be considered in order to come up with a radar observable defined per rain cell.

2.2 Properties and characteristics of K_{dp}

In this section some properties and unique characteristics of K_{dp} as a radar observable are discussed. First of all, K_{dp} is the range derivative of Φ_{dp}. If the rain path is homogeneous, meaning the drop size distribution is the same in every cell, K_{dp} is constant and Φ_{dp} increases linearly. If it is non-homogeneous, then K_{dp} varies and so does the slope of the Φ_{dp} range profile at each rangebin so its curve becomes now non-linear. At any case, K_{dp} is expected to be always positive since rain drops are oblate and not prolate, so Φ_{dp} is always increasing. Regions where Φ_{dp} is constant correspond to negligible values of K_{dp}, while a certain decrease can only be attributed to the effect of δ_{co} which was not completely removed from Ψ_{dp}, estimated initially.

Also, although K_{dp} and Z_{dr} both originate from the non-sphericity of the particles they differ in one important aspect. Z_{dr} is defined as the ratio of the reflectivities for the horizontal and vertical polarization, so the density of the particles does not matter; if it is increased then both reflectivities vary proportionally and their ratio is unaffected. However, K_{dp} arises from their anisotropy in a cumulative sense; increasing their density means that K_{dp} will be increased proportionally. This can be clearly seen by the expressions for K_{dp} and Z_{dr} in the Rayleigh limit:

$$Z_{\mathrm{dr}} = 10log_{10}\frac{\int |S_{hh}(r,D)|^2 N(D)dD}{\int |S_{vv}(r,D)|^2 N(D)dD} \quad (7.9a)$$

$$= 10log_{10}\frac{\int D^6 N(D)|(\epsilon_r - 1)/[1 + \frac{1}{2}(1 - \lambda_z)(\epsilon_r - 1)]|^2 dD}{\int D^6 N(D)|(\epsilon_r - 1)/[1 + \lambda_z(\epsilon_r - 1)]|^2 dD}$$

$$K_{\mathrm{dp}} = \frac{2\pi}{k_0}\mathrm{Re}\int N(D)[\hat{h}\cdot\vec{f}(r,D) - \hat{v}\cdot\vec{f}(r,D)]dD$$

$$= \frac{\pi k_0}{12}\mathrm{Re}\{\int D^3 N(D)[\frac{\epsilon_r - 1}{1 + \frac{1}{2}(1 - \lambda_z)(\epsilon_r - 1)} - \frac{\epsilon_r - 1}{1 + \lambda_z(\epsilon_r - 1)}]dD\}$$

For Z_{dr}, the drop size distribution N(D)[5] appears in a ratio while not for K_{dp}. The implication is that high values of Z_{dr} imply a medium of high anisotropy, while nothing can be said about the density of the particles. High values of K_{dp}, on the other hand, imply either a sparse medium of high anisotropy of particles ($\lambda_z > \frac{1}{3}$) or a dense medium of low anisotropy since the low anisotropy can be offset when multiplied by N(D). This underlines that K_{dp} can offer additional information to Z_{dr} regarding the microphysics of the atmospheric resolution volume.

Another important property is that K_{dp} is derived through Φ_{dp}, and Φ_{dp} being a phase quantity is not affected by attenuation effects, radar calibration errors or partial beam blockage. This is important because attenuation is significant for X-band and simple correction algorithms can be applied based on Φ_{dp} (Chapter 7). Regarding rain rate estimation, if K_{dp} is used it carries the same benefits thus avoiding underestimation which occurs in the case of attenuated Z and Z_{dr} values. On top of that, it can be shown that K_{dp} is well-immune to hail contamination ([5],p174). This is because raindrops tend to be oriented in space, while tumbling hailstones have a dispersion in their canting angles which reduces their contribution to total K_{dp} exponentially by its variance. Finally, it can be shown ([5],p388) that K_{dp} is closely linear to the **total water content** (W) with the slope being the mass-weighted mean diameter D_m. This linearity holds especially for X-band and it is independent of the form of drop size distribution, N(D). The above imply that K_{dp} is suitable to be used for rain rate estimation from a physical point of view. It is therefore reasonable that rain rate estimation algorithms that include K_{dp} can result in significant improvement in certain cases, much in the same way that the inclusion of Z_{dr} improved the pro-existing algorithms based only on reflectivity ([7], [8]).

2.3 Drop size distribution (dsd)

A rain cell is expected to contain particles of different size, shape, orientation or phase. If the exact composition of the rain cell were somehow known, it would be possible to compute the scattered field mathematically (with numerical methods), therefore the radar observables as well. On the other hand, any physical properties related to it (for example its associated rain rate or water content) could be determined by analytical computation as well. However, it is apparent that the assumption of knowing the exact cell composition is not realistic due to the multitude of the microscopic particles and their dynamic behavior.

[5] it is defined in the next section

In any case, the objective of atmospheric observations is eventually the determination of a physical quantity, such as the rain rate on which the current thesis is focused. Radar measurements only supply the radar observables, which are translated to the desired physical quantities by certain relationships. Since both are fundamentally based on the composition of the rain cell, it is useful to at least model it mathematically and describe it approximately. This is done by a **drop size distribution** (dsd) model which is a function that gives the total number of particles of a certain characteristic per unit volume. We assume that all particles are of the same orientation and phase, so the only variable characteristics remaining are:

- the size, that is the **equivolumetric diameter** (D)
- the shape, that is the **axis ratio** (r) as the particles are assumed to be spheroids. Also, r is assumed to be governed by the size (D) via a **rain drop axis ratio model** function.

Under these assumptions, the dsd gives the total number of particles per D and per unit volume so it is expressed in $[mm^{-1}m^{-3}]$. A typical dsd model is that of a modified gamma distribution (or gamma dsd) (Eq. 2.15) which has been widely used since it is able to capture the dynamics of the rain cells reasonably for a wide range of atmospheric conditions ([9]).

$$N(D) = N_0 D^{\mu} e^{-\Lambda D} = N_0 D^{\mu} e^{-(3.67+\mu)\frac{D}{D_0}} \tag{2.15}$$

The gamma dsd is a function of three parameters:

- a constant (N_o) which relates to the density of particles
- the **median drop size** (D_o) defined with respect to the water mass content ([5],p385); larger D_o implies the presence of larger rain drops
- the **shape parameter** (μ) which affects the shape of the curve, serving as an additional degree of freedom so that it can be adapted suitably to the rain event under consideration

In Fig. 2.2 some examples of possible gamma dsd's are given so that the effect of these parameters is made clear.

2.4 Rain rate estimation

The **rain rate** (R, $[mmhr^{-1}]$) expresses the amount of precipitation per unit of time, in other words 'how much' it rains and it is the physical quantity of concern for the current thesis. R can be computed provided the dsd is known and a **drop velocity model** is chosen, which expresses the velocity of a drop as a function of D. Eventually, it takes the form of a moment of the dsd like the radar observables ([5],p414). A **rain rate relationship** expresses R as a function of one or more radar observables and performs the translation from the measurement domain into the physical domain. Mathematically, the relationships are power-laws with the coefficients to be determined (Eq. 2.16-2.20). There are various rain rate relationships due to the different possible choices of the radar observables used

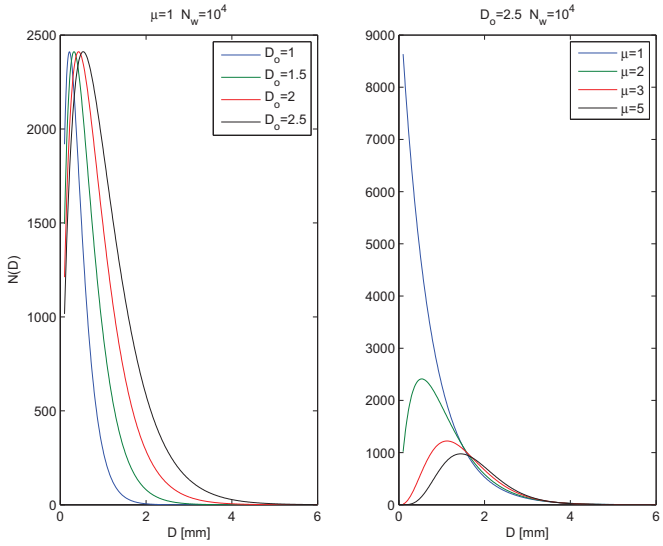

Figure 2.2: The effect of increasing D_o [mm] (left) and mu (right) on the shape of the gamma dsd. The **intercept parameter** N_w appears when the gamma drop size distribution is cast into an alternative but equivalent mathematical form. It is equal to the intercept parameter of an exponential dsd of the same water content (W) and D_o.

as inputs. However, even for the same set of observables there is a variety of coefficients. This is because the coefficients are derived via applying regression techniques on datasets, and different datasets (rain conditions) will result in different coefficients.

$$R = R(Z) = cZ^a \tag{2.16}$$

$$R = R(Z, Z_{dr}) = cZ^a 10^{-bZ_{dr}} \tag{2.17}$$

$$R = R(K_{dp}) = c{K_{dp}}^d \tag{2.18}$$

$$R = R(K_{dp}, Z_{dr}) = c{K_{dp}}^d 10^{-bZ_{dr}} \tag{2.19}$$

$$R = R(Z, K_{dp}, Z_{dr}) = cZ^a {K_{dp}}^d 10^{-bZ_{dr}} \tag{2.20}$$

Initially, R(Z) relationships were used but they were prone to bias due to hail contamination. Using a R(Z,Z_{dr}) relationship mitigates this issue and improves the accuracy of the rain rate estimation. Relationships including K_{dp} were found to give significant improvement over previous ones. Nevertheless, it has to be stressed that using the estimator that is the most accurate in theory does not guarantee the best results in practice, due to the errors involved in the estimation of the radar observables. Also, the performance of each estimator generally depends on the intensity of the rain. In [7], [8] further information can be found about the derivation and performance of rain rate estimators.

2.5 Attenuation

Attenuation is due to the imaginary part of the permittivity of the water. This means that rain drops (precipitation particles in general) absorb some of the transmitted radar beam both ways, so the received signal is attenuated in amplitude. As mentioned before, since the imaginary part of the effective wave number k_{eff} represents attenuation it follows that $E(r) = e^{-Im(k_{eff})r}E(0)$ where E(r) is the amplitude of the wave at range r. In practice the dB scale is used, so if $10log_{10}$ is applied on both sides, the attenuation factor becomes $10log_{10}e^{-Im(k_{eff})r} = -4.343Im(k_{eff})r$. Omitting the negative sign which is implicit for attenuation and taking into account that it occurs two times, the **specific attenuation A** $[dBkm^{-1}]$ is defined as:

$$A = 10^3 8.686 Im(k_{eff}) \tag{2.21}$$

For an anisotropic medium there is A_h and A_v which are unequal, so the **specific differential attenuation** A_{dp} $[dBkm^{-1}]$ is defined as:

$$A_{dp} = 10^3 8.686(Im(k^h_{eff}) - Im(k^v_{eff})) \tag{2.22}$$

If these parameters are somehow known, then they could be used to correct the attenuated Z and Z_{dr} range profiles which may be either unnecessary or essential depending on the intensity of the rain path and the frequency band. For X-band, the attenuation is expected to affect even moderate rain paths.

Chapter 3

Estimation of Differential Phase (Ψ_{dp})

As mentioned in the derivation of K_{dp} section in the previous Chapter, the differential propagation phase (Φ_{dp}) does not appear by itself but with the differential scattering phase (δ_{co}) added. Their combination is the total differential phase (Ψ_{dp}) which can be estimated by measurements. In this Chapter two ways of estimating Ψ_{dp} are presented with emphasis on the spectral polarimetry method. It is again underlined that there is no direct method for the estimation of Φ_{dp}; Ψ_{dp} has to be estimated first as presented here and then δ_{co} has to be filtered out in order to obtain Φ_{dp} and proceed with K_{dp} estimation.

3.1 Time domain approach

The time domain approach implies that a pulse radar is used, so that it emits a horizontally and vertically polarized wave alternatively according to a switching scheme and their echoes are received on both channels.

3.1.1 Formulation

A detailed analysis is given in [5], section 6.4. This time domain approach is well documented in the literature so only the key points will be mentioned that define the outline and correspond to the other approach as well.

- Ψ_{dp} entails the calculation of the phase difference between the V_{hh} and V_{vv} copolar echoes (they are complex). Of course, not a single pair is needed for reliable estimation but rather averaging over many. Statistically, this is the phase of their correlation at zero time lag. However, since the radar can only transmit a pulse of one polarization at a time, the copolar returns are never available at the same time but separated by the pulse period, T_s. Hence, their desired correlation at zero time lag cannot be expressed through measurements. Still, based on certain signal properties of atmospheric echoes, it can be shown that the correlation of the copolar signals at zero time lag can be related to that at T_s (time lag l=1). By

considering the correlation of the copolar signals first as $R_{hh,vv}$ and then as $R_{vv,hh}$[1], Ψ_{dp} can be estimated as the semi-difference of their phases.

- The accuracy of Ψ_{dp} estimation depends on the magnitude of the correlation of the copolar signals (ρ_{co}) and the Doppler spectrum width. In general, Ψ_{dp} can be estimated with an accuracy of up to 2^o provided that ρ_{co} is more than 0.97. High values of ρ_{co} imply that the received signal was due to precipitation, since non-atmospheric echoes are often decorrelated.

3.1.2 Implementation

The above were under the assumption that the radar emits pulses. IDRA is an FM-CW radar instead, so the previous formulation is not directly applicable to the content of IDRA raw data files. However, the IDRA raw files can be processed by a pulse-pair processing algorithm which is equivalent as if the data were obtained by a pulse radar so that the previous formulation is then directly applicable to them. Detailed theoretical treatment is given in [3], while practical issues are addressed in Appendix C. Eventually, using the IDRA offline processing program as explained in Appendix C, we obtain the total differential phase Ψ_{dp} in the form of a two dimensional matrix of dimension 512x143 (for a given PPI) where the columns represent different sectors and the rows represent rangebins spaced 30m apart. If a specific column is considered only, we obtain the range profile of Ψ_{dp} for that sector under the time domain approach as an one dimensional matrix of dimension 512x1.

3.2 Spectral polarimetry approach

The objective of spectral polarimetry is to treat each radar observable not as a single integrated value but as a function of the Doppler velocity of the particles. For example, the differential reflectivity Z_{dr} results from all the particles inside the rain cell with no distinction being made as to their Doppler velocities. In spectral polarimetry formulation, Z_{dr} is no longer a value but a function $Z_{dr}(\mathrm{v})$ (called *spectral* Z_{dr}), where v is the particle Doppler velocity. Therefore, the particles are grouped together regarding their velocities and their radar observables are thus distinguished. More information along with cases where spectral polarimetry offers additional physical insight can be found in [10],[11]. As far as the current thesis is concerned, focus was given on using the previously estimated Ψ_{dp} using a spectral polarimetry approach and contrasting it to the typical time domain method.

3.2.1 Formulation

A detailed analysis of IDRA signal processing is available in [3]. Here only a very brief outline will be given. IDRA is an FM-CW radar, so it emits a series of chirp pulses of duration ΔT each. The received waveform after quadratic demodulation is sampled within each chirp duration, so it can be represented as a two-variable function $s(t_k, t_n)$ where t_k denotes the samples within ΔT

[1] they are not complex conjugate because the pulse pairs are not identical, but similar only in a leap-frog scheme sense due to polarization switching

Table 3.1: Processing steps for estimation of Ψ_{dp} for the spectral polarimetry approach

1^{st} *algorithm*
obtain Ψ_{dp} as $arg(S_{hh}[k,n]S^*_{vv}[k,n])$
apply system circuitry phase offset
compensate for non-simultaneity of copolar measurements
compensate for Doppler aliasing
spectrum smoothing
zero Doppler bin suppression
spectral polarimetric filtering
clipping
2^{nd} *algorithm*
zero Doppler bin suppression
obtain Ψ_{dp} as $arg(S_{hh}[k,n]S^*_{vv}[k,n])$
apply system circuitry phase offset
compensate for non-simultaneity of copolar measurements
spectrum smoothing
spectral polarimetric filtering
clipping
compensate for Doppler aliasing

and t_n a certain chirp and its corresponding ΔT interval. By taking its Fourier Transform with respect to t_k we obtain $s(f_k, t_n)$ where the frequencies f_k can be translated into rangebins since this is the principle of FM-CW radars. With a subsequent Fourier Transform with respect to ${t_n}^2$ we obtain $s(f_k, f_n)$ where the frequencies f_n can be translated into the Doppler velocities of the particles thus forming the Doppler spectrum for a certain rangebin. In discrete notation, the result is a S[k,n] 512x512 matrix where index k denotes the rangebins and index n denotes a Doppler velocity bin. A certain column contains the values of the Doppler spectrum along the range for that Doppler velocity bin, while a certain row contains the full Doppler spectrum (all the velocity bins) for that rangebin. Taking polarization into account we end up with the S_{hh}, S_{vh}, S_{vv} and S_{hv} matrices conceptually corresponding to the V_{hh}, V_{vh}, V_{vv} and V_{hv} return signals.

3.2.2 Implementation

The starting point is the complex $S_{hh}[k,n]$ and $S_{vv}[k,n]$ matrices mentioned above. Essentially, considering the difference of the phases of their elements gives rise to Ψ_{dp}, however some extra steps have to be applied as well. These are shown in Table 3.1 as part of two current variations in the Ψ_{dp} estimation algorithm, the difference being the order of the processing steps. The steps are briefly commented:

- $arg(S_{hh}[k,n]S^*_{vv}[k,n])$ obtains a 'raw' Ψ_{dp} that has to be corrected

[2] in practice after a number of consecutive sweeps

- system circuitry phase offset is due to different circuit phase delays for the h and v channel
- the issue of non-simultaneity of the copolar measurements which prevents from estimating directly the correlation of the copolar echoes at zero time lag has been dealt by applying a phase compensation technique presented in ([12])
- In case of Doppler aliasing, the differential phase is affected and must be compensated by a fixed phase depending on which side the aliasing occurs ([12])
- spectrum smoothing for noise removal
- zero Doppler bin suppression removes the clutter corresponding to static targets
- spectral polarimetric filtering allows for advanced filtering of the spectra ideally keeping only atmospheric echoes. There are two possible filtering criteria:
  - based on $L_{dr}(v)$: the spectral L_{dr} has low values for atmospheric targets. Therefore, the Doppler bins exhibiting atypical large values (>-5dB) for this parameter are discarded ([13])
  - based on $Z_{dr}(v)$: a higher and a lower limit are defined for the Z_{dr} and according to the magnitude of the v-channel echo, parts of the spectra where the h-channel echo is higher or lower, respectively, than what is expected are rejected. This type of filtering is present only in the second variation, but not used for the present estimation of Ψ_{dp}.
- clipping rejects parts of the spectra where the magnitude of the HH copolar echo is below a defined threshold based on the noise power
- spectral differential phase filtering disregards bins having differential phase more than 30^o in absolute value. Inclusion of this step should be considered carefully, since it will result in distortion for sectors of intense rainfall such that the differential phase indeed can have values more than the threshold. For this reason, this filtering was left out from the present estimation of Ψ_{dp}.

Eventually, the result is a Ψ_{dp}[k,n] matrix with the indices k and n as explained before. In order to arrive to a single value for each rangebin and thus converge in the time domain approach, a sort of integration has to occur along the rows (Doppler velocity bins). Two approaches are available:

- Averaging over all Doppler velocity bins which are considered equally
- Weighting the Doppler velocity bin by the magnitude of the respective $S_{hh}[k, n]$ elements before averaging them, the idea being to suppress the influence of weak echoes and their associated phases which are more likely to be governed by noise and promote the influence of strong, atmospheric echoes instead

By applying this last weighting-averaging step, the final product is an estimate of the total differential phase Ψ_{dp} along the range of a certain sector, in the form of a 512x1 vector Ψ_{dp}[k] where the elements represent the rangebins spaced 30m apart. In other words we obtain the range profile of Ψ_{dp} for a sector, under the spectral polarimetric approach. Lastly, it is noticed that in the current processing routines due to a different sign convention used the Ψ_{dp} results as monotonically decreasing, that is negative. This is corrected by changing the sign at the last step of computation.

An example of an estimated Ψ_{dp} range profile according to both approaches is given in Fig. 3.1. It is seen that the curves in general tend to increase as expected for Φ_{dp}. It is noticed, however, that at this processing stage they actually are the Ψ_{dp} which includes δ_{co} which may cause any bumps on the profiles. Significant statistical fluctuations from rangebin to rangebin are also observed, which especially is true for the spectral polarimetry approach. A detailed presentation of the results from the Ψ_{dp} estimation algorithms will be given in Chapter 5. These example phase range profiles are given at this point only to draw attention and help illustrate the following points.

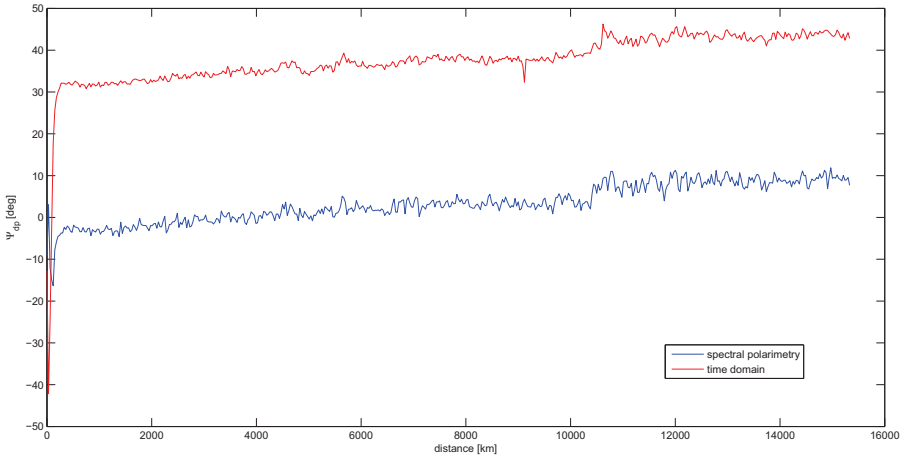

Figure 3.1: The estimated Ψ_{dp} for sector of 290^0 of the raw data file R2008-8-1_2-0-0.bin according to spectral polarimetry and time domain method. It is noticed the wrong offset of the curves for the vertical axis and the abnormally high values in the near-field region, up to about 250m. The offset can be successfully corrected while the values of the phases within the near field should be omitted from any kind of calculation.

3.3 Unwrapping of the time domain Ψ_{dp}

It was observed that the time-domain Ψ_{dp} needs unwrapping as it presents jumps of 180^o between some adjacent rangebins (Fig. 3.2). In practice the phase jumps are not exactly equal to 180^o due to the presence of noise, but in any case clearly visible. The spectral polarimetry Ψ_{dp} does not present any phase jumps. The

origin of these phase jumps is the way that Ψ_{dp} is estimated in the time-domain, as the semi-difference of two phases. One of them may be aliased so it will result in a 180^o phase jump. It was observed that these phase jumps usually occur in clusters around certain locations, or not at all. These clusters are believed to be related perhaps to regions of increased local wind turbulence but there was no actual need for the examination of this hypothesis. The most important point is that a custom unwrapping routine was eventually used instead of the integrated Matlab unwrap function due to the clustering of the phase jumps.

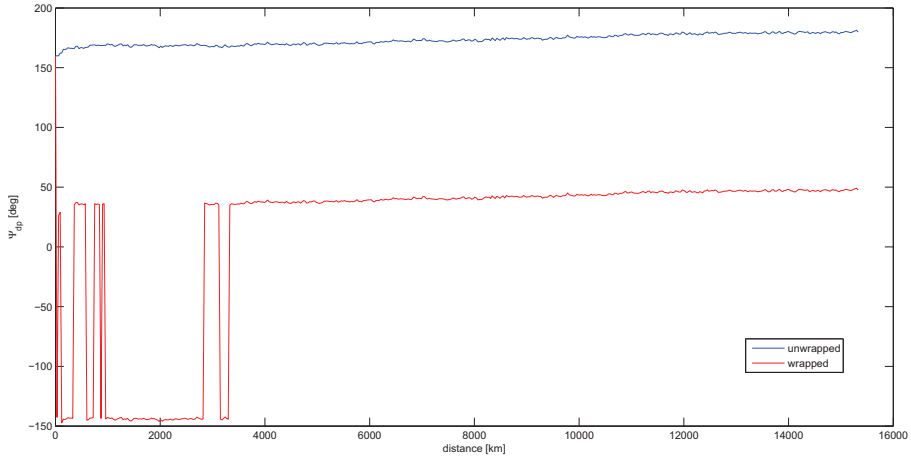

Figure 3.2: The estimated time domain Ψ_{dp} for sector of 320^0 of the raw data file R2009-5-26_4-0-1.bin. The phase jumps of about 180^0 can be seen and their tendency to occur in clusters. It is again noted the apparently wrong y-axis offset that is corrected in the next step.

3.4 Near field fluctuation of Ψ_{dp}

As it is seen in the example of Fig. 3.1, it was observed that for the first range bins, the Ψ_{dp} takes abnormally large values. The magnitude of these variations cannot be attributed to the presence of noise; it is because all the theoretical formulations used are valid for the far field range only. For IDRA, f=9.475GHz and the antenna aperture is A=1.5m in diameter so the far field is expected to begin from $r = \frac{2D^2}{\lambda} = 150m$. In practice, it was observed that these near fluctuations reach up to about 250m which is more than what expected according to the above formula. In any case, the effect of these near field fluctuations is that they contaminate the phase profiles so they should be disregarded. This is especially relevant to the next section.

3.5 Offsetting of the Ψ_{dp}

At the moment, the Ψ_{dp} range profile as estimated from the raw data files and for both the spectral polarimetry and time domain method, has not the correct

offset for the vertical axis. By this it is meant that:

- Φ_{dp} should begin from 0^o at the first rangebin.
- Due to δ_{co}, the Ψ_{dp} is not expected to begin from 0^o, but the value of δ_{co} corresponding to the first rangebin, which is expected to be a positive value of few degrees (based on simulations of δ_{co} for the X-band that are presented in Chapter 6). Of course, after correct removal of δ_{co} the resulting Φ_{dp} should begin with a value of 0^o.
- The above refer to the theoretical phase profiles. In practice, when they are estimated by measurement there is additional noise so for example the estimated Φ_{dp} may not begin strictly from 0^o but in an average sense if a small segment near the radar origin is considered.

It was observed that the estimated Ψ_{dp} has obviously not the correct offset as shown on Fig. 3.1. The reason for this is believed to be the radar circuitry despite the dedicated correction processing step during Ψ_{dp} estimation. The delay between the horizontal and vertical radar channel is expected to be constant, characteristic of the system. Perhaps this variability could be attributed to the system repairments that occurred sometimes at the past. If this assumption is correct then the relative channel delay and the resulting wrong offset between the horizontal and vertical phases should be constant between periods of continuous operation but this is not the case.

In order to fix that wrong offset issue we are based on the a priori knowledge of the expected behaviour of Ψ_{dp} and Φ_{dp} near the range origin as explained above. As it will be discussed in Chapter 6, it is possible based on the measured Z and Z_{dr} alone to compute the expected Ψ_{dp} range profile. That means that another way to offset correctly the measured Ψ_{dp} is to offset it so that it matches, in an average way, the computed Ψ_{dp}. However, this approach is not practical because it entails a series of computations simply for offsetting the estimated Ψ_{dp} that has to be repeated for each case. Still, it can be used as a check for the validity of the used, practical method. It has to be mentioned that comparing the two aforementioned phase profiles over the whole range is not suggested because the attenuation progressively affects the expected Ψ_{dp} (Chapter 6). For this reason only the beginning of the curves, up to about 5km where the attenuation can rather be safely ignored, should be compared. It was found out that there is agreement between the two different offset correction methods as it will be recalled in Chapter 6. In Fig. 3.3 this approach is illustrated. To sum up, the practical way to correct the wrong Ψ_{dp} offset is:

- estimate δ_{co} as explained in Chapter 6
- subtract δ_{co} from Ψ_{dp} to obtain Φ_{dp}
- calculate the deviation of Φ_{dp} from 0 degrees by taking its average in the 250-700m range. This range was selected so that on one hand it avoids the contamination due to the near field effects, on the other hand it contains enough rangebins to cancel out the statistical fluctuations. The upper range limit cannot be arbitrarily far because then the theoretical average will not be zero, as the cumulative increase of Φ_{dp} will not be negligible. In practice, low values of K_{dp} were typically observed in the beginning of

the range. If 0.3deg/km is taken as a limit then the maximum error in the offset correction is 0.21 degrees (this is how much the Φ_{dp} is expected to build up at 700m). It is noted that this is the worst case, when this maximum value for K_{dp} extends all over the averaging range.

- subtract the thus described average value from Ψ_{dp} since it represents the wrong offset

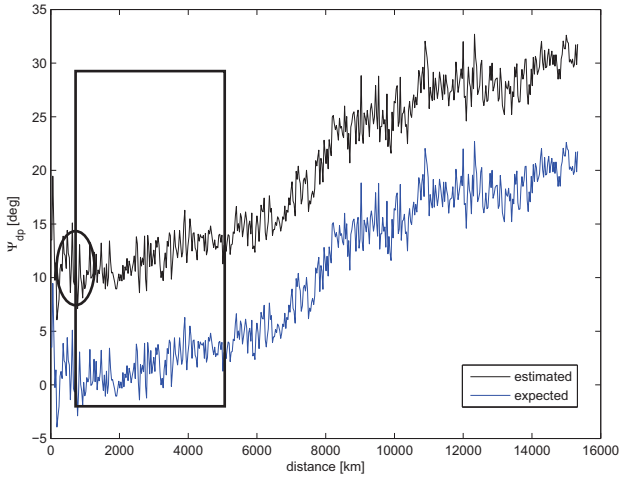

Figure 3.3: Illustration of the two possible approaches for offset correction. The expected curve, derived computationally is correctly offset in contrast to the estimated one (a wrong offset of $+10^o$ is shown here). The estimated curve can get a correct offset based only on the segment annotated by the circle. Another way is to calculate the relative average difference of the two curves on the segment annotated by the rectangle. Only the first approach is practical, as explained, however comparing the two results is a check for its validity.

Chapter 4

Estimation of Specific Differential Phase (K_{dp})

4.1 Estimation of K_{dp}

As mentioned on section 2.1, from a mathematical point of view K_{dp} is simply the first derivative of the propagation differential phase Φ_{dp} with respect to the range, that is the distance from the radar. According to Chapter 3, we can have an estimation of the total differential phase either in time domain or through a spectral polarimetric approach. This means that we can subsequently estimate a K_{dp} based on the time domain or the spectral polarimetric approach, respectively. In the following, no distinction is made regarding the way that Φ_{dp} was estimated since there is no difference in the subsequent estimation of K_{dp} itself. The steps for K_{dp} estimations are the following:

1. Removing δ_{co} from the Ψ_{dp} range profile so that only the propagation differential phase Φ_{dp} remains.

2. Smoothing the resulting Φ_{dp} curve which is expected to have statistical fluctuations.

3. Applying an estimator for its range derivative, which is K_{dp} by definition.

The first step is needed because δ_{co} is coupled to Φ_{dp} and only their sum, Ψ_{dp}, can be estimated by measurements while K_{dp} is related only to Φ_{dp}. For the lower frequency bands (such as S or C) where the scattering mechanism is normally under the Rayleigh limit δ_{co} can be ignored as it is expected to be zero. However, IDRA is an X-band radar so δ_{co} is not negligible in principle. Removal of δ_{co} is only possible if there is a kind of estimator for it and this is treated in Chapter 6.

As to the estimator itself, the simplest first derivative estimator has the following form:

$$\hat{K}_{\mathrm{dp}} = \frac{\Phi_{\mathrm{dp}}(r_2) - \Phi_{\mathrm{dp}}(r_1)}{2(r_2 - r_1)} \simeq \frac{\hat{\Psi}_{\mathrm{dp}}(r_2) - \hat{\Psi}_{\mathrm{dp}}(r_1)}{2(r_2 - r_1)} \tag{4.1}$$

and the variance of the estimator, denoting the accuracy of the estimation, is given by

$$\mathrm{SD}[\hat{K}_{\mathrm{dp}}] = \frac{\mathrm{SD}[\hat{\Psi}_{\mathrm{dp}}]}{\sqrt{2}\Delta r} \tag{4.2}$$

It is clear that if higher accuracy is desired, either larger range segments should be considered or somehow the accuracy of Ψ_{dp} estimation should be improved. This is a general point regarding K_{dp} estimation: **accuracy and resolution are conflicting**, therefore a trade-off will always be present. For rain rate estimation, the accuracy of K_{dp} estimation should be within some tenths of a deg/km. Taking 0.2deg/km as the maximum allowed and assuming that $\mathrm{SD}[\Phi_{dp}]=2^o$, it can be seen that Δr which is the range segment over which K_{dp} is estimated, should be a little more than 7km which is not practical. It is seen that such an intuitive estimator that is based only on two end-points is not applicable. Also, in order to avoid negative values for K_{dp} the Φ_{dp} range profile should be strictly monotonous, probably requiring heavier smoothing in some parts than in others. If it is filtered at once, some parts will undergo excessive smoothing resulting in underestimation of K_{dp}. Otherwise, it should be filtered in an adaptive way which gives rise to complication.

In order to avoid these issues, another estimator may be used that takes into account more than two adjacent rangebins relaxing the requirements on the shape of Φ_{dp} profile. The estimator used is given next and its physical meaning is that we consider a certain segment of N rangebins, apply a straight line fit to the Φ_{dp} segmented profile and obtain its slope[1] (Fig. 4.4).

$$\hat{K}_{dp} = \frac{\sum_{i=1}^{n}[\Psi_{dp}(r_i) - \bar{\Psi}_{dp}](r_i - \bar{r})}{2\sum_{i=1}^{n}(r_i - \bar{r})^2} \tag{4.3}$$

$$\bar{\Psi}_{dp} = \frac{1}{N}\sum_{i=1}^{n}\Psi_{dp}(r_i) \tag{4.4}$$

$$\bar{r} = \frac{1}{N}\sum_{i=1}^{n} r_i \tag{4.5}$$

This is the estimated K_{dp} which is assigned to its rangebin (i). By shifting this window of N points K_{dp} is calculated for the rest of the rangebins as well. The advantage of using this estimator over a more complicated one (for example considering a higher degree fit to the Φ_{dp}) is that its standard deviation can be expressed analytically, which makes it appropriate to be used as a first attempt. In Fig. 4.1, its standard deviation is shown. Since for IDRA the rangebins are spaced apart by 30m, it can be seen that for the desired accuracy of estimated K_{dp} the segments considered should be no less than 1.5km (50 rangebins).

Smoothing of the Φ_{dp} profile previous to applying the K_{dp} estimator can be done by using a low pass filter in order to remove the rapid statistical fluctuations and keep only the cumulative, slow-varying, mean trend of the phase profile which is Φ_{dp}. This step is needed since differentiation, which is basically the process of applying an estimator for K_{dp}, will further increase this noisy part of the signal. This issue is discussed in the following section.

[1] since the derivative of a straight line is its slope

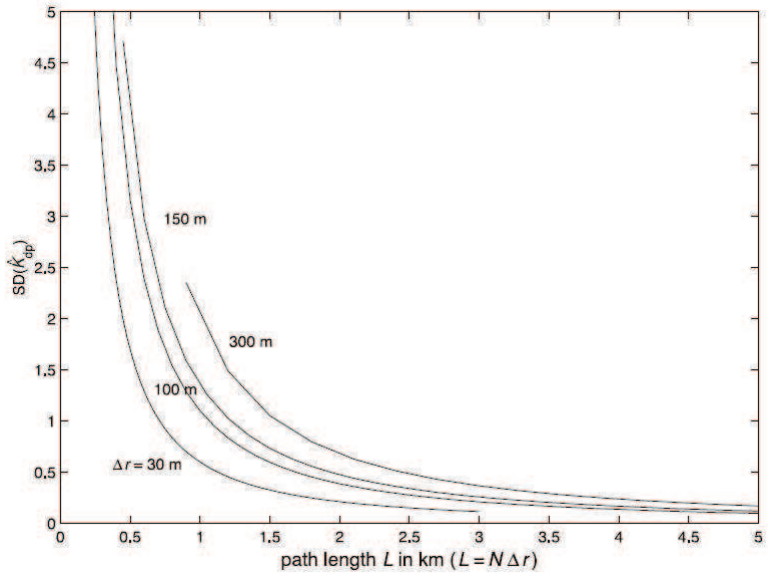

Figure 4.1: The trade-off between accuracy (low standard deviation) and resolution is prominent for K_{dp} estimation ([5], p375).

4.2 Filtering of the Φ_{dp}

Filtering of Φ_{dp} is crucial because of the statistical fluctuations. If the filtering is not enough then it will introduce bias to K_{dp} estimation and will make difficult the understanding of the physical meaning of the Φ_{dp} curves. On the other hand, if it is excessive it will result in underestimation for K_{dp}. The possibility for some kind of adaptive filtering based on local phase fluctuations is attractive but complicated. Three types of filters were considered and some example filtering results are shown in Fig. 4.2.

- A simple moving average filter. It was found out that it produces sufficiently smooth curves with length of integration N at the very least 48 rangebins, preferably 64, which is close to the expected inherent smoothing aspect of the K_{dp} estimator (1.5-2km). However, the resulting curve appears to be shifted in range as if "delayed" so the shape is disturbed which must be avoided if we wish to compare Φ_{dp} curves (Chapter 6).

- This "delay" effect is due to filter phase distortion. The filter phase distortion will be opposite if the data series is processed from its end to the beginning (backwards). Hence, for cases where the whole data series is available (non real-time) the filter phase distortion can be cancelled out[2]. In this way, the phase distortion of the filter cancels out and the shape of the filtered curve remains exact. However, one characteristic of such a filtering operation is that the values at the end match perfectly the input. This is not desired for the end rangebin as the phase fluctuations can result in distortion (Fig. 4.2). To treat that, the value at the end point has to

[2]filtfilt command in Matlab

be set at the local average in order to exclude the influence of phase noise. For the range origin, this filter behaviour is actually desired because it will always set it to 0 degrees if a similar approach is applied. In that case, comparison with expected Φ_{dp} curves is facilitated. If this filter is used, N=48 is enough since it is applied two times. This is the smoothing filter that was selected as more appropriate and used in all the following results regarding Φ_{dp}. It is also noticed that before applying the smoothing filter, the Φ_{dp} should not contain any NaN values resulting from the previous spectral polarimetric filtering and noise removal processing. Typically, this happens for cases of low reflectivity where Φ_{dp} is of no concern. Still, it may happen for a few rangebins even for cases where Φ_{dp} is relevant. In such a situation, the missing NaN values are replaced from neighbouring rangebins.

- Use of a Lowess filter. This is expressed by two continuous parameters, λ and α so there is an additional degree of freedom. It keeps the shape of the input curve and regarding its behaviour at the end points, it is not set strictly to the values of the input but it reflects the local trends. As discussed above, for the end rangebin this is desired, but concerning the range origin, care should be taken so that there is no artefact. It was found that by using values of λ=2 and α=0.3 similar results with the two-way filter are obtained.

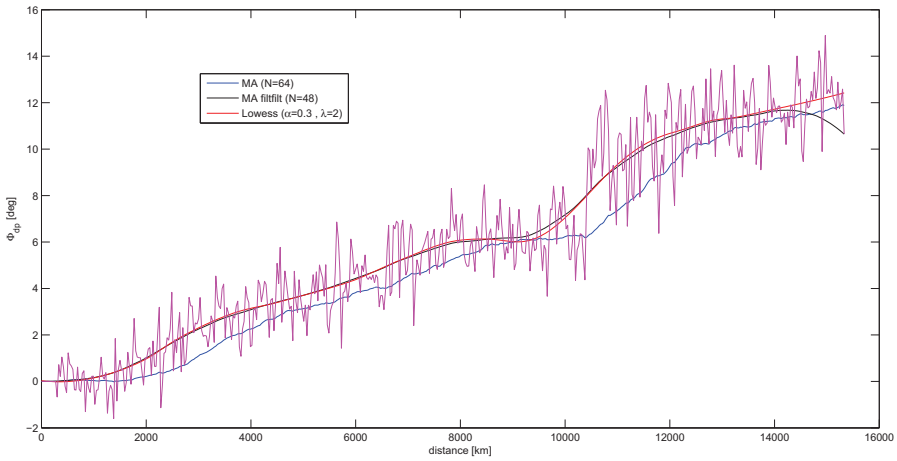

Figure 4.2: The corresponding Φ_{dp} to Fig. 3.1 (spectral polarimetry approach) after δ_{co} removal and offsetting of the Ψ_{dp}. The three available smoothing filters are compared. It is seen the "delay" caused by the MA filter that distorts the actual Φ_{dp} curve shape. With the filtfilt MA and the Lowess filters similar result is obtained without any distortion. It is noticed the strict end-point setting for the filtfilt filter which results in an artificial downward trend at the end of the range. This can be overcome by using the local average of Φ_{dp} as the final rangebin value (Fig. 4.3).

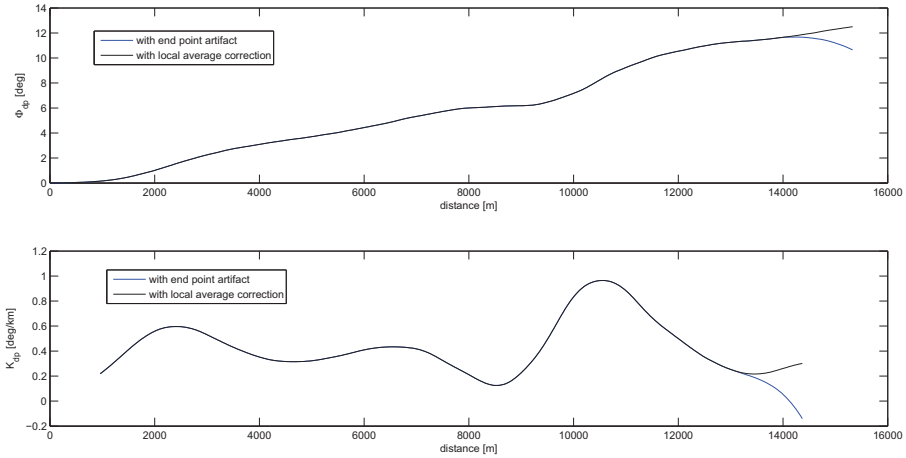

Figure 4.3: The local average correction for the filtfilt MA smoothing filter is shown. Without it, the resulting K_{dp} would also be biased.

4.3 Errors in K_{dp} estimation

In this section the main possible sources of error in K_{dp} estimation are discussed, along with ways to mitigate them.

4.3.1 K_{dp} bias due to δ_{co}

K_{dp} is defined as the range derivative of the Φ_{dp}, the *propagation* differential phase, however in practice Φ_{dp} does not appear by itself; it appears as part of the *total* differential phase, Ψ_{dp}, which is the differential phase that is actually estimated in Ch. 3. The other part is the differential scattering phase δ_{co}, Eq. 4.6.

$$\Psi_{\mathrm{dp}} = \Phi_{\mathrm{dp}} + \delta_{\mathrm{co}} \tag{4.6}$$

The presence of δ_{co} will give rise to a bias, $\bar{K}_{dp}^{\delta_{co}}$, in the estimated K_{dp} according to Eq. 4.7. In practice, the differentiation is interpreted in the same way as the estimation of K_{dp} from Φ_{dp} mentioned above, so $\bar{K}_{dp}^{\delta_{co}}$ it is the slope of the straight-line fit to a segment of δ_{co} profile (Fig. 4.4).

$$\bar{K}_{dp}^{\delta_{co}} = \frac{1}{2}\frac{d\delta_{\mathrm{co}}}{dr} \tag{4.7}$$

$\bar{K}_{dp}^{\delta_{co}}$ is zero if:

1. δ_{co} is zero itself. This is a valid assumption for S-bands radars, however for C-band and especially X-band the assumption does not always hold.

2. δ_{co} is non-zero yet steady with respect to the range, so its range derivative is still zero and there is no bias.

In principle, since IDRA is an X-band radar we choose not to disregard δ_{co} as being zero, as even for moderate rain paths where the size of the rain drops is not expected to be relatively large the scattering will still be non-Rayleigh; this will become even more pronounced for more intense rain paths. On the other hand, in some cases it may be steady along the range but this is a very restrictive case since it accounts only for homogeneous rain paths. For these reasons, we account for the presence of δ_{co} and aim to correct its bias. This bias can be minimized (ideally eliminated if δ_{co} is completely removed) in two ways:

- by filtering. Since δ_{co} may vary from rangebin to rangebin in contrast to Φ_{dp} which is range cumulative, the presence of δ_{co} may be obvious as it will appear as 'bumps' on top of the Φ_{dp} slow-varying profile. These bumps can be easily removed if they are obvious, however in order that they are obvious they should not extend over a long distance thus get concealed within the mean trend of Φ_{dp}. This approach seems more suitable for long range radars such as those operating in S or C band where δ_{co} bumps can easily be spotted within a long Φ_{dp} profile. X-band IDRA has a maximum range of 15km and for this approach to work the δ_{co} bursts should only occur within limited range segments so that they are apparent. This assumption seemed of limited validity and in order to avoid the ambiguity issue of where *exactly*[3] Φ_{dp} ends and δ_{co} starts, we opted for the next approach.

- by using an estimator for δ_{co}. If δ_{co} is somehow obtained, it could be subtracted from the estimated Ψ_{dp} directly. However, δ_{co} cannot be estimated directly from measurements hence a indirect way has to be found. This could be done if δ_{co} is estimated through another observable. For example, Z_{dr} seems suitable since they both originate from the non-sphericity of the precipitation particles so that the estimation has a physical basis as well. This approach is presented in section 6.5.

4.3.2 K_{dp} bias due to non homogeneous path

Eq. 4.3 implies that for the estimation of K_{dp} we consider range segments over which we compute a best linear fit of the Φ_{dp} range profile (Fig. 4.4). This implicitly assumes that the rain path is homogeneous so Φ_{dp} is indeed a linear curve. If the rain path is not homogeneous, then what we try to estimate is of limited physical basis. Essentially, inhomogeneities along the considered range segment will result in either overestimation or underestimation of K_{dp}. This is not unlike $\bar{K}_{dp}^{\delta_{co}}$ shown in Fig. 4.4, the difference is that the bias is due to the linear assumption for the estimator itself and not because of a external variable (δ_{co}). In [14], [15], a detailed analysis was carried out for S-band regarding all sources of bias and their potential effect in subsequent rain rate estimation. It is believed that similar work should be done for the X-band as well if K_{dp} is to be used for rain rate estimation and correlation with rain gauges measurements. This bias was not taken into account since rather extended analysis is required, however an assessment of the estimated K_{dp} will be carried out later comparing it with its expected values and the agreement can be checked for homogeneous and non-homogeneous rain paths.

[3] this ambiguity will have greater effect when the precipitation is not heavy and K_{dp} takes small values as in the rain events examined

4.3.3 K_{dp} bias due to attenuation

In X-band, the attenuation is no longer negligible even for light rain. K_{dp} estimation is based on Φ_{dp} which being a phase quantity is unaffected by amplitude attenuation effects, provided the signal is above the noise level. Hence, attenuation seems irrelevant to K_{dp} estimation. However, if a $\delta_{co}(Z_{dr})$ correction is applied to the Ψ_{dp} range profile, attenuation effects will have indirect effect on K_{dp} estimation through inexact and possibly insufficient δ_{co} removal. This issue will be recalled in Chapter 7.

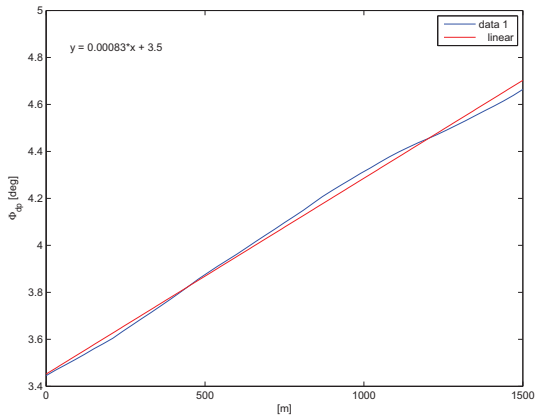

(a) Φ_{dp} segment

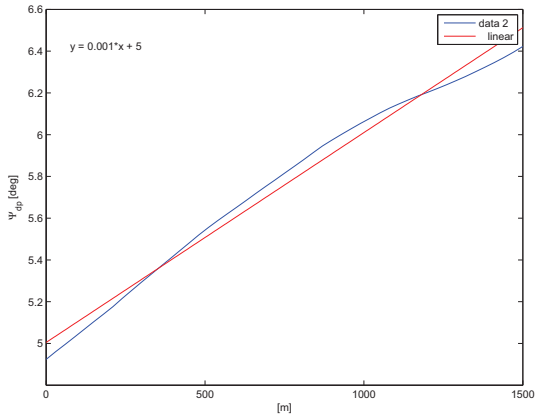

(b) Ψ_{dp} segment, smoothed but without δ_{co} removal

Figure 4.4: A Φ_{dp} (a) and Ψ_{dp} (b) segment from the phase profile of Fig.4.2 is shown. Actually it corresponds to the 6-7.5km part, however the range is shown here to start from zero for simplicity. The K_{dp} estimator applies a linear fit to the segments and calculates the slope. That means that the resulting K_{dp} value for (a) is 0.83deg/km, as there is a phase excursion of about 1.2deg over 1.5km (1.2/1.5=0.8deg/km). In (b), the resulting K_{dp} value is 1deg/km, because the presence of δ_{co} introduces fluctuation on the Φ_{dp} profile and the K_{dp} estimator is biased. Therefore, in this case $\bar{K}_{dp}^{\delta_{co}}$ is positive and equal to 0.17deg/km, or 20%. However, it could also be negative depending on the δ_{co} fluctuation. It is noticed that the bias due to non-homogeneous path can be thought as similar, since when the rain path is not uniform the Φ_{dp} segment (a) will not be linear as in this case, so its fluctuation (as in (b)) will result in a respective bias.

Chapter 5

Results

In this chapter the results obtained by processing two IDRA raw data files according to Chapters 3 and 4 are presented and discussed. These particular raw data files were selected because they correspond to relatively intense rain events making the estimation of Φ_{dp} and K_{dp} more reliable. In general, the occurrence of a meteorological event can easily be concluded by visual inspection of the reflectivity PPI and the records of other observation instruments placed at the Cabauw atmospheric site.

5.1 Case study A

This first rain event occurred on 1^{st} of August 2008 between 00:00-03:00 UTC. High values of reflectivity (up to 40dBZ) were recorded, which stand out among the typically observed ones for IDRA. Also, the precipitation was not homogeneous so within each different sector there is a unique range profile of the reflectivity and differential reflectivity. This offers the opportunity to apply the estimation algorithms on a variety of different conditions with respect to the intensity and homogeneity of the precipitation. There are three raw data files available for this rain event, namely R2008-8-1_0-0-0.bin, R2008-8-1_1-0-0.bin and R2008-8-1_2-0-0.bin. Each one represents a one-minute continuous raw data recording every one hour (as indicated in the filenames), in other words a full azimuthal scan since the rotational speed of IDRA was 1rpm. Of these three available files, the last one was chosen as it contains a larger number of intense rain cells.

In Fig. 5.1-5.4 the reflectivity, differential reflectivity, mean Doppler velocity and Doppler width are shown as PPI scans. It is noticed that the Z_{dr} parameter can be biased for some sectors (Appendix B). The sector that corresponds to a viewing angle of 0^o is oriented along the North, and the azimuth angle increases clockwise. For example, the sector of 270^o matches the West direction. The following results correspond to the sector of 274^o, as marked in Fig. 5.1. In Fig. 5.5 the estimation of the total differential phase[1] Ψ_{dp} is shown for the range-bin located 10km away from the radar, under the spectral polarimetry approach (section 3.2). As explained before, if the differential phase is estimated with a time domain approach then at a certain location (rangebin)it is represented by

[1]since it contains δ_{co} at this processing step

a single value. However, the spectral total differential phase extends over the Doppler velocity bins so it is a function defined over them. The blue curve is the total differential phase while the green curve is the weighting function, the spectral reflectivity (section 3.2.2). The left column, which is in dB scale, and the right column being in linear scale, are otherwise identical. The gaps of the curves for the upper row are due to the spectral polarimetric filtering and noise clipping. They correspond to Doppler velocity bins where there is not meteorological echo. It is also mentioned that the gap around the Doppler velocity 0m/sec is due to a fixed notch filter. In the lower row all parts of the spectra are attached together so that the weighting process becomes clearer; the blue curve ($s\Psi_{dp}$) is weighted by the green one (sS_{hh}).

By applying the spectral weighting, the result is the value of Ψ_{dp} assigned to that particular rangebin. The other option is to apply a uniform weighting, essentially taking the average of spectral Ψ_{dp} values over all the velocity bins equally. Doing this for all rangebins along the radar beam, the result is the range profile of Ψ_{dp} as shown in Fig. 5.6. In the upper row the red curve corresponds to the first algorithm of Ψ_{dp} estimation while the blue to the second; for the left subfigure uniform averaging was performed in contrast to spectral weighting for the right one. In the lower row the same curves are grouped differently, in terms of the weighting method. Apparently, there are four possible candidate Ψ_{dp} range profiles depending on the choice of algorithm and the method of weighting. Based on many similar results as the one depicted here, it was concluded that:

- Spectral weighting results in less statistical variation than uniform averaging.
- The two different algorithms have no noticeable differences, which is indication of the robustness of the Ψ_{dp} estimation.

Therefore, for the subsequent estimation of K_{dp} we chose to use the Ψ_{dp} range profile obtained from the first variation[2] and by applying spectral weighting. In Fig. 5.7, all the available radar observables are shown under the time domain and spectral polarimetry approaches. Based on many similar results as the one depicted here, it was concluded that:

- There is very good agreement on Z and Z_{dr} except for some narrow spikes present in the time domain approach. It is believed that these are due to spurious signals which are removed with spectral polarimetric filtering and this is the reason that they do not appear in the spectral polarimetry approach.
- The agreement on L_{dr} is not good, however L_{dr} is very difficult to measure reliably due to the very weak level of the cross-polar echoes and since L_{dr} is not much involved in the estimation procedures this issue was disregarded.
- There is agreement on the estimated Ψ_{dp} between the two different approaches. Under spectral polarimetry the resulting curve has more statistical fluctuations which is a disadvantage, but after applying a smoothing filter the filtered curves are expected to coincide.

[2] it could have been the second as well

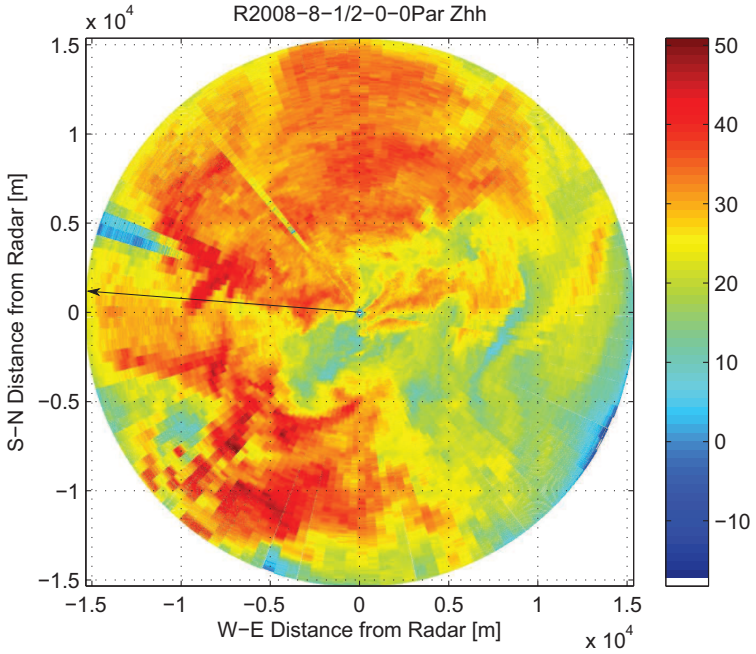

Figure 5.1: PPI of the reflectivity in dBZ.

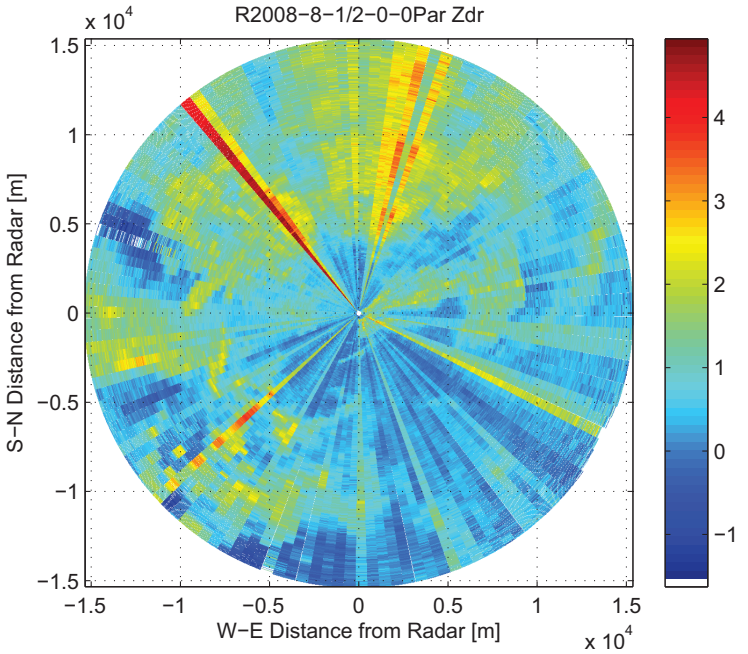

Figure 5.2: PPI of the differential reflectivity in dB.

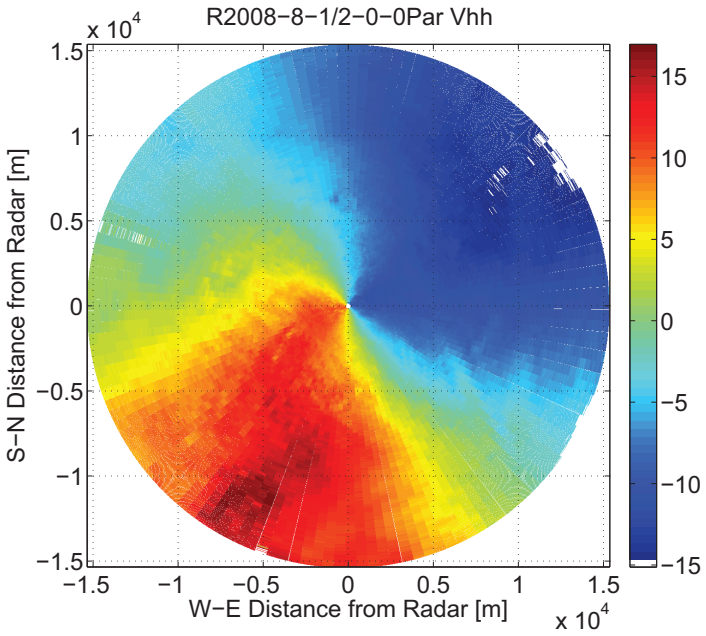

Figure 5.3: PPI of the mean Doppler velocity in m/sec.

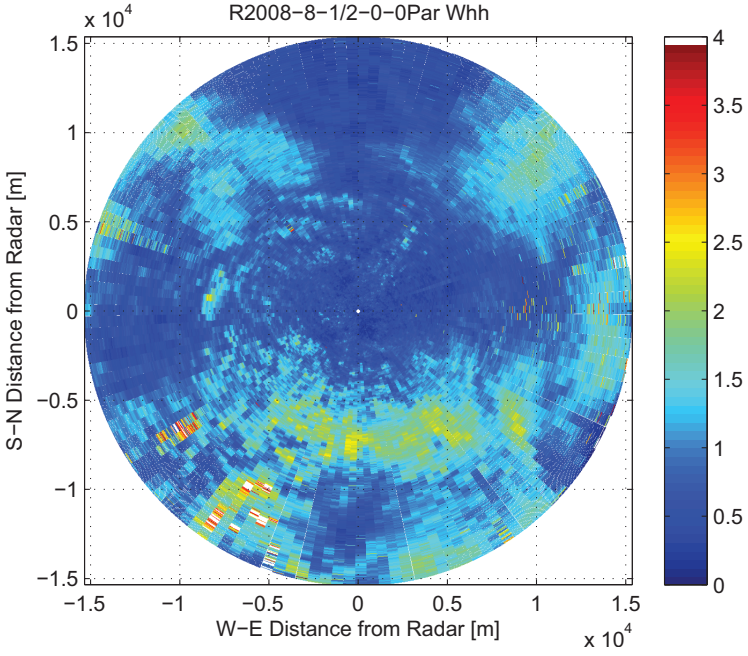

Figure 5.4: PPI of the Doppler width in m/sec.

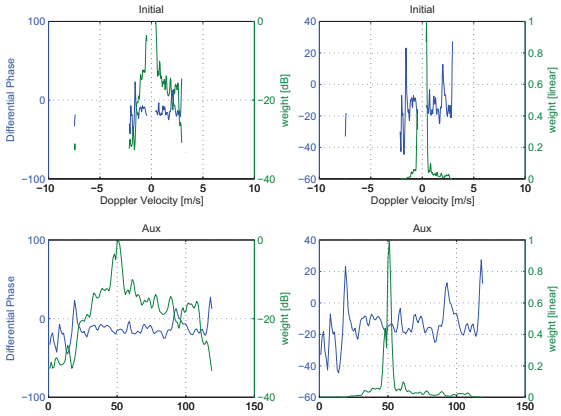

Figure 5.5: The spectral total differential phase (sΨ_{dp}) for one rangebin (blue curve). The spectral reflectivity (sS_{hh}), which will be used as a weighting function, is also shown (green curve). On the lower right subfigure it is seen that only a narrow part around the peak of the weighting function will contribute to the resulting Ψ_{dp} value of about -15^o. The minus sign is because at this processing stage the differential phases are computed with negative sign. So it is actually about +15^o as it can be seen in Fig. 5.6.

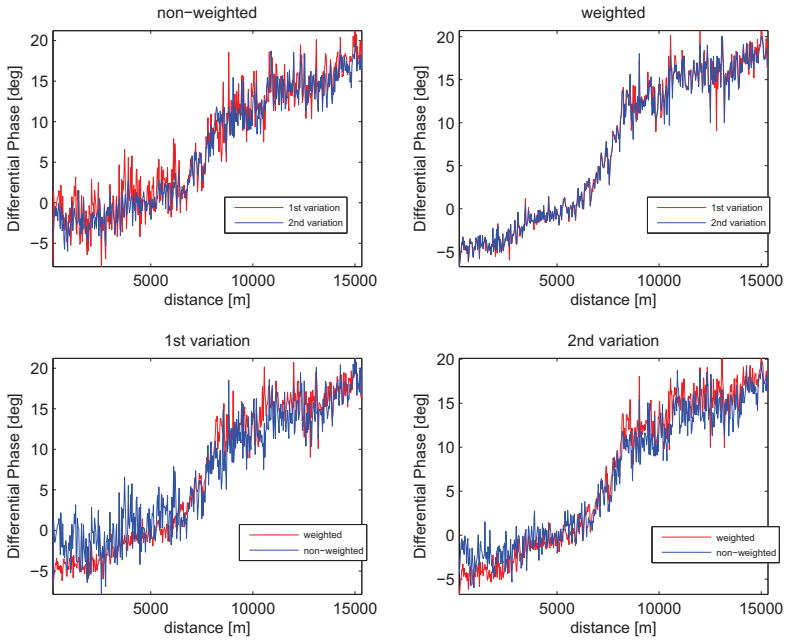

Figure 5.6: The Ψ_{dp} range profile for the sector of 274^0. There are four candidate Ψ_{dp} curves as there are two algorithms for its estimation and the possibility for either spectral weighting or uniform averaging. It is noticed that at this processing stage there is no offset correction, which will apparently be about +5^o.

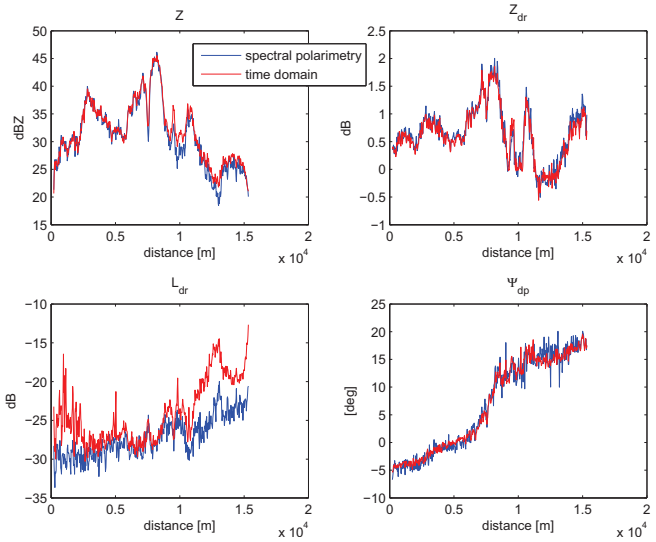

Figure 5.7: Comparison of the radar observables under the time domain and spectral polarimetric approach. Good agreement is observed except for L_{dr} which is of no consequence for our estimations.

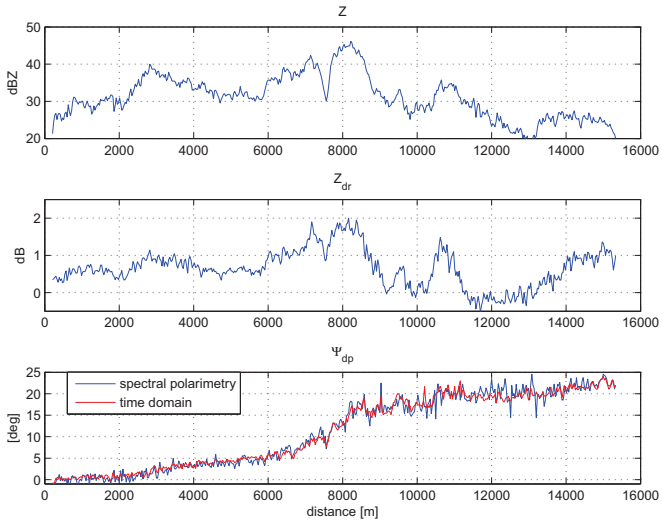

Figure 5.8: The range profiles for Z, Z_{dr} and Ψ_{dp} (with correct offset since δ_{co} is available at this processing stage).

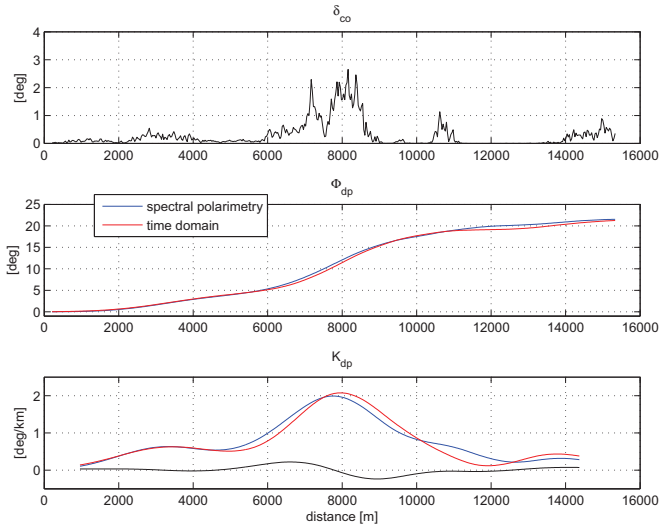

bias.Figure 5.9: The range profiles for δ_{co}, Φ_{dp} and K_{dp}. The black curve in the lower subfigure is the estimated $\bar{K}_{dp}^{\delta_{co}}$ bias.

Having the Ψ_{dp} range profile the δ_{co} is removed by using a $\delta_{co}(Z_{dr})$ relationship resulting in the desired Φ_{dp} range profile. Afterwards, Φ_{dp} is smoothed by applying a two-way smoothing filter of 48 rangebins (about 1.5km in extent) and the K_{dp} is estimated (Fig. 5.8-5.9). These two processing steps were discussed in Chapters 3 and 4.

From Fig. 5.8-5.9 it is seen that the K_{dp} curve "follows" the shape of the Z and Z_{dr} curves which is expected. Of course, the resolution of the K_{dp} curves is lower because the K_{dp} estimator operates on large range segments (N=48 in this case). The reflectivity peak at 8km is the among the strongest observed with IDRA and accordingly the value of K_{dp} at that point is one of the highest. This particular sector is non-homogeneous and this also is apparent in the Φ_{dp} profiles that exhibit a varying local slope (which is expressed locally by K_{dp}). Regarding δ_{co}, it is seen that it can have high values but its actual contamination depends on its slope: it has to be constantly increasing or decreasing in order to introduce a strong positive or negative bias, respectively. In this case this takes place only around 8km in a limited way so the $\bar{K}_{dp}^{\delta_{co}}$ is in magnitude less than 0.2deg/km. It is noticed that this bias is not present in the given K_{dp} curves; it would be if no δ_{co} estimation had taken place, and it is computed in order to assess its effect in general.

5.2 Case study B

The second rain event occurred on 25^{st} of May 2009 from about 19:30 till 04:30 UTC the next day. However, the intensity of the precipitation was particularly high only between 20:00-21:00 and 1:30-4:30. High values of reflectivity were observed (up to 40dBZ) allowing for more reliable estimation of K_{dp} than in the case of weak atmospheric echoes, accompanied by variation in the intensity and homogeneity of the precipitation within the sectors. The content of the corresponding raw data files is similar as explained before and they are available every half an hour or even every ten minutes for some part of the event. In Fig. 5.10-5.13 the reflectivity, differential reflectivity, mean Doppler velocity and Doppler width are again shown as PPI scans. Following are the respective figures similar to the previous case study (the sector of 320^o of the raw data file R2009-5-26_4-0-1.bin was selected in this case).

In this case, this particular sector is rather homogeneous as it is seen by the Z and Z_{dr} profiles and this is why the Φ_{dp} profile has limited slope variability. It has to be stressed, however, that due to the aspect ratio of the figures they appear somehow elongated and this conceals the small slope variations in the Φ_{dp} profile; they become obvious in the K_{dp} curve which presents a certain variability, but mostly around a mean value rather that strong peaks since this sector is essentially homogeneous unlike the previous case study. Even though the K_{dp} has small values in this case and limited variation, there is still a slight peak discernible at 11km, correlated to the Z and Z_{dr}, which is a positive point for the sensitivity and correctness of its estimation.

It is important that sectors from different raw data files be analyzed, because each one represents a different rain event of different properties (different drop size distribution). In this way the processing algorithms are tested against a variety of meteorological conditions so their performance is assessed in a realistic way. Therefore, in Appendix A more results are given based on the processing discussed so far and the assessment approach presented in Chapter 6.

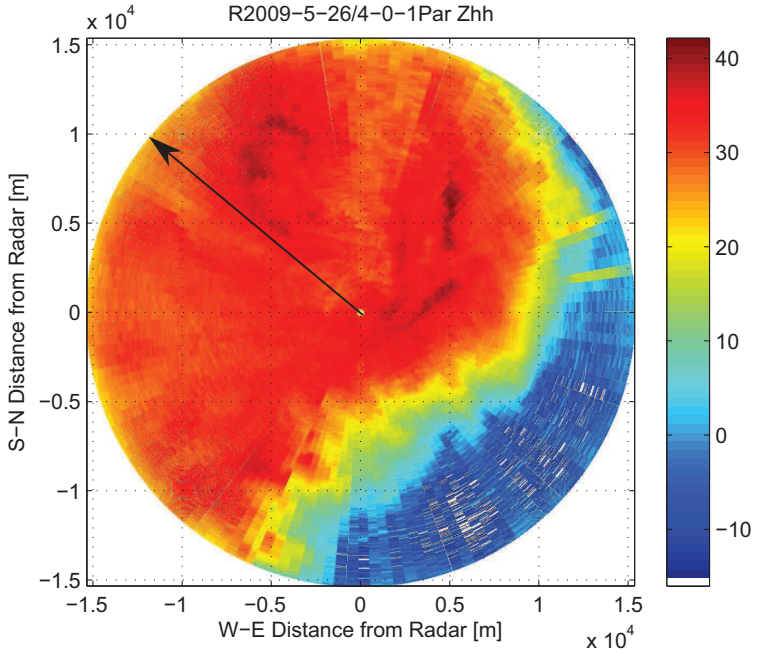

Figure 5.10: PPI of the reflectivity in dBZ.

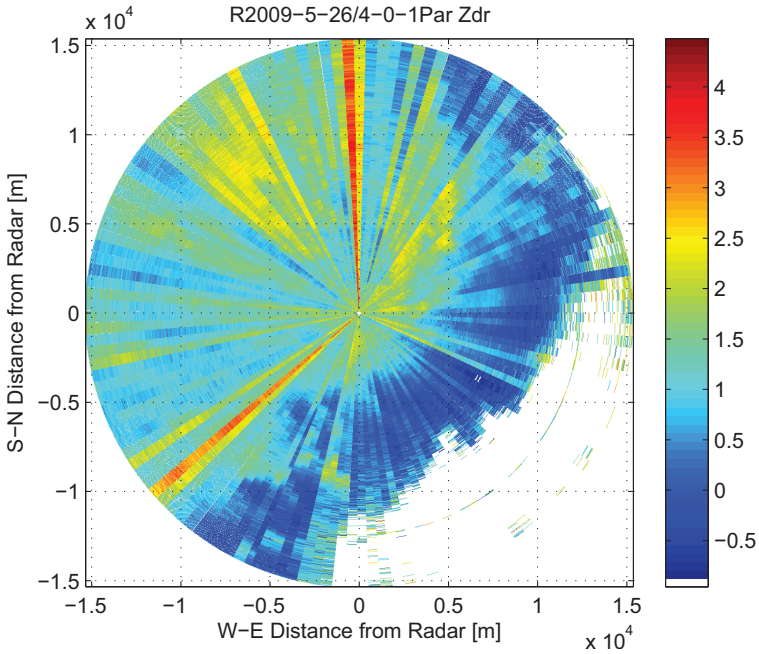

Figure 5.11: PPI of the differential reflectivity in dB.

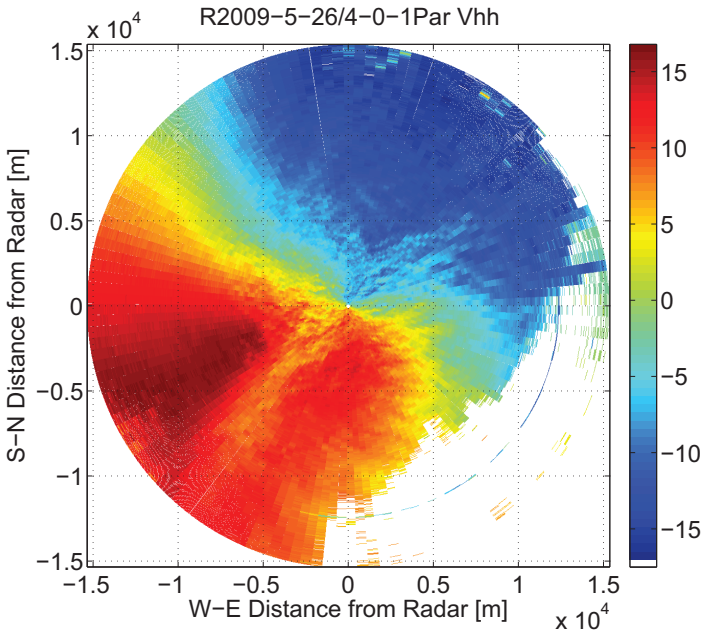

Figure 5.12: PPI of the mean Doppler velocity in m/sec.

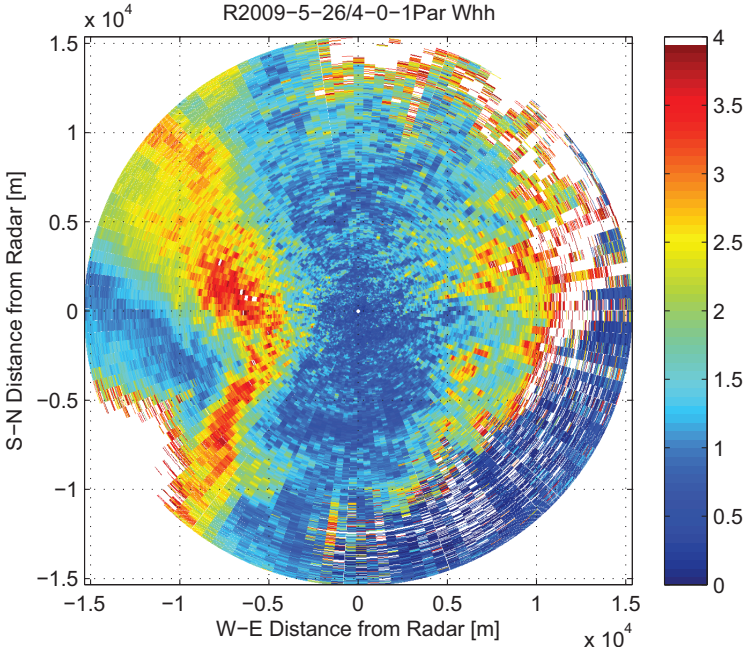

Figure 5.13: PPI of the Doppler width in m/sec.

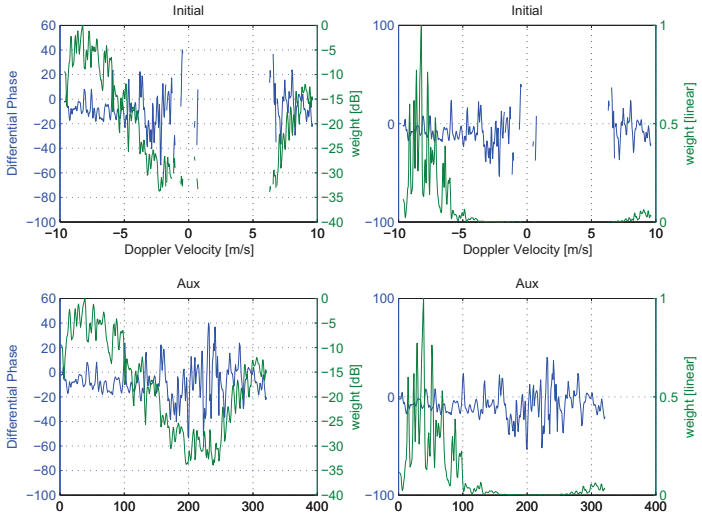

Figure 5.14: The spectral total differential phase sΨ_{dp} (blue curve) and the spectral reflectivity sS_{hh} (green curve) for the rangebin located at 10km. In contrast to Fig. 5.5, in this case a larger number of velocity bins have actual contribution to the resulting Ψ_{dp} value for the rangebin, as the weighting function does not present such a strong peak.

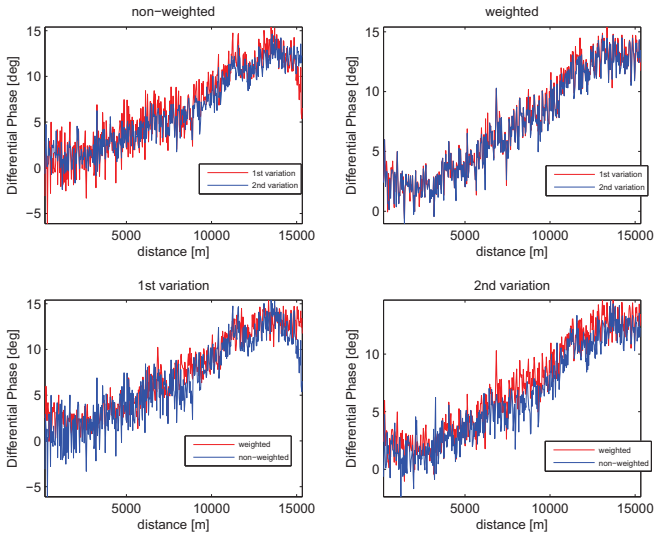

Figure 5.15: The Ψ_{dp} range profile for the sector of 320^0. As before, there are four candidate Ψ_{dp} curves. Regarding the first variation, in the lower left subfigure it is noticed the positive effect of the spectral weighting, since with just averaging the Ψ_{dp} presents a suspect downward trend at the end of the range. In general, it was noticed that the comparative effect of spectral weighting (other than less statistical fluctuations) is either negligible or positive and this is why it was the preferred method.

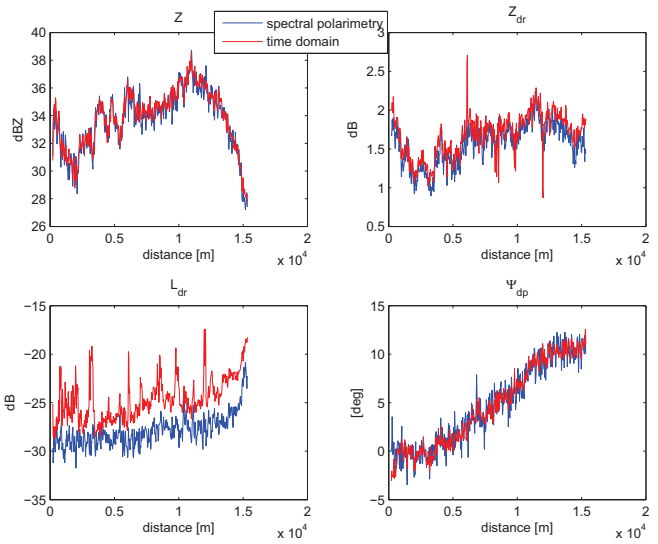

Figure 5.16: Comparison of the radar observables under the time domain and spectral polarimetric approach.

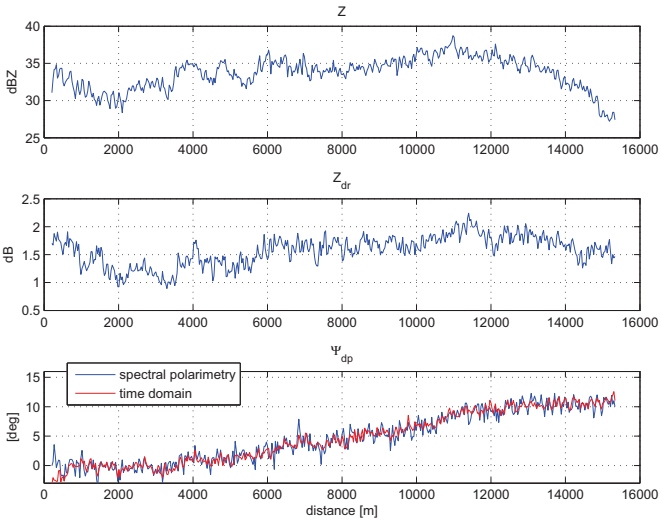

Figure 5.17: The range profiles for Z, Z_{dr} and Ψ_{dp}.

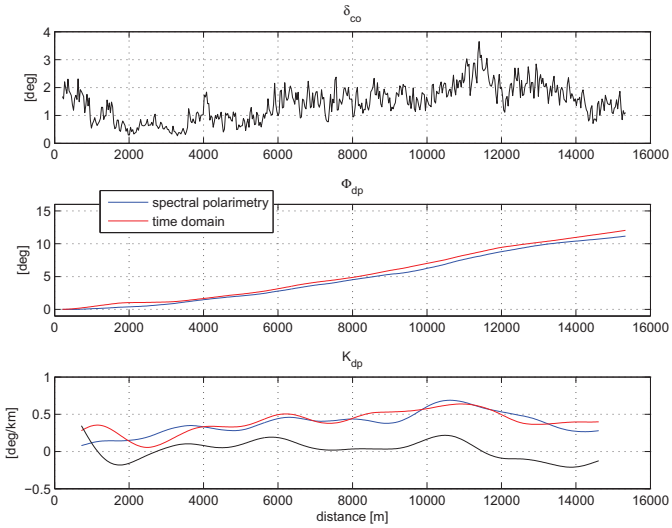

Figure 5.18: The range profiles for δ_{co}, Φ_{dp} and K_{dp}. The black curve is the $\bar{K}_{dp}^{\delta_{co}}$ bias.

Chapter 6

Assessment of results

As mentioned in Chapter 4, correct estimation of K_{dp} is a complicated task because it entails various processing steps that have to take place in advance: estimation of Ψ_{dp}, removal of δ_{co} in order to get Φ_{dp} and smoothing of the curve. When a smooth Φ_{dp} curve is obtained, an estimator of K_{dp} can be applied (Eq. 4.3). The estimated K_{dp} is then used for applications such as rain rate estimation. Rain rate estimators themselves are not exact relationships but best-fit curves so they have limited inherent accuracy. It is therefore essential that K_{dp} or any other observable to be estimated as accurately as possible before it is used in such ways. In this chapter we look into possible ways to assess the quality and correctness of the previous Φ_{dp} and K_{dp} estimation and gain further insight into the results.

6.1 Correlation with rain gauges

The most dependable way to have confidence in the estimated K_{dp} is to apply a rain rate estimation algorithm involving it (ideally K_{dp} alone in order to isolate effects from other estimated radar observables) and check for agreement with rain gauge measurements. This is because rain gauge measurements are typically regarded as the 'ground truth' being the reference for all other estimations. Seeking agreement with rain gauges measurements is generally a complicated task mainly for two reasons:

- rain gauges measure the rain on the ground surface, while rain rate estimators based on radar observables refer to a certain rain cell above the ground. Correlating them is possible under certain assumptions.
- rain gauges measure accumulation of rain, while rain rate estimators give instantaneous results that have to be integrated in time.

There are available rain gauges in the IDRA area (one network belonging to KNMI and the other to Wageningen University) however a correlation was out of the scope of the present thesis. It is believed that checking for agreement against these rain gauges is important for gaining confidence in IDRA measurements and estimations. At the moment, the main obstacle to this direction is that the estimation of K_{dp} is based on raw data files that are available not very

frequently. Frequent K_{dp} values (every few minutes) have to be available so that estimated rain rates can be integrated and compared against the rain gauges. That means that any K_{dp} estimation processing step (involving Φ_{dp} smoothing and δ_{co} removal) has to be implemented in the real-time processing scheme first.

6.2 Analytical computation

As mentioned before all the radar observables are mathematically defined as moments of the drop size distribution. If the dsd is known, the radar observables can be analytically computed and used as reference for the correctness of their estimation based on radar data. The dsd is possible to be retrieved by 2D disdrometer measurements, an instrument available near the Cabauw tower where IDRA is located. It is believed that 2D disdrometers measurements can offer valuable information regarding the specific meteorological conditions in the site of radar measurements which can be helpful in any case. Despite that, such an approach was not taken as it was out of the scope of the current thesis.

6.3 Self-consistency considerations

As stated above, once the DSD is known the radar observables can be calculated analytically. This implies that the observables themselves do not vary independently but they are correlated. Of course, this does not mean that there are only unique combinations of values, for example unique triplets of (Z, Z_{dr}, K_{dp}). In the same way there is actually a 2D scatterplot of Z and Z_{dr} values and not a unique curve expressing their mutual variation, there is a 3D scatterplot of triplets (Z, Z_{dr}, K_{dp}) where each point corresponds to a certain dsd, or equivalently a certain combination of the dsd parameters. Calculation of a best fit surface is possible so that one parameter is expressed as a function of the other two. An intuitive reasoning is that since there is a rain rate estimator as a function of Z and Z_{dr} and K_{dp} is closely linear to R, at least for the X-band (section 2.2), it should also be possible to express K_{dp} as a function of Z and Z_{dr}. This 'interconnection' of the radar observables is known as the self-consistency principle [16] and has been used for attenuation correction. In our case, we wish to use this principle to check the correctness of the Φ_{dp} and K_{dp} estimation. We can do that by deriving a relationship which will be used as a reference for the estimated K_{dp} values. This relationship is:

$$\mathrm{K}_{dp}^{sc} = K_{dp}(Z, Z_{dr}) = \alpha Z^{\beta} 10^{-\gamma Z_{dr}}, \text{ Z in linear scale and } Z_{dr} \text{ in dB} \quad (6.1)$$

and it means that to each couple of (Z,Z_{dr}) values corresponds a certain value of K_{dp}, in a best-fit sense. To sum up, we will try to come up with a relationship like Eq. 6.3 and check for agreement between the estimated K_{dp} and the one according to the self-consistency principle, ${K_{dp}}^{sc}$. Following a similar argument, δ_{co} may expressed through Z_{dr} as

$$\delta_{co} = a {Z_{dr}}^{b},$$

Z_{dr} in dB (6.2)

The intuitive reasoning for the above relationship is that both variables originate from the non-sphericity of the rain droplets, so they have a common physical basis. Also, Z_{dr} is expressed in dB so that in the limiting case where it becomes zero (spherical particles) δ_{co} will be zero as well.

The validity of this approach is based on the following assumptions:

1. Eq. 6.3 is mathematically meaningful, that is the dispersion of the (Z, Z_{dr}, K_{dp}) triplets in their 3D space is limited (high correlation) and thus able to be approximated by a surface.

2. The estimated values of Z and Z_{dr} used as inputs in Eq. 6.3 to get a reference for K_{dp} are correct.

Regarding the first point, it will be shown in section 6.5 that it holds. Most importantly, it has to be underlined that the validity of the fit (Eq. 6.3) from a *physical* prospective depends on the kind of dsd's considered. If we wish to apply this method reliably, then the range of dsd used to generate the dataset on which the regression will be carried out to get Eq. 6.3 should be as closely as possible to the actual meteorological conditions in the site of measurement. Otherwise, we will end up with a relationship which may be mathematically accurate, but wrong from a physical point of view, as it describes a different meteorological situation. In brief, Eq. 6.3 has to be calibrated to the actual rain event under consideration. The way and reasoning for doing so will be discussed further in section 6.5. Regarding the second point, at the moment there is confidence in the estimated Z and Z_{dr} values so that they are thought to be suitable to serve as references. Besides, Eq. 6.3 will be mainly used as a qualitative measure for assessing the correctness of Φ_{dp} and K_{dp} estimation and not in a quantitative sense. A special issue regarding Z_{dr} is addressed in Appendix B; at this point it is only noted that it has limited influence.

6.4 Drop size distribution retrieval

As mentioned in section 6.2, if the dsd could somehow be retrieved then K_{dp} could be computed analytically and used as a reference for the estimated one. Without using 2D disdrometers, the dsd may be retrieved by the measured Z and Z_{dr}. However, it is apparent that since the model for dsd being used is the gamma dsd involving 3 parameters (section 2.3) and there are only two known observables (Z and Z_{dr}), one parameter has to be assumed known and only then the other two can be retrieved. It is assumed that μ is known as the radar observables are less sensitive to it compared to N_w and D_o. Since Z depends on both N_w and D_o while Z_{dr} only on D_o, D_o can be retrieved first by Z_{dr} and then N_w. The validity of this approach is based on the following assumptions:

1. The actual dsd in the measurement location can be described by a gamma dsd model.

2. The estimated values of Z and Z_{dr} used as inputs to retrieve the dsd are correct.

Regarding the first point, only actual in situ 2D disdrometer measurements can verify its validity or not. However, the gamma dsd model is widely used and believed to be a reasonable approximation of the particle distribution, especially for common meteorological conditions. The second point has been discussed just before. In conclusion, we will try to retrieve the dsd from the measured Z and Z_{dr} and once the dsd is known K_{dp} will be computed analytically (K_{dp}^{dsd}) and used as reference for the estimated one and similarly for Ψ_{dp}.

6.5 Implementation

In this section, it is described how the approaches presented in sections 6.3 and 6.4 are implemented along with the reasoning and assumptions involved. Although these two approaches are different in implementation, they are both based on the measured Z and Z_{dr} as their only inputs. Theoretically, the dsd retrieval approach is expected to be more accurate to be used as a reference, provided μ is assumed correctly and Z and Z_{dr} are measured with high accuracy, since the self-consistency approach is a best-fit practice. However, these points are not easy to meet, so in the end there may be not any relative advantage over the self-consistency approach. In any case, we are interested in these methods as assessment tools for the Φ_{dp} and K_{dp} estimation rather than for detailed quantitative studies, meaning that further analysis into comparing them is not required.

The main point of implementation is being able to compute the radar observables analytically for a certain dsd, or equivalently for a certain selection of its parameters. For the case of Mie scattering, this is not a trivial task as there are not direct mathematical relationships as opposed to Rayleigh scattering. It is necessary to use a numerical method to compute the scattering amplitude from a single particle, which is then used as a basis for computing the radar observables due to an ensemble of particles. Examples of such a technique is the Fredholm integral method (FIM) [17] and the T-matrix method. The one used was the FIM as it was already implemented inside a Matlab toolbox allowing for systematic use and integration with the other routines used (Appendix C). By using this toolbox it is able to:

- define a gamma dsd by its three parameters and compute all the radar observables and the rain rate (R)
- define a range of dsd by considering a range for its parameters in order to get a dataset of observables and rain rate
- retrieve the dsd (derive N_w and D_o) by the measured Z and Z_{dr} provided that μ is assumed

We begin by deriving Eq 6.3. For this, a regression has to be applied on a dataset consisting of (Z,Z_{dr},K_{dp}) triplets. This dataset was generated by considering a certain range for the gamma dsd parameters, given in Table 1. This range of parameters is close to ([5],p538) where similar simulations were carried out. However, as discussed previously, this dataset should also be similar to the actual meteorological conditions of the rain event under consideration. In order to do this, combinations of (N_w,D_o,μ) that result in rain rate R greater than 20mm/hr were filtered out because they correspond to precipitation events

Table 6.1: The range of dsd parameters that resulted in the dataset of Fig. 6.1.

μ	k ($N_w = 10^k$ $[mm^{-1}m^{-3}]$)	D_o $[mm]$
-1:1:5	3:0.25:4.5	0.1:0.05:4.5

more intense than the observed ones. It has to be noticed that since no rain rate estimation was actually made, the threshold value of 20mm/hr was selected empirically based on inspection of the vast majority of the Z values and the corresponding R according to typical R(Z) relationships found in literature. The full and filtered dataset is given in Fig. 6.1.

It is seen that the scatter of K_{dp} with respect to Z and Z_{dr} is limited, so a relationship like 6.3 is mathematically meaningful. By applying regression, it was found that

$$K_{dp}^{sc} = 0.0005 Z^{0.9751} 10^{-0.3908 Z_{dr}} \quad (6.3)$$

The values of the parameters in the above relationship relate well with those given in [16] for S- and C-band. In our case, parameter β was found to be larger, which is offset by an also larger parameter γ. This difference is probably due to the different regression technique used, non-linear for [16] and linear in our case. It is noticed that the non-linear regression is the optimal one, so that means that the derived self-consistency relationships as presented here could be improved. The performance of the estimator is shown in Fig. 6.2.

Regarding Eq. 6.3, the δ_{co}-Z_{dr} scatterplot and performance of the estimator is given in Fig. 6.3. Although the MSE of the estimator is not as limited as before, still good results were obtained by using it since the smoothing of the Φ_{dp} curve is expected to eliminate small faults in δ_{co} removal. Also, the performance of the estimator deteriorates only for large values of Z_{dr} (larger than 2.5dB which corresponds on average to δ_{co} of about 5^o) which are not very common, at least for many consecutive rain cells. It was found that

$$d_{co}^{sc} = 0.3719 {Z_{dr}}^{2.8291} \quad (6.4)$$

Various rain rate relationships can also be derived as shown in Fig. 6.4. The parameters were computed by regression and are given in Table 2. It is seen that the best estimator is the R(K_{dp},Z_{dr})[1] followed by R(Z,Z_{dr}). Also, R(K_{dp}) although it depends on only one observable unlike the others still performs well. These general conclusions are in agreement with the literature ([7], [8]).

As mentioned in section 2.3, a shape-size model has to be selected so that the particle distribution can be modelled by a monoparametric dsd, that is

[1] R(Z,K_{dp},Z_{dr}) offers no noticeable improvement despite the additional inclusion of Z

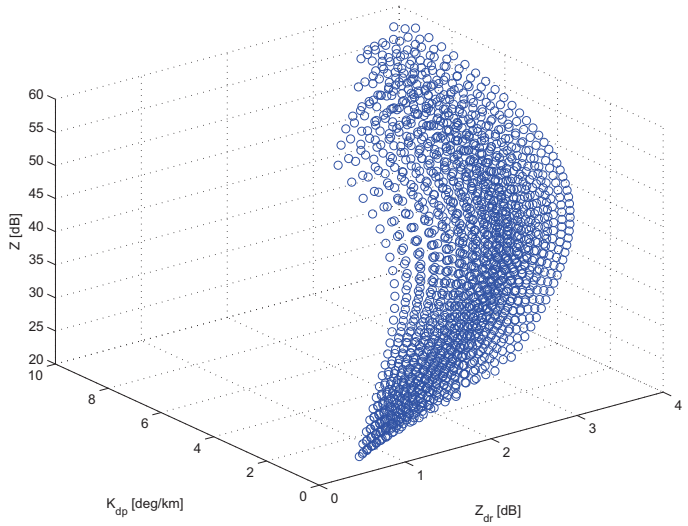

(a) Complete dataset.

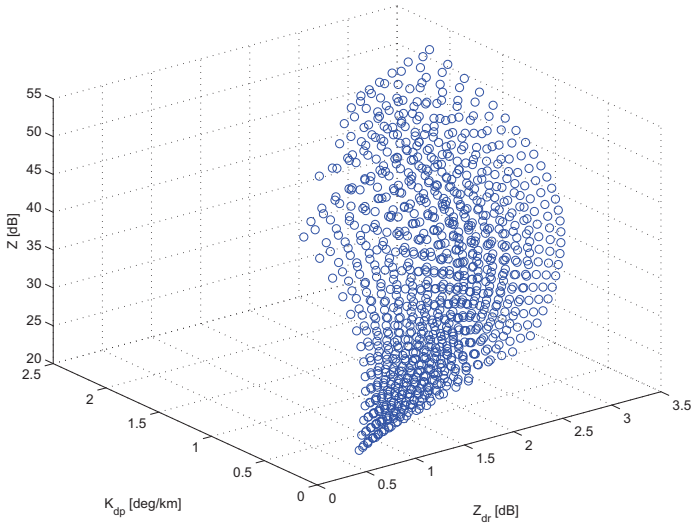

(b) Filtered so that it only contains points corresponding to R less than 20mm/hr.

Figure 6.1: The dataset of radar observables generated according to Table 1 in order to derive the self-consistency relationships.

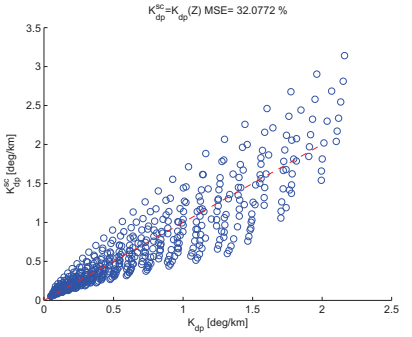

(a)

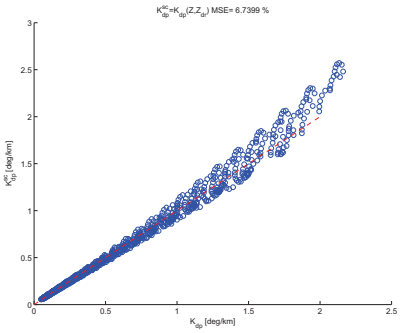

(b)

Figure 6.2: Performance of the self-consistency K_{dp}(Z,Z_{dr}) estimator (subfigure b). It is seen that it tends to result in overestimation for higher values of K_{dp}. It is noticed that an attempted K_{dp}(Z) (subfigure a) estimator fails (very high MSE); Z_{dr} is needed in order to 'capture' the origin of K_{dp} due to the non-sphericity of the rain drops.

Table 6.2: Rain rate estimators according to the dataset of Fig. 6.1 and the raindrop axis ratio model in [18]. In the second row the mean square error (MSE) is given.

X-band (9.475 GHz); T=25^oC; Z $[mm^{-6}m^{-3}]$ Z_{dr} $[dB]$ K_{dp} $[deg/km]$				
R(Z)	R(Z,Z_{dr})	R(K_{dp})	R(K_{dp}, Z_{dr})	R(Z,K_{dp}, Z_{dr})
$R = 0.083Z^{0.49}$	$R = 0.018Z^{0.91}10^{-0.47Z_{dr}}$	$R = 10.98{K_{dp}}^{0.84}$	$R = 17.8{K_{dp}}^{0.93}10^{-0.09Z_{dr}}$	$R = 8.37Z^{0.84}{K_{dp}}^{0.13}10^{-0.1Z_{dr}}$
39.1%	11.1%	12.1%	6.9%	6.8%

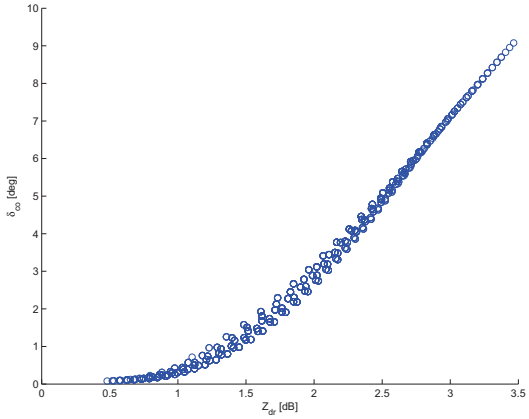

(a) δ_{co}-Z_{dr} scatter plot

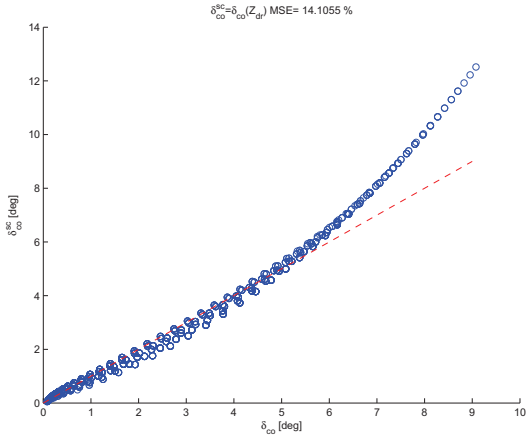

(b) Performance of $\delta_{co}(Z_{dr})$ estimator

Figure 6.3: Self-consistency estimator of δ_{co}. It is seen that it tends to result in overestimation for higher values of δ_{co} (about 5^0, corresponding to Z_{dr} of about 2.5dB). It is apparent that the variation of δ_{co} versus Z_{dr} is such that cannot be captured effectively in only one power-law expression over the whole range of values. It is suggested that two different power-law expressions may be used for future work, one up to the 5^0 region where the variation is closely linear, and another for the remaining range where the variation deviates from linear.

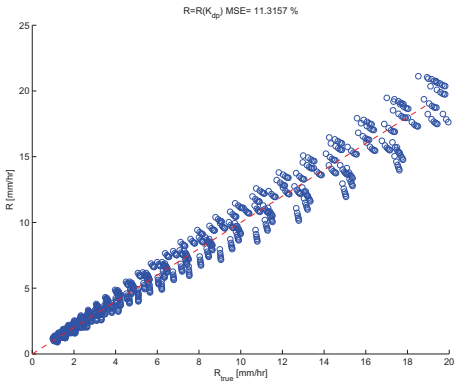

(a) R(K_{dp}) estimator.

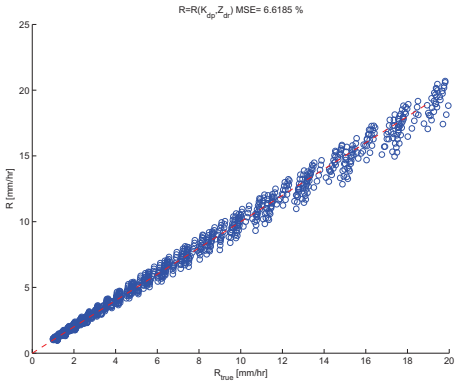

(b) R(K_{dp},Z_{dr}) estimator.

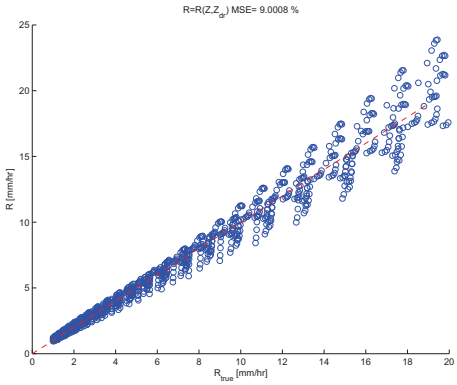

(c) R(Z,Z_{dr}) estimator.

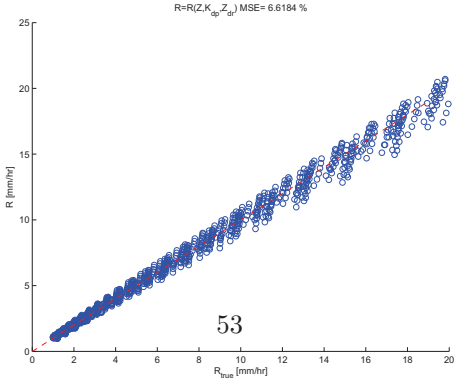

(d) R(Z,K_{dp},Z_{dr}) estimator.

Figure 6.4: Various possible rain rate estimators.

involving only D as an independent variable. The choice of such a model is not trivial as there are many available and it affects the computed radar observables for a certain dsd, especially the ones that originate from the anisotropy of the particles such as K_{dp} and Z_{dr}. The simulation toolbox offers the possibility to use various rain drop axis ratio models but only the Pruppacher and Beard [18] model was eventually used since it is rather common and good results were obtained with it. Still, the possible effects of different choice of the axis ratio model would be useful to be studied and be known in order eliminate sources of uncertainty.

At this point, the approach presented in section 6.3 has been implemented as we may compute a K_{dp}^{sc} and δ_{co}^{sc} from the measured Z and Z_{dr} and the self-consistency relationships. For section 6.4, a value for μ is assumed (along the whole range of the sector) and then N_w and D_o are retrieved. Once the dsd is retrieved, we may compute a similar K_{dp}^{dsd} and δ_{co}^{dsd} (not through an equation, but by using the FIM toolbox). Regarding the choice of μ, small values such as 0,1 or 2 seem more reasonable[2] as it has been reported in the literature that higher values are associated with more intense rain events ([19]). This is somehow expected, because increasing μ shifts the shape of the dsd more to the right (Fig. 2.2) to include a greater number of larger raindrops which are not expected to occur in the light to moderate rain events we are dealing with. A schematic representation of the two approaches is given in Fig. 6.5. Finally, it is noted that for some rain cells (typically near the radar origin) Z and Z_{dr} have NaN values meaning they are below the noise level. In such cases the self-consistency relationships cannot be applied so K_{dp}^{dsd} and δ_{co}^{dsd} are directly taken to be zero, which is the correct physical interpretation.

6.6 Results

We refer to the same case presented in section 5.2 (Case study B). In Fig. 6.6 the result of the dsd retrieval can be seen, that is the profiles for N_w and D_o (μ=1 was assumed). The reconstructed Z and Z_{dr} profiles completely coincide with the measured ones, so no error takes place at this step. Having retrieved the dsd, δ_{co}^{dsd} and K_{dp}^{dsd} can be computed and thus the Ψ_{dp}^{dsd} and Φ_{dp}^{dsd} range profiles as well. Similar procedure can be followed for the self-consistency approach; K_{dp}^{sc} and δ_{co}^{sc} are computed directly in this case from their estimators and $\Psi_{dp}^{sc}, \Phi_{dp}^{sc}$ profiles can be reconstructed as well. The reconstructed Φ_{dp} for the dsd retrieval approach is calculated as $\Phi_{dp}^{dsd} = 2\int_{r=0}^{r=r_{end}} K_{dp}^{dsd}(r)dr$, where the multiplying factor of 2 accounts for the two-way propagation of the radar beam, while $\Psi_{dp}^{dsd} = \Phi_{dp}^{dsd} + \delta_{co}^{dsd}$ since δ_{co} originates only once at the radar resolution volume. For the approach based on self-consistency the relationships become $\Phi_{dp}^{sc} = 2\int_{r=0}^{r=r_{end}} K_{dp}^{sc}(r)dr$ and $\Psi_{dp}^{sc} = \Phi_{dp}^{sc} + \delta_{co}^{sc}$.

First, a comparison of the two approaches is shown in Fig. 6.7. It is seen that there is good agreement on K_{dp} and δ_{co}, so the respective Φ_{dp} and Ψ_{dp} profiles in Fig. 6.8 agree. This is expected since both are based on the same physical basis, that all the radar observables are interrelated. A cumulative deviation is observed for the phase profiles, however this is relatively small (about 1 degree at the end of the range). Next, a comparison between the results of the dsd

[2]for the dsd retrieval curves following in the next section, the selected value of μ is given in the figures

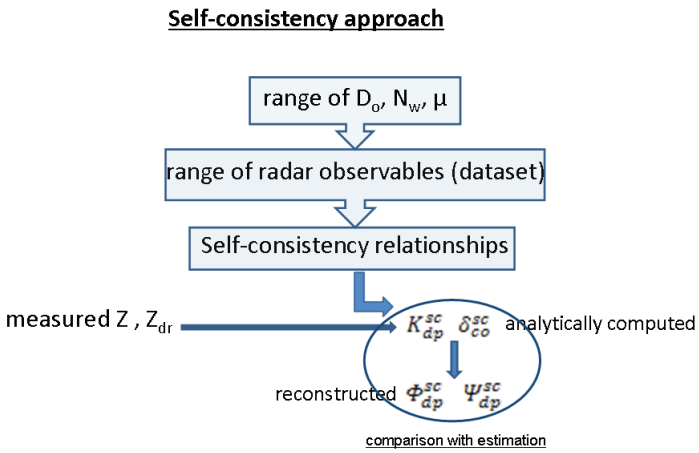

(a) Self-consistency approach

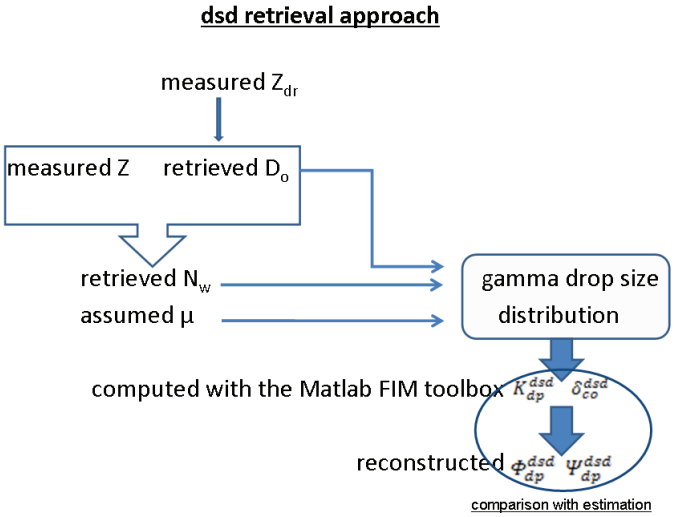

(b) dsd retrieval approach

Figure 6.5: A schematic representation of the two assessment methods. The objective is the comparison of these reference, expected values with those estimated directly from radar signal measurements.

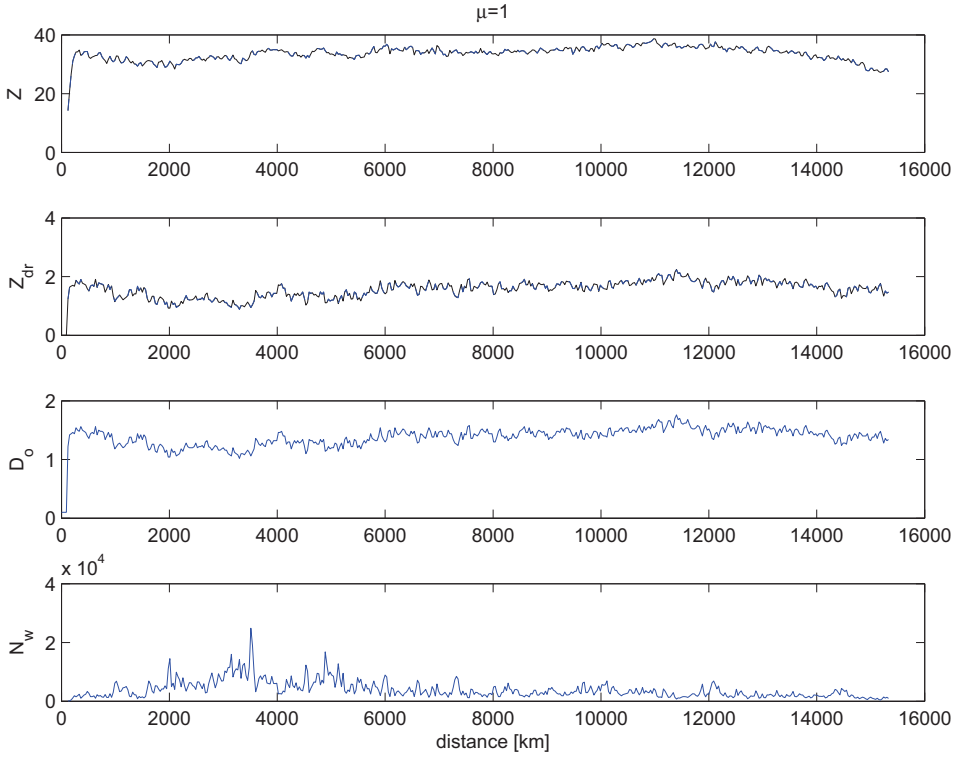

Figure 6.6: Drop size distribution retrieval for Z and Z_{dr} of Fig.5.17 (case B). The reconstructed Z and Z_{dr} profiles are given by the blue curves while the original ones by the dashed black curves and they coincide.

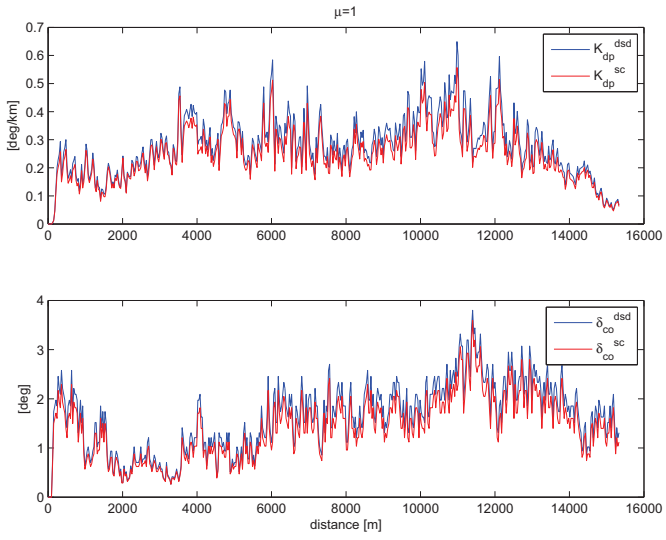

Figure 6.7: Comparison of the results from the self-consistency and dsd retrieval approach (case B).

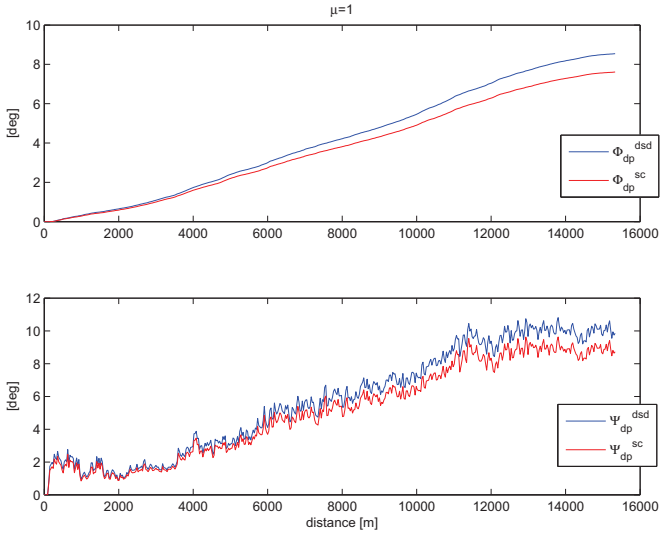

Figure 6.8: Comparison of the reconstructed Ψ_{dp} and Φ_{dp} profiles (case B).

retrieval method and the actual estimation regarding Ψ_{dp}, Φ_{dp} and K_{dp} is given in Fig. 6.9. The respective for the self-consistency approach is Fig. 6.10.

It is seen that there is close agreement between the estimated (through measurements) and expected (through either the self-consistency or the dsd retrieval method) Ψ_{dp} and Φ_{dp} profiles. However, a growing deviation is observed after about 6km, with the estimated Φ_{dp} and Ψ_{dp} growing continuously more than the expected ones. This deviation reaches up to 3 degrees at the end of the range so it cannot be dismissed as negligible. It is believed that it is caused by attenuation, because attenuated Z and Z_{dr} values result in underestimation of the expected Φ_{dp} and Ψ_{dp}. This will be examined in the next chapter. Regarding the comparison of K_{dp} curves, it should be noted that the measured curves include an inherent smoothing due to the K_{dp} estimator which works on range segments while the expected K_{dp} curves are per range point (one rain cell only). Therefore, being different in nature, for a more realistic comparison the expected K_{dp} curves should be smoothed with a smoothing filter of the same N used for the K_{dp} estimator, such as the one used for Φ_{dp} smoothing. This is shown in Fig. 6.16.

The respective results for the sector discussed in section 5.1 are now given in Fig. 6.11-6.15. The above conclusions apply for this case as well. It is again noticed a growing deviation for the differential phase profiles which is now more pronounced (about 7^o at the end) which is suggestive of a systematic underlying reason which could be the attenuation of the radar beam.

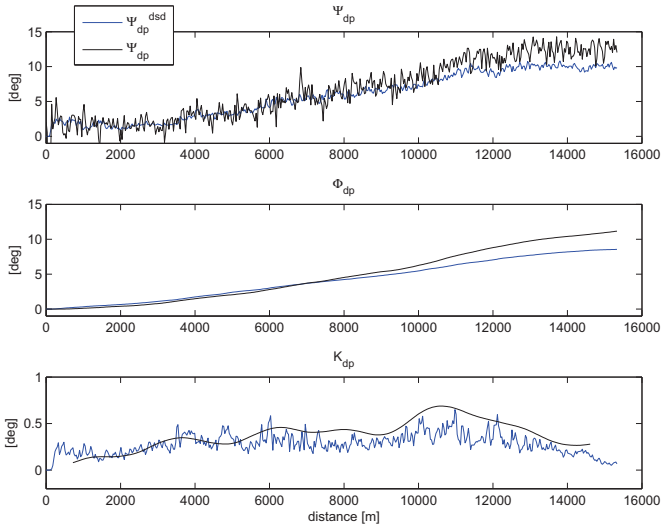

Figure 6.9: Comparison of the results (case B) from the dsd retrieval approach (blue curve) and the actual estimation of Ψ_{dp}, Φ_{dp} and K_{dp} (black curve).

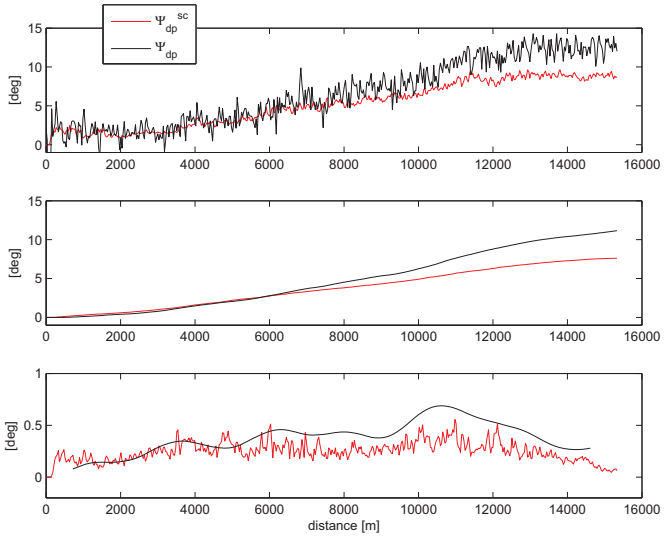

Figure 6.10: Comparison of the results (case B) from the self-consistency approach (red curve) and the actual estimation of Ψ_{dp}, Φ_{dp} and K_{dp} (black curve).

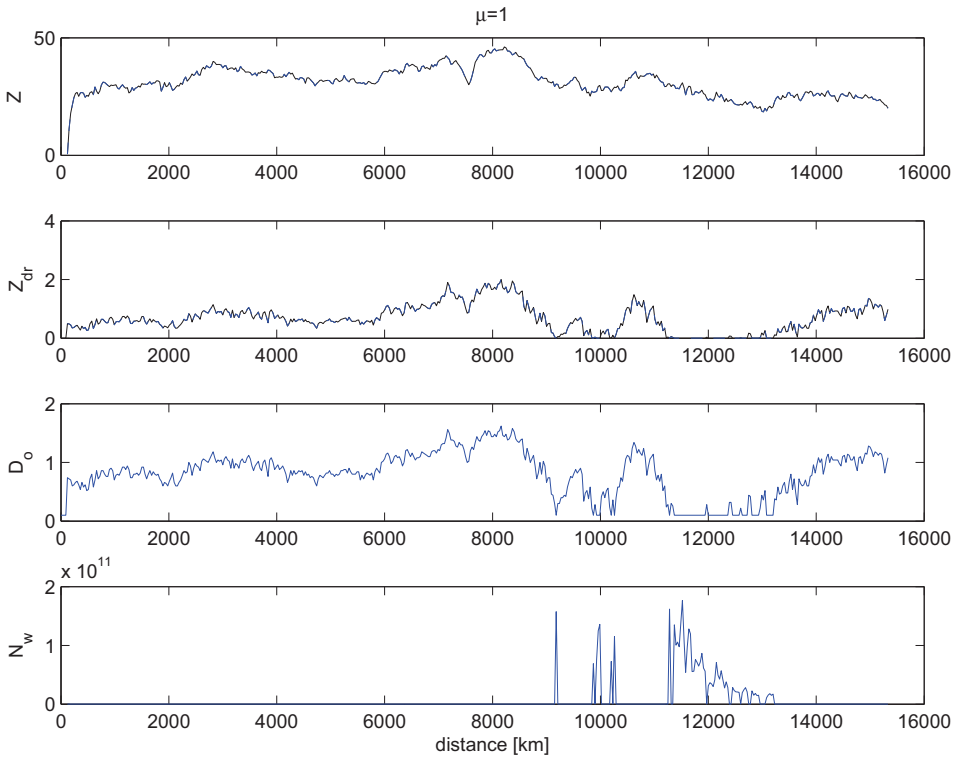

Figure 6.11: Drop size distribution retrieval for Z and Z_{dr} of Fig.5.8. The reconstructed Z and Z_{dr} profiles are given by the blue curves while the original ones by the dashed black curves and they coincide. It is noticed that for rangebins where D_o is very low (very low Z_{dr}), the error in N_w estimated values is very large. In fact, in the shown N_w profile above, due to non-optimal vertical axis zoom only these spike values appear.

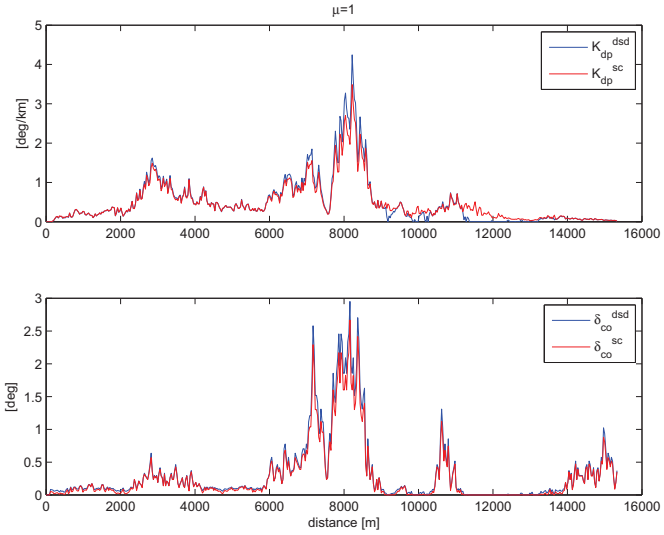

Figure 6.12: Comparison of the results from the self-consistency and dsd retrieval approach (case A).

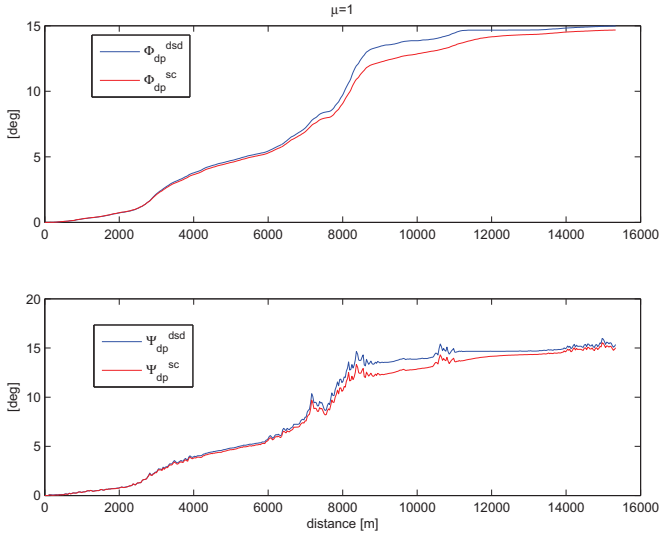

Figure 6.13: Comparison of the reconstructed Ψ_{dp} and Φ_{dp} profiles (case A).

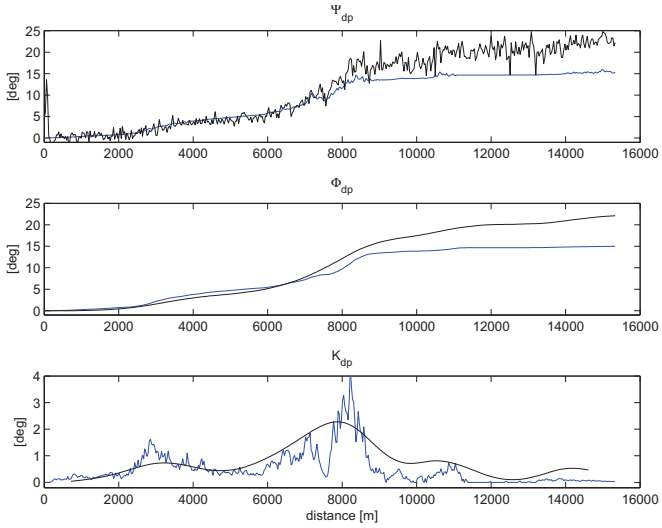

Figure 6.14: Comparison of the results (case A) from the dsd retrieval approach (blue curve) and the actual estimation of Ψ_{dp}, Φ_{dp} and K_{dp} (black curve).

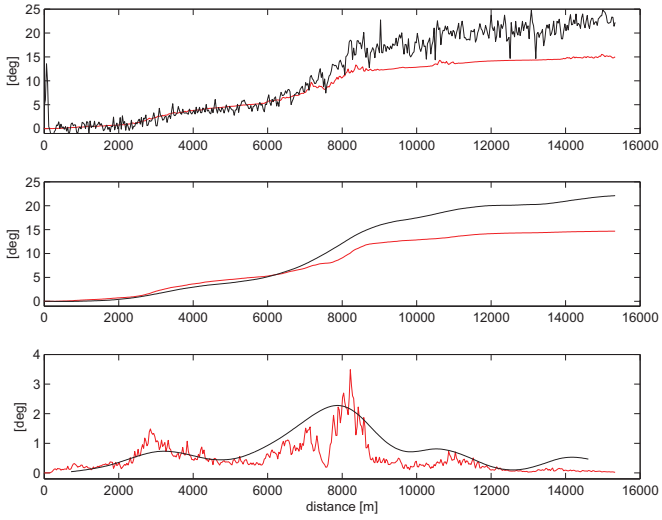

Figure 6.15: Comparison of the results (case A) from the self-consistency approach (red curve) and the actual estimation of Ψ_{dp}, Φ_{dp} and K_{dp} (black curve).

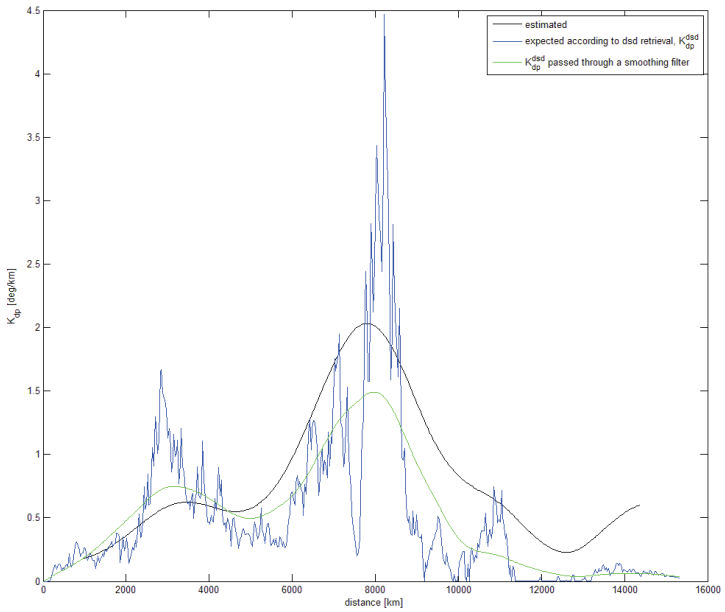

Figure 6.16: Comparison of the estimated and expected K_{dp} curves while trying to account for their different qualities by smoothing the expected ones.

Chapter 7

Attenuation

In X-band, the attenuation may no longer be ignored even for light to moderate rain paths. The attenuation of the radar signal is quantitatively described by the specific attenuation (A_{hh}) and specific differential attenuation (A_{dp}) which affect Z and Z_{dr} respectively. Attenuated Z and Z_{dr} will result in underestimation of the rain rate along with shortening of the effective radar range over which reliable atmospheric observations may be carried out. The latter can be dealt with increasing the transmission power, but even in this case A_{hh} and A_{dp} will still result in distorted Z and Z_{dr} range profiles which obfuscate their analysis. For these reasons, an attenuation correction algorithm is believed to be of necessity for IDRA data when the intensity of the rain path is not negligible. Our motivation is supported by the results presented in the previous chapter where a disagreement was observed between the measured and expected values of Φ_{dp} at long ranges, which was assumed to be due to attenuation effects.

7.1 Attenuation correction based on Φ_{dp}

The simplest attenuation correction algorithm for Z is based on assuming a linear relationship $A_h \cong \alpha K_{\mathrm{dp}}(r)$, where A_h is in $dBkm^{-1}$ and K_{dp} is in $degkm^{-1}$. By definition of the specific attenuation, the attenuated reflectivity Z' can be expressed as

$$\mathrm{Z}'_h(r) = Z_h(r) - 2\int_0^r A_h(s)ds = Z_h(r) - 2\alpha\int_0^r K_{\mathrm{dp}}(s)ds = Z_h(r) - \alpha[\Phi_{\mathrm{dp}}(r) - \Phi_{\mathrm{dp}}(0)] \quad (7.1)$$

and since the initial value for Φ_{dp} is $\Phi_{\mathrm{dp}}(0) = 0$, it follows that

$$\mathrm{Z}_h(r) = Z'_h(r) + \alpha\Phi_{\mathrm{dp}}(r) \quad (7.2)$$

According to Eq. 7.2, the unattenuated or corrected Z (in dBZ) can be computed if the respective value of Φ_{dp} multiplied by the coefficient α is added to the measured one, for each rangebin. For Z_{dr}, a similar analysis holds with the

Table 7.1: Effect of temperature on complex permittivity of water (f=9.475GHz) and attenuation correction coefficients

Temperature (^oC)	ϵ_r	α	β
15	59.6177+34.7621i	0.25	0.0529
20	62.3766+31.7862i	0.26	0.053
25	64.1842+28.8638i	0.26	0.053
30	65.2438+26.1288i	0.28	0.054

only difference being that A_{hh} is now replaced by $A_{dp}(r)$ and coefficient α by coefficient β, $A_{dp} = \beta K_{\rm dp}(r)$ (Z_{dr} is in dB and A_{dp} in $dBkm^{-1}$):

$$\mathrm{Z}'_{dr}(r) = Z_{dr}(r) - 2\int_0^r A_{dp}(s)ds = Z_{dr}(r) - 2\beta\int_0^r K_{\rm dp}(s)ds = Z_{dr}(r) - \beta[\Phi_{\rm dp}(r) - \Phi_{\rm dp}(0)] \quad (7.3)$$

$$Z_{dr}(\mathrm{r}) = Z_{dr}{}'(r) + \beta\Phi_{\rm dp}(r) \quad (7.4)$$

Based on the simulation approach, scatterplots of $A_h - K_{dp}$ and $A_{dp} - K_{dp}$ and the performance of their estimators are given Fig. 7.1-7.4 in order to check the assumption of linearity and determine the actual values for coefficients α and β. It is seen that the assumption of linearity is only true for small values of K_{dp}, namely less than 1deg/km, therefore the validity of the consecutive estimators is limited. Additionally, even for such a small linear region, the scatter of the estimators is considerable (Fig. 7.2 and 7.4) and the origin of this should be studied more closely. Still, the computed values for α and β agree well with the reported ones in the literature ([5],p494). A more pronounced discrepancy can be noted regarding the value of β which was initially thought that it could be attributed to the temperature which was taken to be 20^oC, instead of averaging over $0 - 30^o$C as is ([5],p494). Temperature has an effect on the coefficients α and β because it affects the permittivity of the rain drops. However, as shown on Table 7.1 this effect is only minimal and consequently it is believed that any discrepancies related to the attenuation coefficients originate from the choice of the drop axis ratio model.

At this point Eq. 7.2 and Eq. 7.4 are applied to the range profiles of Z and Z_{dr} of the previous section in order to get their 'true', un-attenuated profiles (Fig. 7.5). It is clearly seen the distorting effect of attenuation on both after about 6km since it is cumulative. We now use these corrected profiles of Z and Z_{dr} as inputs for the self-consistency and dsd retrieval methods which result in the expected Φ_{dp} for case B (Fig. 7.7). The previous results are repeated in Fig. 7.6 where it is seen that the disagreement between the measured and expected Φ_{dp} range profiles begins at the same point where attenuation starts to occur for Z and Z_{dr}. Correcting for attenuation 'lifts' Z and Z_{dr} up after this point, and subsequently the expected Φ_{dp} (Φ_{dp}^{sc} or Φ_{dp}^{dsd}) which now is in good agreement with the measured one (Fig. 7.7). Therefore, we conclude that the

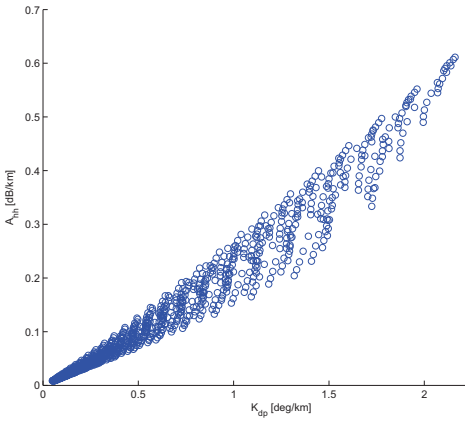

Figure 7.1: A_{hh}-K_{dp} scatter plot.

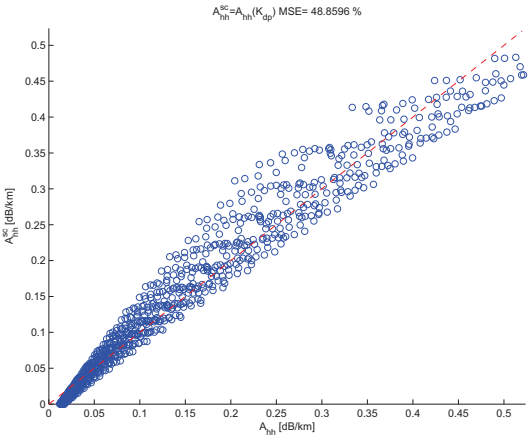

Figure 7.2: Performance of $A_{hh}(K_{dp})$ estimator (α=0.26, 20^{o}C).

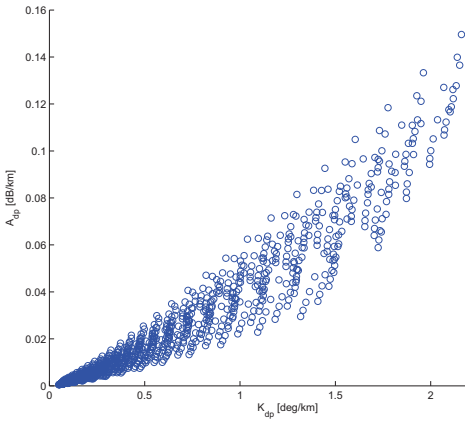

Figure 7.3: A_{dp}-K_{dp} scatter plot.

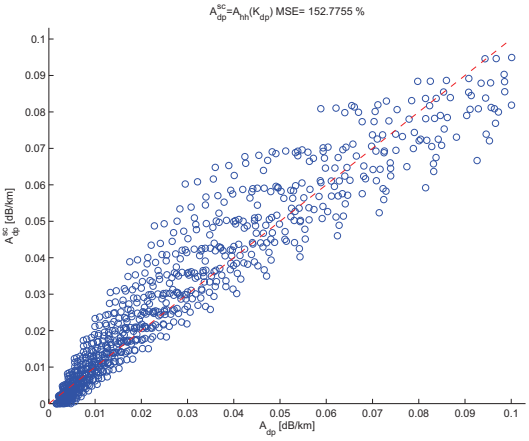

Figure 7.4: Performance of $A_{dp}(K_{dp})$ estimator (β=0.053, 20^{o}C).

initial disagreement was indeed due to attenuation and the agreement reached after correction is indicative of good performance of both the Φ_{dp} estimation on one hand and the simple attenuation correction algorithm on the other. The corresponding results for the other case are shown in Fig. 7.8- 7.9.

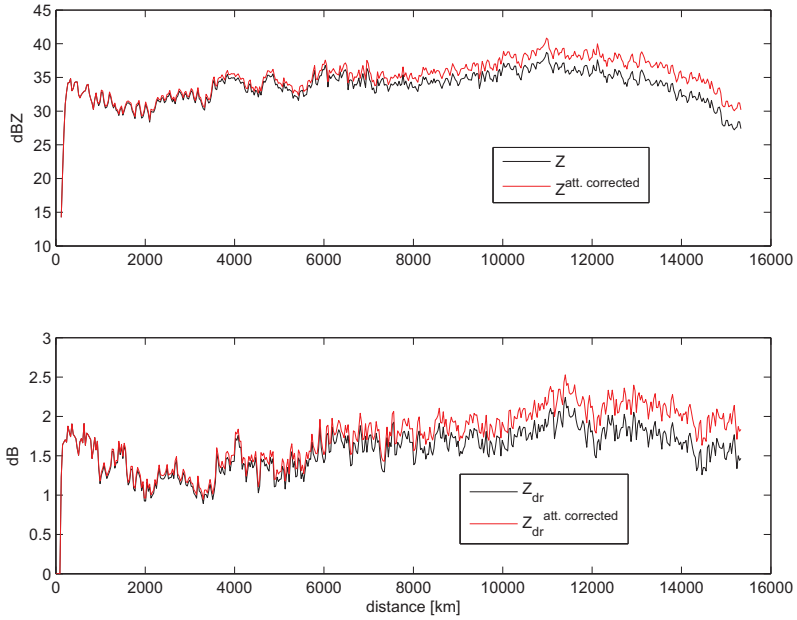

Figure 7.5: Attenuation correction for the Z and Z_{dr} range profiles of Fig. 5.17 (case B).

So far it has been said that attenuation of Z and Z_{dr} will result in underestimation of the expected Φ_{dp} and Ψ_{dp} profiles. However, according to Eq. 6.1 the opposite may also occur. The attenuation of Z and Z_{dr} have different impacts on the expected K_{dp}: attenuated Z results in underestimation while attenuated Z_{dr} actually results in overestimation. Their combined result may be either one, at least in theory. However, in practice (Appendix A) it has been observed that attenuation results in underestimation of the expected K_{dp} and therefore of the expected differential phases.

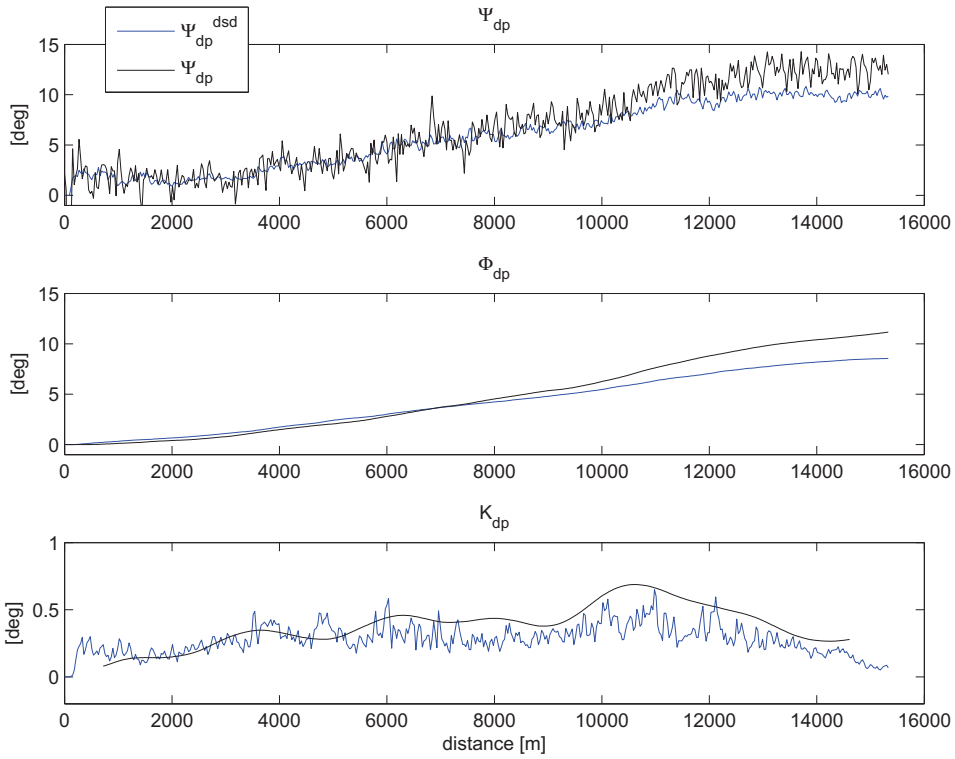

Figure 7.6: Fig. 6.9 repeated for comparison with Fig. 7.7. It is seen that the deviation starts to occur at the same point as the attenuation, indication that the effects are correlated. The curves in black colour represent the estimated parameters, while the ones in blue the expected according to the dsd retrieval approach.

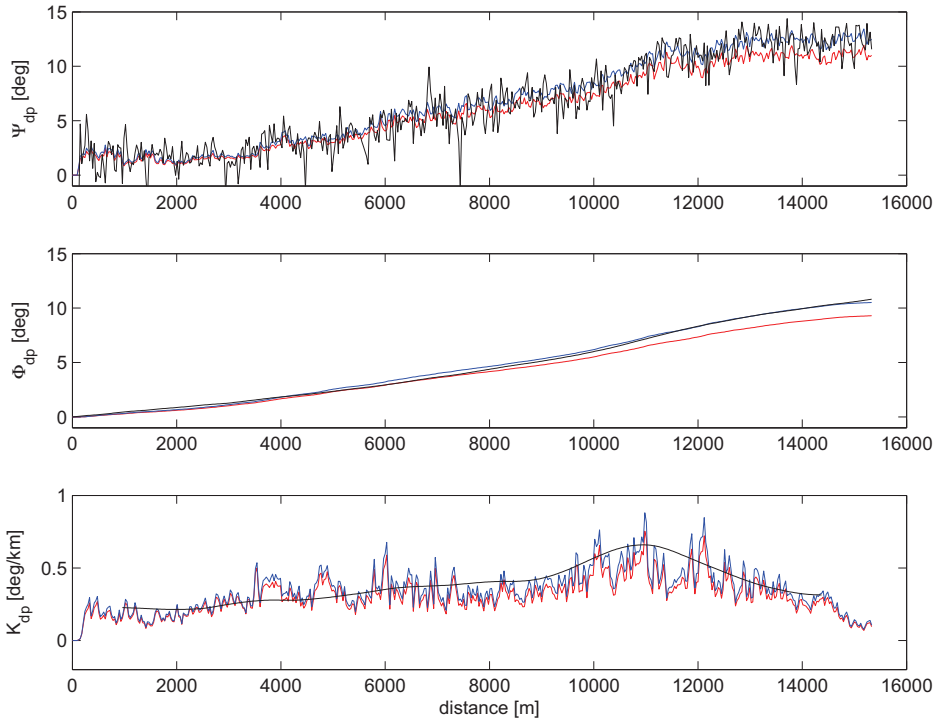

Figure 7.7: Correcting for attenuation results in better agreement between expected and estimated Φ_{dp} and Ψ_{dp} range profiles (case B). The curves in black colour represent the estimated parameters, while the ones in blue the expected according to the dsd retrieval approach and the ones in red the expected according to the self consistency approach.

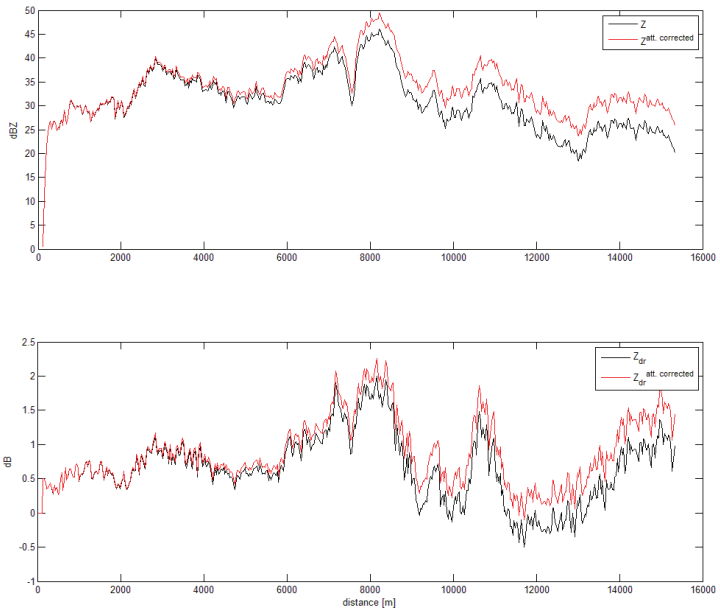

Figure 7.8: Attenuation correction for the Z and Z_{dr} range profiles of case A.

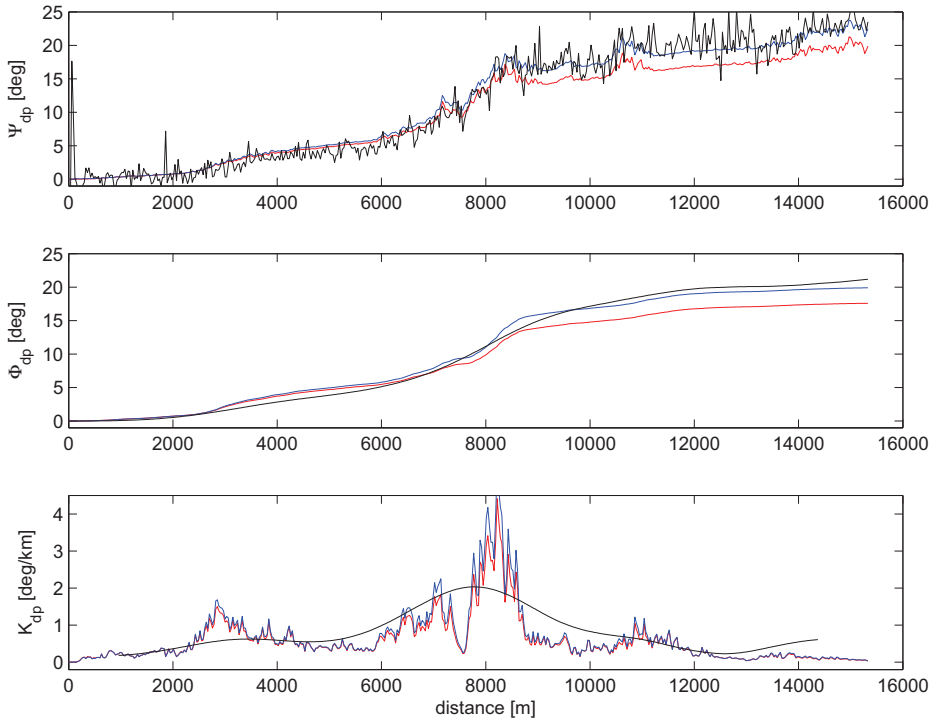

Figure 7.9: Correcting for attenuation results in better agreement between expected and estimated Φ_{dp} and Ψ_{dp} range profiles (case A). Again, the curves in black colour represent the estimated parameters, while the ones in blue the expected according to the dsd retrieval approach and the ones in red the expected according to the self consistency approach.

7.2 Attenuation and $\delta_{co}(Z_{dr})$

Since attenuation correction for Z and Z_{dr} depends on Φ_{dp}, a vicious circle is encountered: Φ_{dp} has to be available first, but Φ_{dp} estimation assumes δ_{co} removal which depends on Z_{dr}. This means that un-attenuated Z_{dr} has to be available first as well, otherwise if we are based on the attenuated Z_{dr}, δ_{co} estimation and removal may not be exact and this will induce bias in Φ_{dp}. Also, erroneous δ_{co} will result in bias in the K_{dp} estimation as explained in Chapter 4. Nevertheless, these issues are merely mentioned for future reference and no further investigation was attempted. In the case of attenuation correction, studying further the uncertainties in the corretion relationships is considered to be of higher priority. In the case of K_{dp} estimation, it is believed that the inherent smoothing of the estimator smooths away small errors coming from problematic δ_{co} removal.

Chapter 8

Conclusions

The main objective of this thesis was the estimation of the K_{dp} radar polarimetric variable. K_{dp} is derived from Φ_{dp} both under the time domain and spectral polarimetry approach. The estimation of Φ_{dp} is presented because the processing steps directly affect the K_{dp}, so that the estimation of K_{dp} is explained in an analytical way as a whole with the starting point being the IDRA raw data files. Since there are two approaches for the estimation Φ_{dp}, the same holds for K_{dp}. Emphasis was given on the spectral polarimetry as it is used for IDRA. Although the time domain technique is the actual standard, the gain of spectral polarimetric processing is better performance in removing non-atmospheric echoes. As this can be advantageous in such cases, it is the reason for focusing on a spectral polarimetric estimation of K_{dp} in order to remove dependency on the time domain technique for any radar observable. The spectral polarimetry and time domain Φ_{dp} were compared against each other and good agreement was observed; therefore the respectively derived K_{dp} are in good overall agreement as well. For cases were discrepancies are observed, the proposed strategy is to take the time domain curves as references and trace back the processing steps of the spectral polarimetry even up to the initial Doppler spectra. This is because the spectral polarimetry approach involves more processing and choices of threshold values.

On the other hand, the presented Φ_{dp}, Ψ_{dp} and K_{dp} curves were attempted to be compared against the expected, reconstructed ones through a self-consistency or dsd retrieval approach in a way that also accounts for possible effects of attenuation. Based on cases A&B and Appendix A, and despite the assumptions and uncertainties involved, the results are believed to be satisfactory and the following are concluded:

- the good self-consistency of the IDRA observables
- the potential of IDRA measurements for dsd retrievals
- the potential of implementing an attenuation correction algorithm, useful for all type of IDRA applications, based on Φ_{dp}
- the potential of a successful δ_{co} removal scheme; although the δ_{co} bias in K_{dp} was not found to be troublesome, it is useful being able to remove it, as for stronger rain events it may prove to affect a potential rain rate

estimation accuracy. In any case, its removal is crucial for any kind of assessment, qualitative as presented here or even quantitative, since as long it is involved the true Φ_{dp} cannot be retrieved from Ψ_{dp}.

- Appropriate sectors have to observed for a sufficient time frame and the estimated $R(K_{dp})$ has to be correlated with the rain gauges measurements. This work is greatly facilitated since the routines and processing algorithms for correlation of radar estimated rain rates with rain gauges have already been implemented by previous work for the $R(Z)$ estimators. The estimation of K_{dp} was attempted to be as modular as possible so that various possible choices for the involved parameters can be studied and compared. By substituting $R(Z)$ with $R(K_{dp})$, the performance of the $R(K_{dp})$ estimator can be assessed for different configurations (length of the smoothing interval N for Φ_{dp}, choice of the $\delta_{co}(Z_{dr})$ relationship parameters etc). In the end it will be concluded if the estimation of K_{dp} is correct and what values for the parameters are more accurate. Regarding rain rate estimation, at the moment it is not certain the potential of K_{dp} for rain rate estimation; this is due to the weak values of K_{dp} observed, usually below 1deg/km. The reflectivity Z should be at least 30 dBZ for K_{dp} to start becoming discernible (0.2deg/km). However, it increases quickly to around 1deg/km as Z rises higher (35-40dBZ). When Z surpasses 40dBZ, the K_{dp} approaches the 2deg/km vicinity. Although intense rain events are not very common at the moment, it is believed that they could be more pronounced in the future which would facilitate K_{dp} applications.

- The next step will be essential if the results from the previous one are not satisfactory enough, but also important in any case: the analysis of the disdrometer measurements available at the Cabauw site. These will prove very useful as they give direct insight into the drop size distribution, for which only assumptions can be made. The most fundamental parameter that has to be modelled with good certainty is the rain drop axis ratio which affects the results. Additionally, these data are important for deriving relationships such as $\delta_{co}(Z_{dr})$, $A_{hh}(K_{dp})$, $A_{dp}(K_{dp})$ outside of the simulation approach. Considering the rain gauge approach, the appropriate choices for the parameters of such relationships can be derived rather heuristically by trial and error. On the contrary, when disdrometer data are taken into account these choices are possible to be supported by direct measurements and scientific reasoning (a good candidate is the issue of the choice of μ). However, the work required is more demanding.

It is believed that the above two steps should be the focus of future work because they advance into extended measurements and techniques close to the IDRA objectives rather than attempting to improve small details. Trying to improve the following issues is regarded as complementary:

- altough from a processing point of view the issue of the wrong offset for the Ψ_{dp} can be overcome, it would be useful to determine the actual cause with certainty by observing this variability from sector to sector and from time to time.

- reducing the variation for the spectral polarimetry estimation of Φ_{dp} so it is comparable to the time domain
- studying the influence of non-homogenous rain path on the K_{dp} estimator is also suggested as it is a factor of uncertainty at the moment. It may also point to the necessity of a better smoothing and K_{dp} estimation approach, based on local, unequal range segments. However, taken into account the current assessment results for K_{dp}, that do not take it into account, its influence is not thought to be crucial.

Consequently, it is believed that despite the uncertainties it can be argued that there are indications for the correct estimation of Ψ_{dp}, Φ_{dp} and K_{dp} based on combined radar measurements and simulations. In any case, the lack of a known reference, which is a defining factor for remote sensing studies, eventually demands extensive studies only to lower the level of uncertainty by little. It is hoped that the work presented in this thesis is sufficiently methodological so it will be accessible enough for future corrections, improvements and extensions.

Appendix A

Extended results

In this Appendix results obtained in the same way as the ones presented in Chapters 5-7 are given for various sectors (azimuth directions) of various raw data files as listed below. Files 1-3 belong to the rain event of case study A, while the rest to case study B. The filenames also denote the specific time of acquisition (UTC). On the next page the reflectivity PPI corresponding to each file are shown. From these PPI some sectors were selected and processed in the same way described in Chapters 5,6 and 7. The layout of the results is as shown in Fig. A.1.
1:R2008-8-1_0-0-0.bin 2:R2008-8-1_1-0-0.bin
3:R2008-8-1_2-0-0.bin 4:R2009-5-25_20-13-0.bin
5:R2009-5-25_20-23-0.bin 6:R2009-5-25_20-33-0.bin
7:R2009-5-26_1-0-1.bin 8:R2009-5-26_1-30-1.bin
9:R2009-5-26_2-0-1.bin 10:R2009-5-26_4-0-1.bin

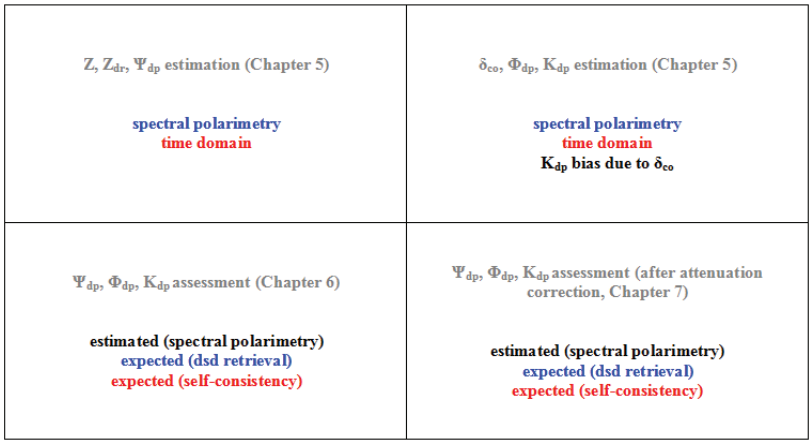

Figure A.1: On each page the results from processing a certain sector are presented, given in four plots as depicted, in terms of the grouping of the curves (grey font) and the meaning of each one (coloured font).

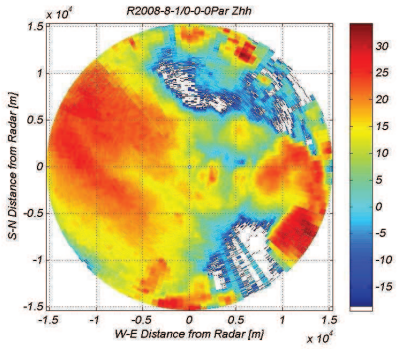

(a) 1

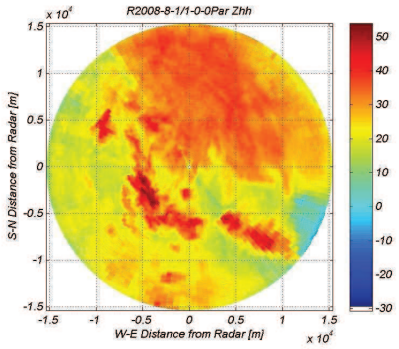

(b) 2

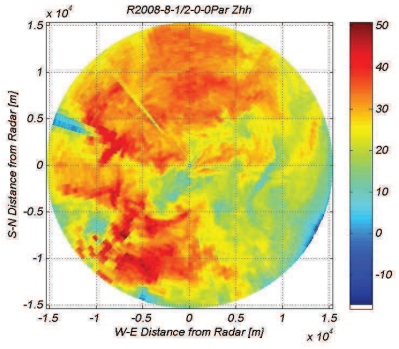

(c) 3

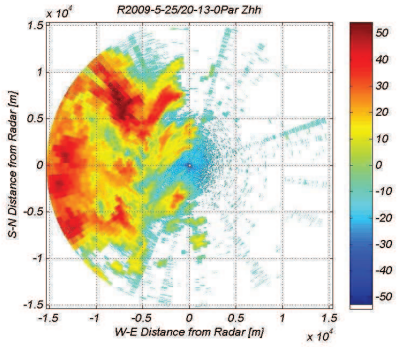

(d) 4

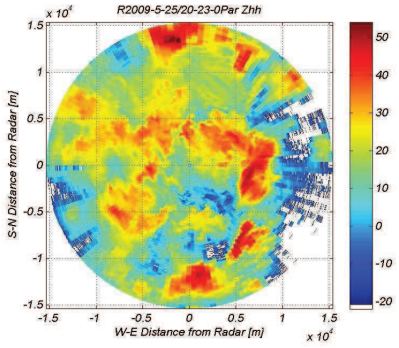

(e) 5

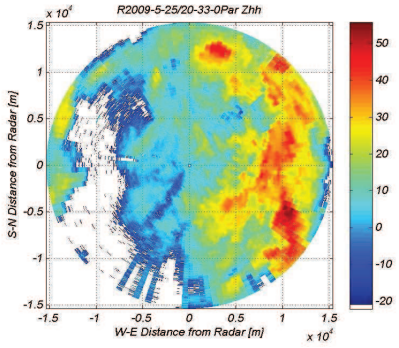

(f) 6

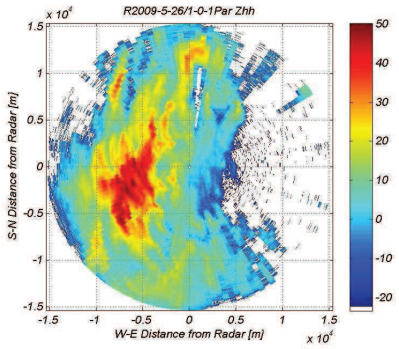

(g) 7

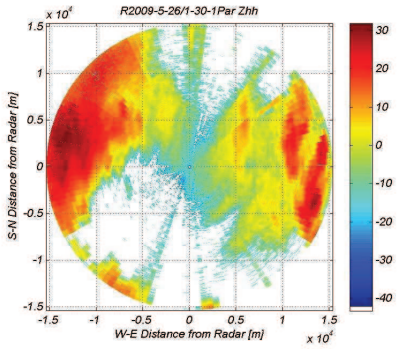

(h) 8

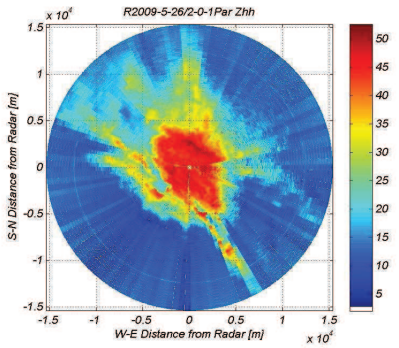

(i) 9

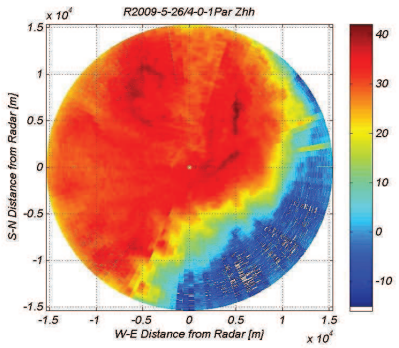

(j) 10

case:**1** sector:**280** In this case the reflectivity is too low ($30dBZ$) so that K_{dp} stays below 0.2deg/km. However, the time domain and spectral polarimetry Ψ_{dp} curves agree on their shape and total phase excursion, about 2^o. It is noticed that the shape of time domain Φ_{dp} is distorted by spurious noisy spikes around 10 and 13km.

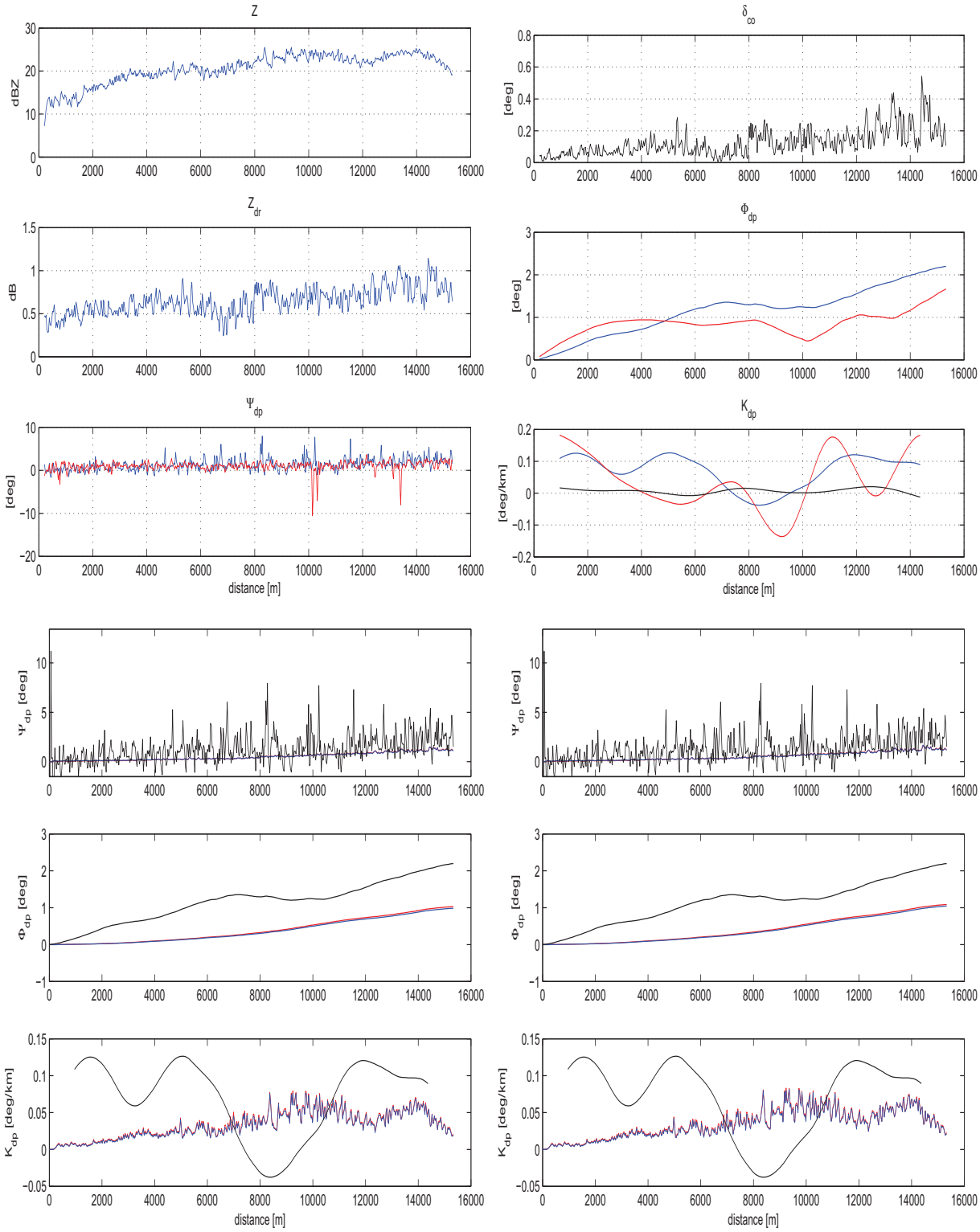

case:**2** sector:**0** For this sector the reflectivity lies in the 30-40dBZ range. Up to about 8km it stays under 35dBZ so K_{dp} is closely below what we consider its detection value (0.2deg/km). For the other part where 35<Z<40dBZ it is seen that it rises above this boundary value. The assessment curves also agree with the estimation, and attenuation correction results in improved agreement. In this case the K_{dp} bias due to δ_{co} ($\bar{K}_{dp}^{\delta_{co}}$) takes non-negligible values, which means more than the low limit of 0.2deg/km.

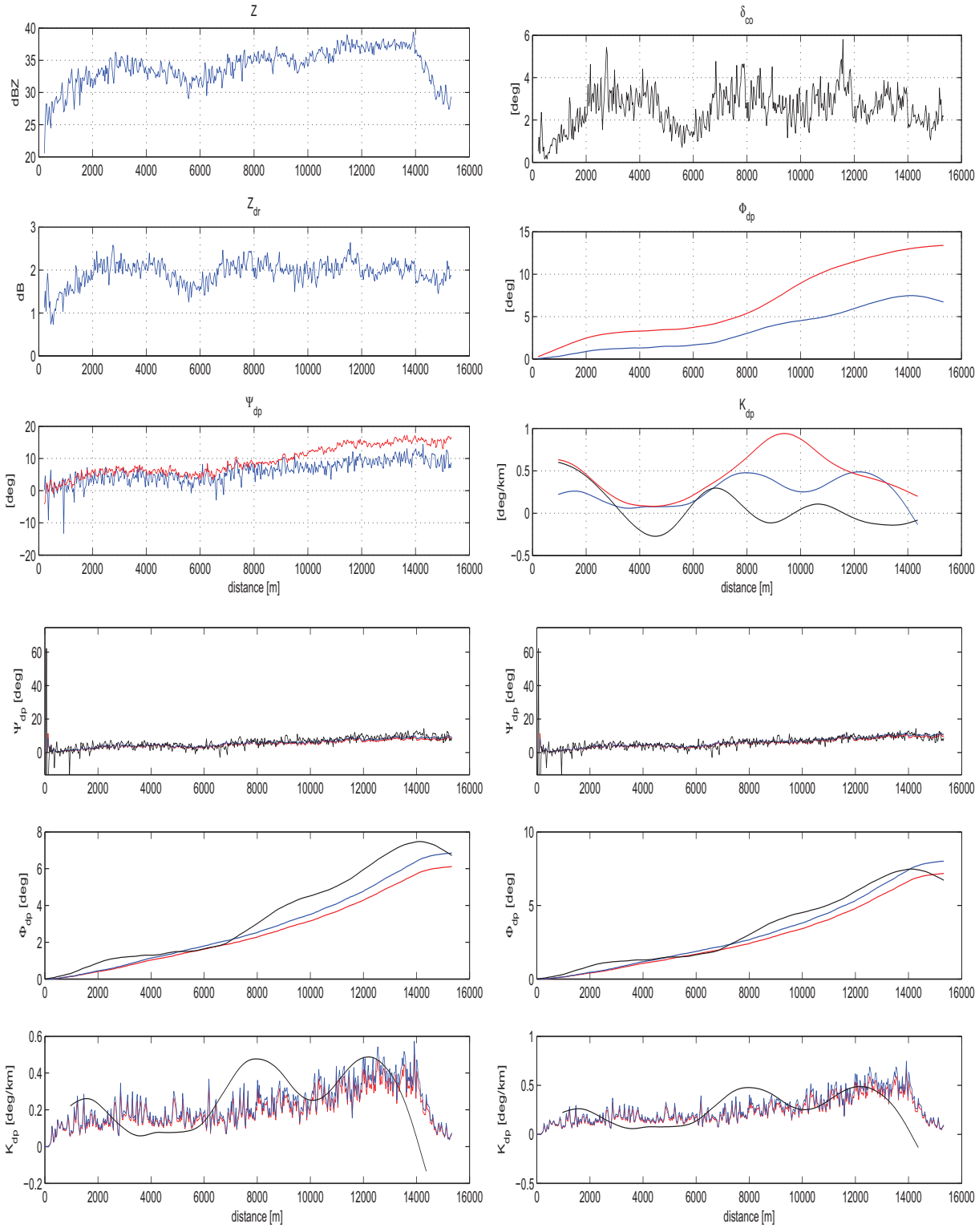

case:**2** sector:**140** This is the case of a sector of very low Z, with the exception of a raincell at 6-10km. There is very good agreement between the time domain and spectral polarimetry estimation. There is also good agreement in the assessment, especially after the attenuation correction where there is agreement on the value that the phase assumes after the 'jump'. It is also noticed that the pronounced inhomogeneity around 6km results in considerable $\bar{K}_{dp}^{\delta_{co}}$ bias.

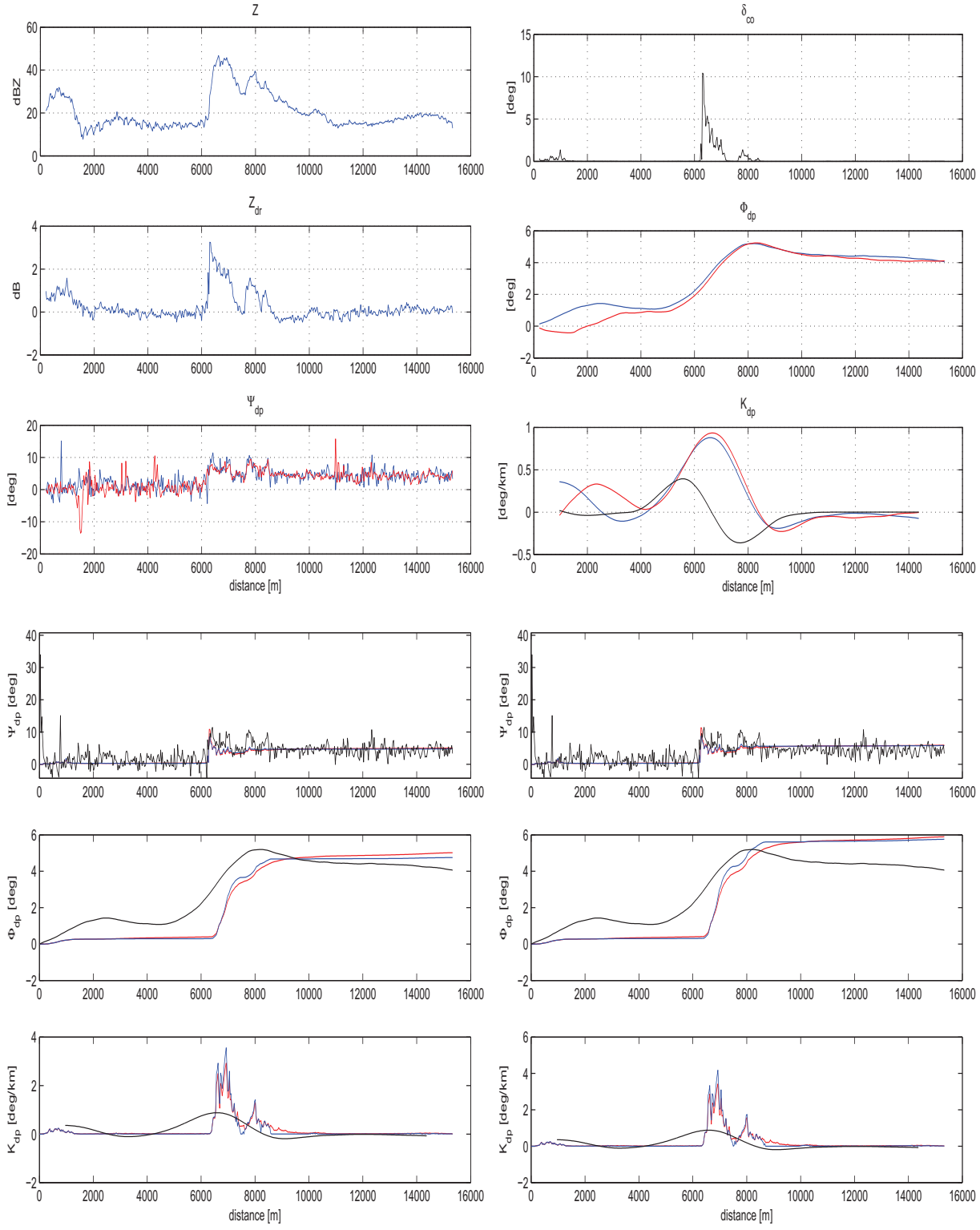

case:**2** sector:**220** This case is similar to the previous, but even more pronounced. If no δ_{co} removal had taken place, its bias on K_{dp} and any resulting rain rate estimation would be severe.

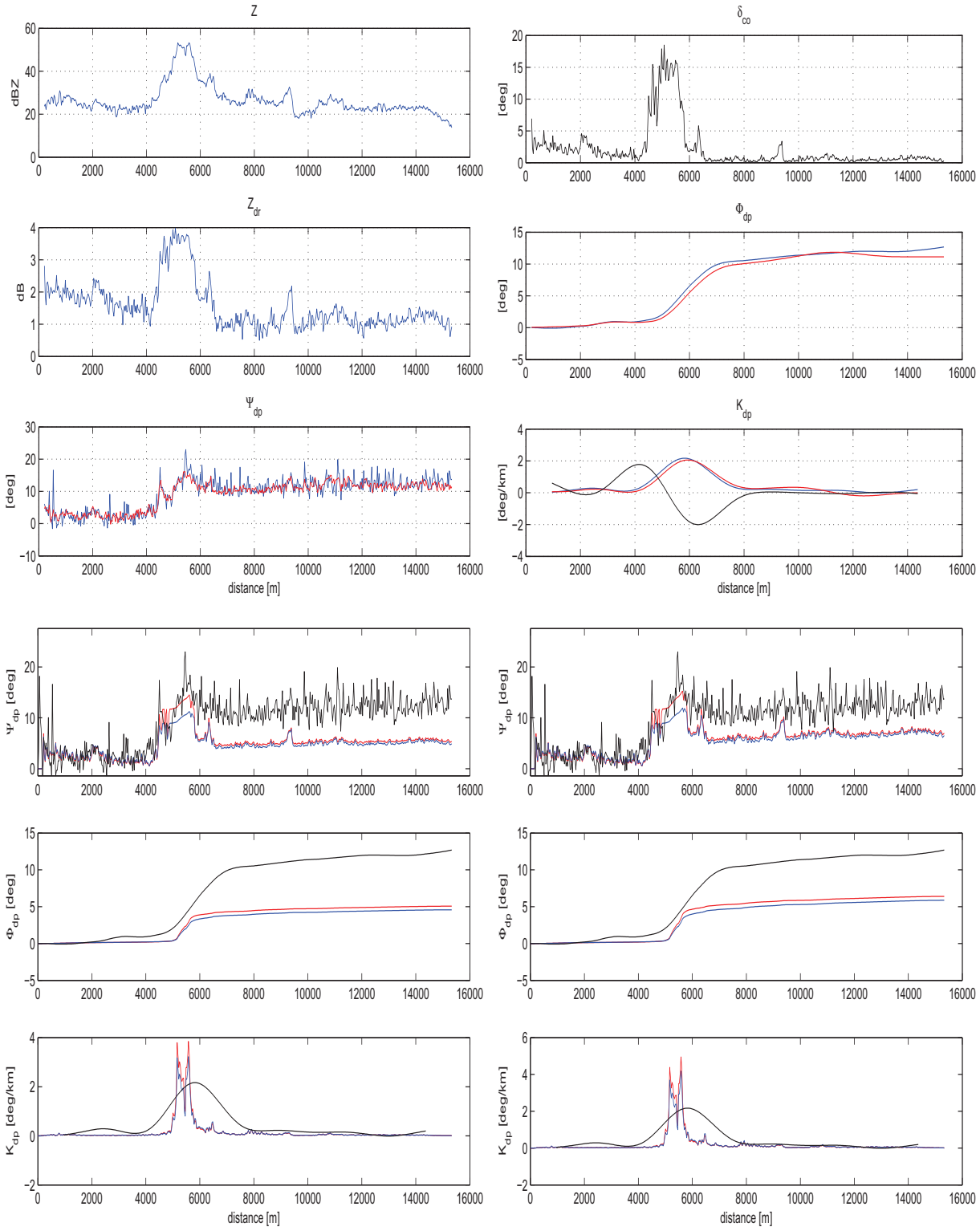

case:**2** sector:**320** Good agreement between the spectral polarimetry and assessment curves is observed for this sector. The phase wrap issue for time domain Ψ_{dp} appears at 8km.

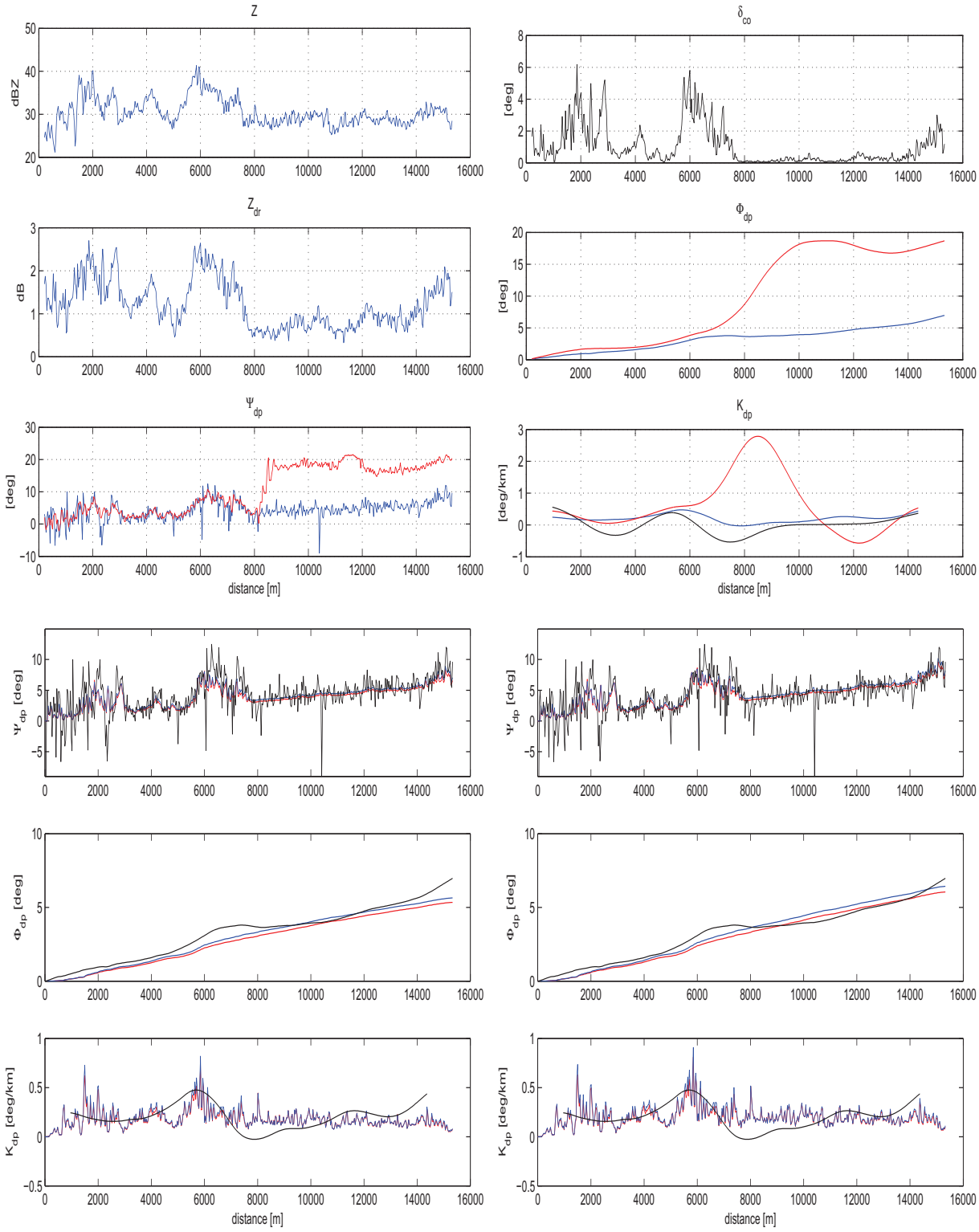

case:**3** sector:**20** In this case the time domain and spectral polarimetry Φ_{dp} and K_{dp} do not coincide due to a discrepancy in Ψ_{dp} around 5.5km.

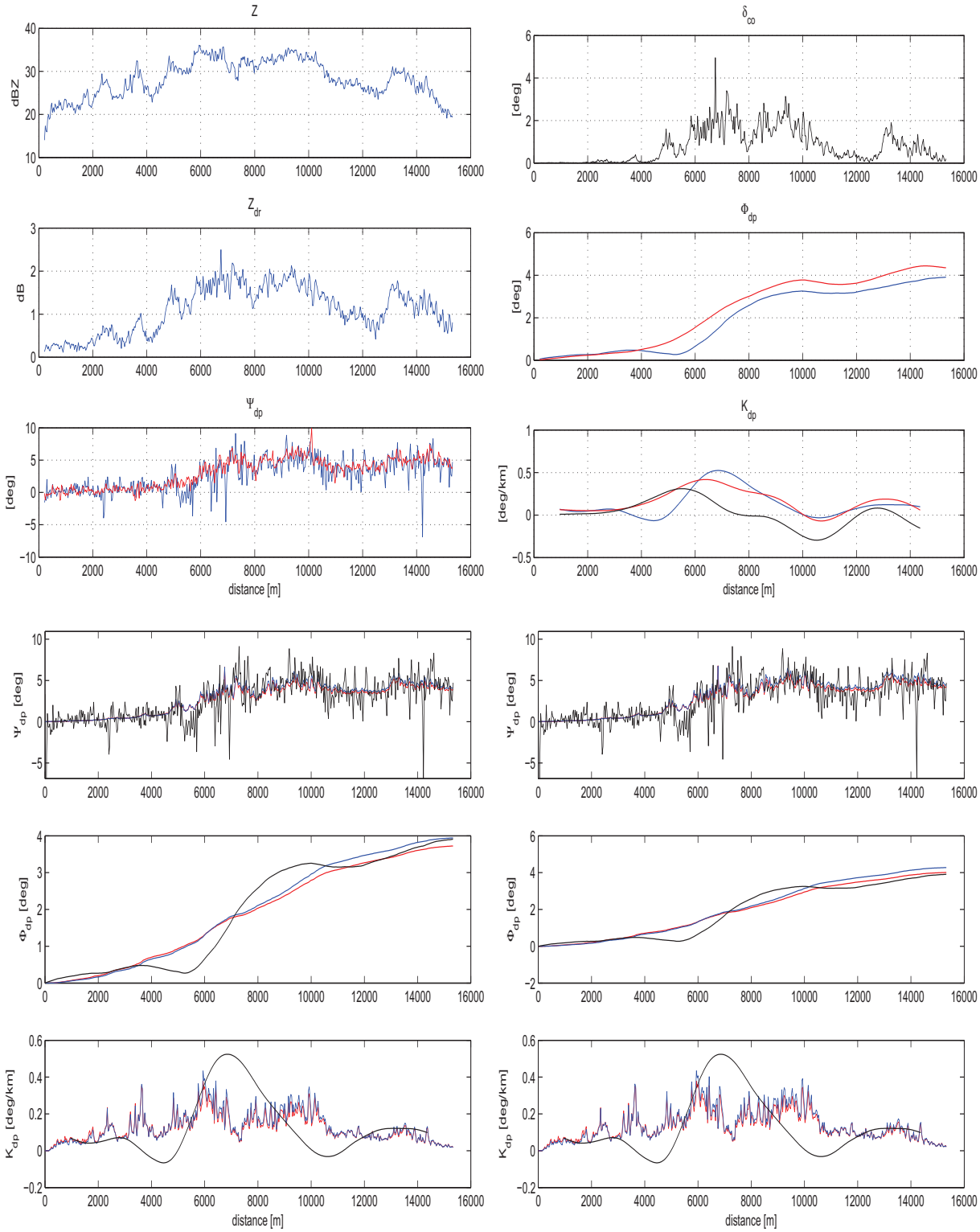

case:**3** sector:**180** Good agreement between the time domain, spectral polarimetry and assessment curves is observed. The disagreement of the TD and SP Φ_{dp} curves is limited only in the beginning (where there is a noisy spike in time domain Ψ_{dp}) and the end of the range where the reflectivity is too low (below 20dBZ) so the signal to noise ratio deteriorates which affects Ψ_{dp} estimation. It is noticed, however, that the spectral polarimetric processing has successfully removed the spurious peak present in the time domain, and is more robust against SNR deterioration.

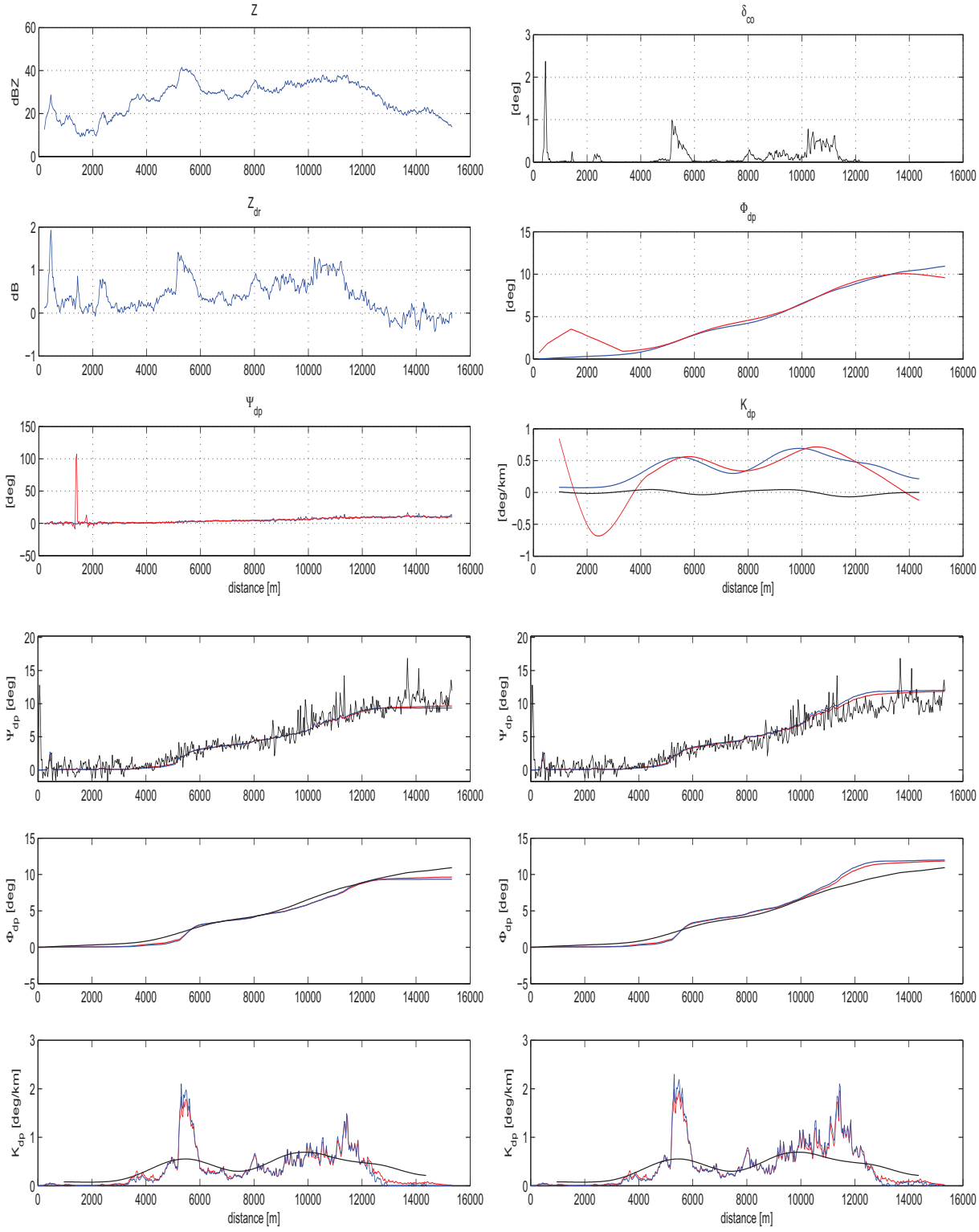

case:**3** sector:**300** Another sector where good agreement is observed. Regarding assessment, the K_{dp} curves are more difficult to be compared due to their different quality: the assessed K_{dp} is per rangebin, which is fictitious. By observing the range of values over which they vary locally their agreement becomes more obvious, especially after the attenuation correction for the 10-14km part. It is noticed that at 5km $\bar{K}_{dp}^{\delta_{co}}$ would result in 100% relative error due to the local Z_{dr} inhomogeneity.

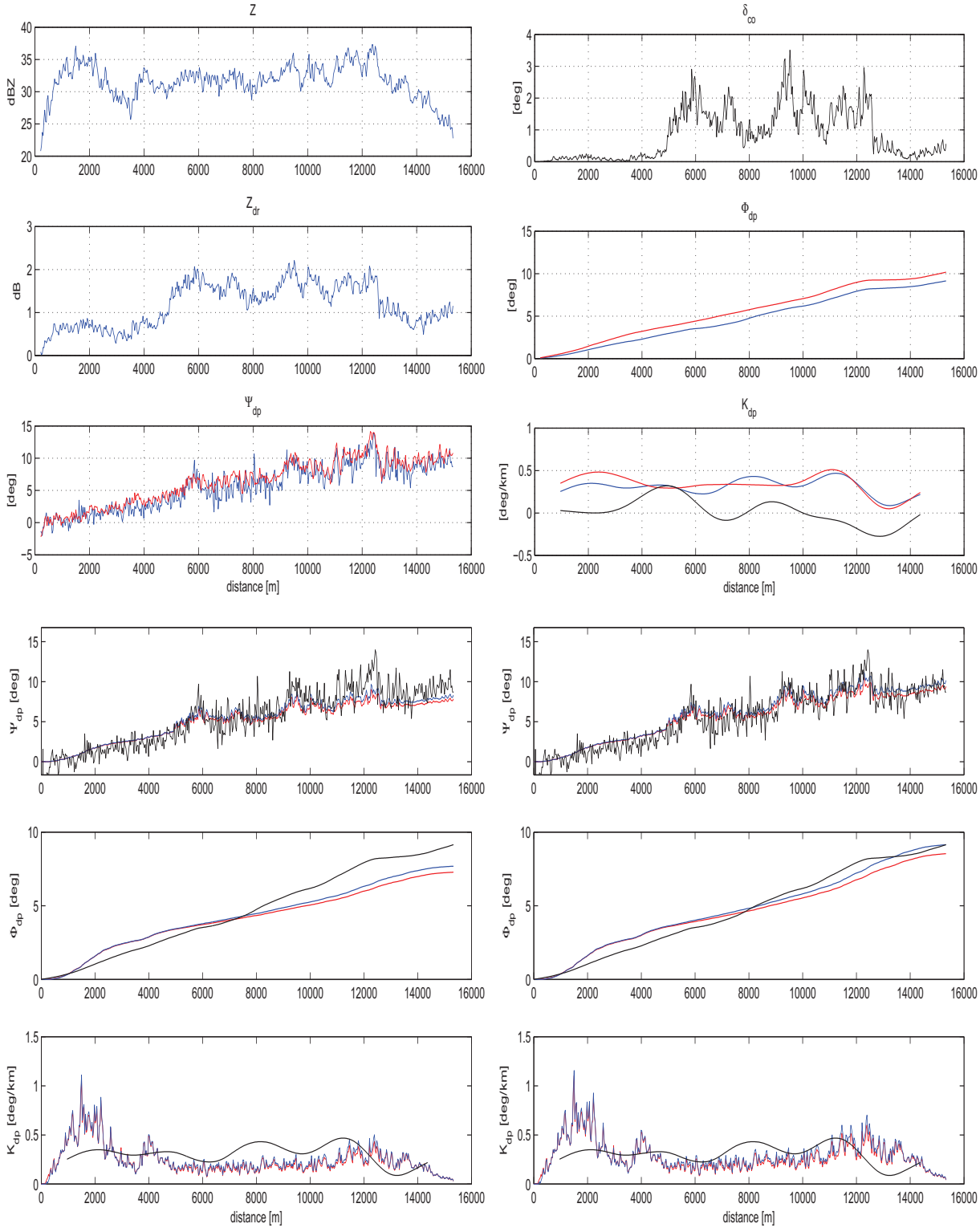

case:**3** sector:**340** This is a sector similar to the previous giving similar, consistent results.

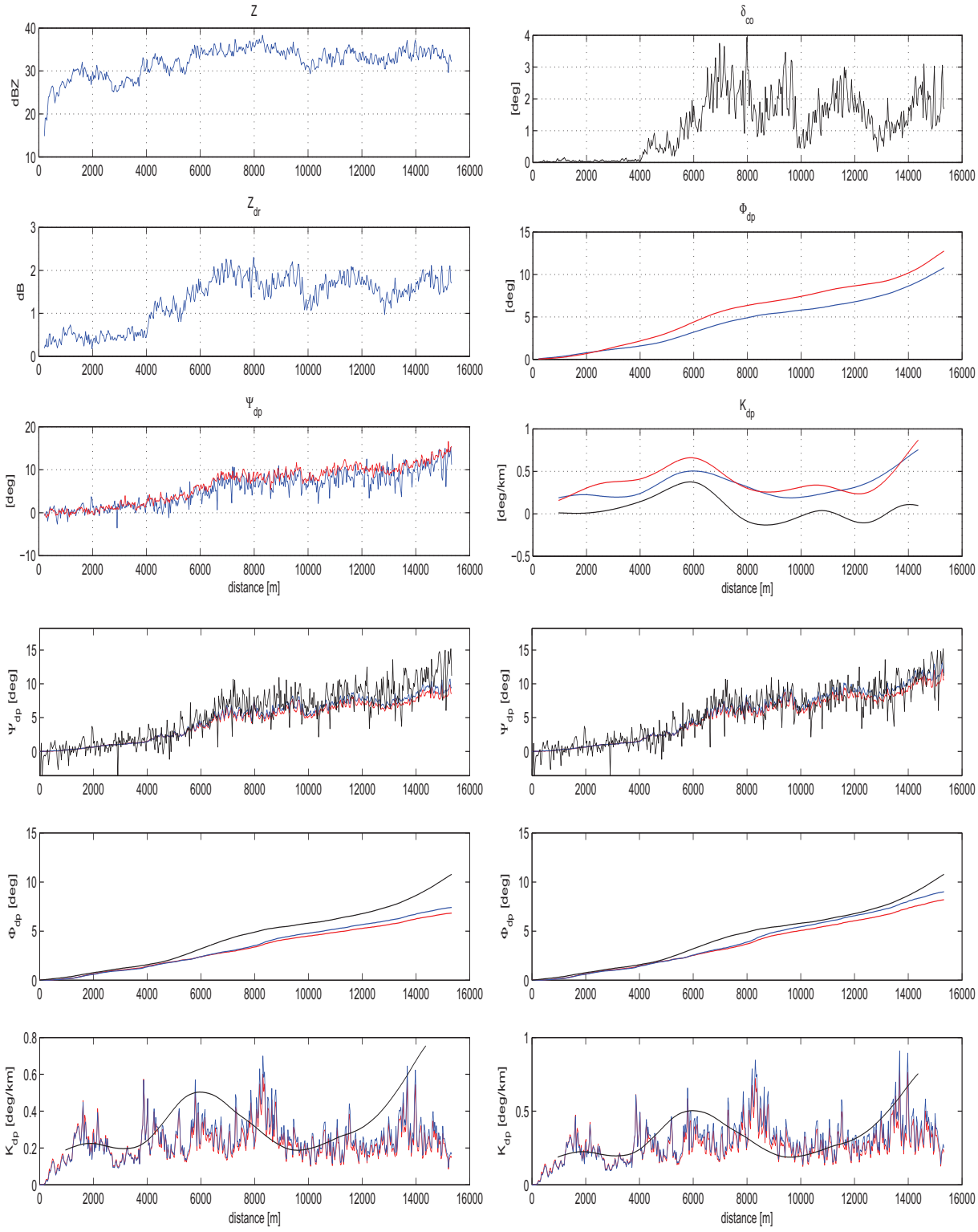

case:**5** sector:**20** This sector presents pronounced variations in the Z and Z_{dr} values, however there is very good agreement in the assessment. In this case the phase wrap issue for the time domain Ψ_{dp} is left untreated in order to illustrate it.

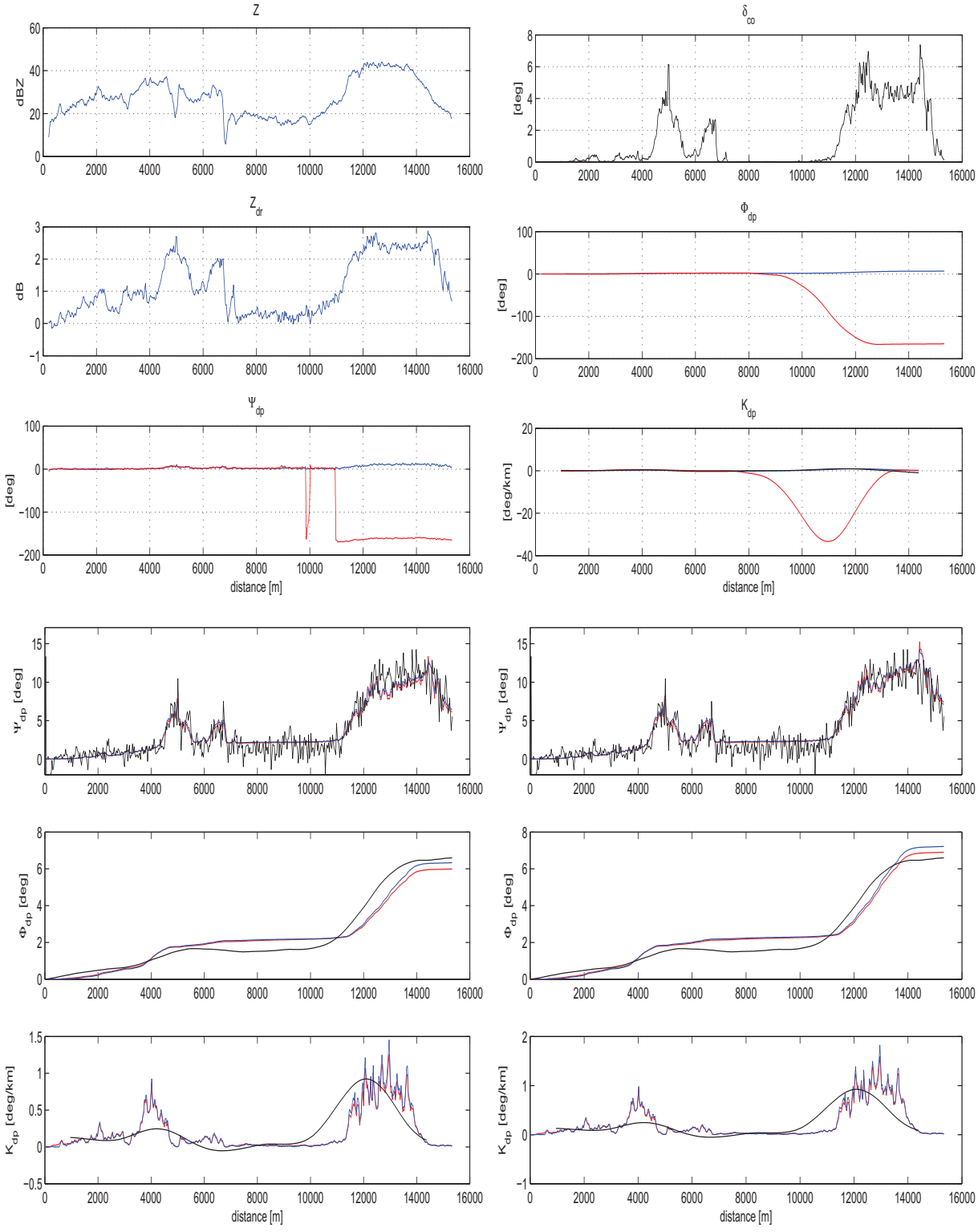

case:**5** sector:**340** In this sector the reflectivity peaks a little over 50dBZ, one of the highest values observed by IDRA. Consequently, K_{dp} also peaks at 4.6deg/km. It is noticed that the attenuation correction results in severe disagreement after 14km. This is because the correction factor is proportional to Φ_{dp}, which is particularly high in this case. An small error in the actual value of the attenuation correction factors α and β for Z and Z_{dr} respectively, would be amplified. As it has been mentioned, these factors are indeed variable (mostly on the temperature). It is believed that it would be useful to study this case so that the limitations and assumptions of the attenuation correction scheme become more clear.

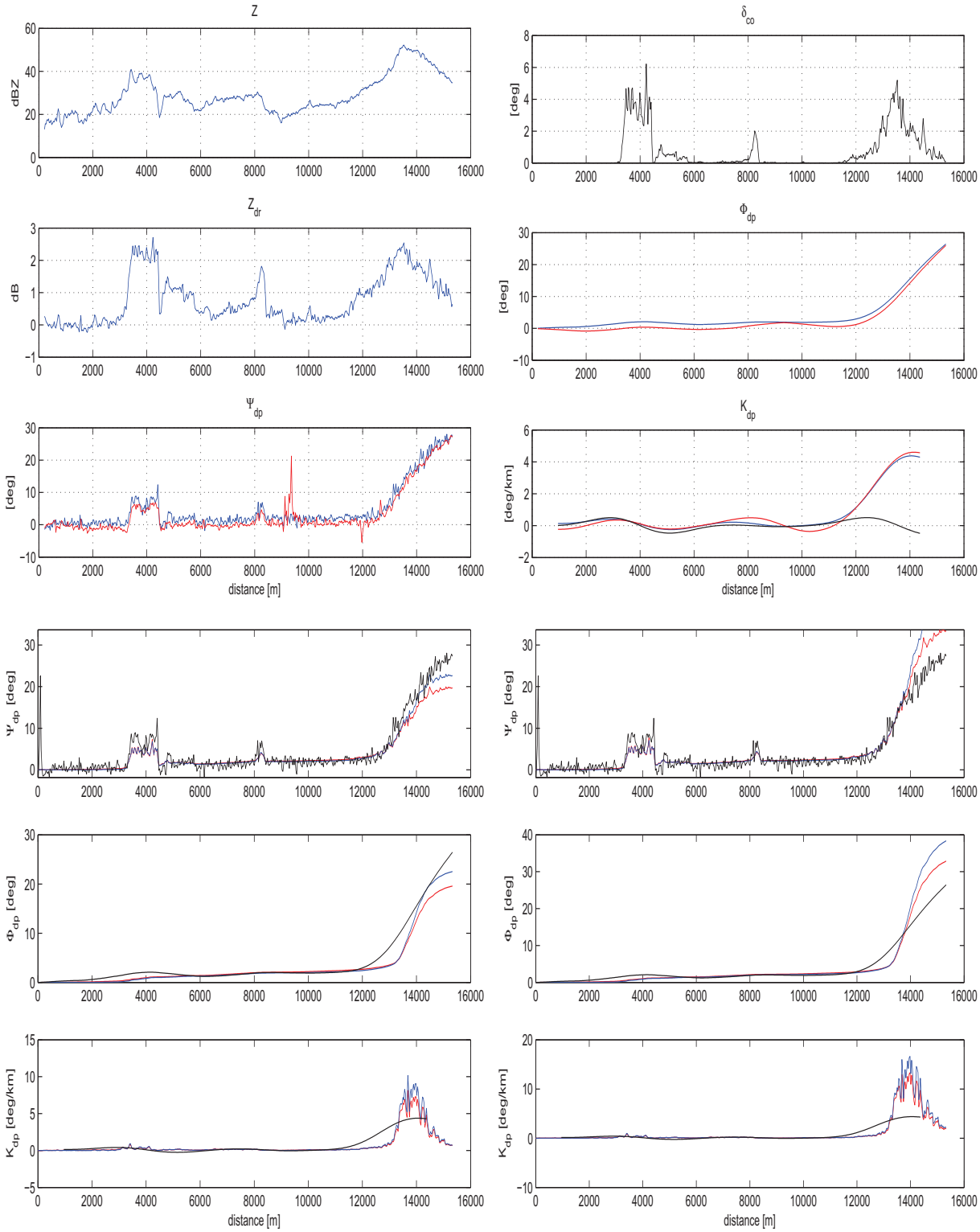

case:**6** sector:**100** In this case the good agreement in the assessment is distorted by the very noisy part of the estimated Ψ_{dp} which affects Φ_{dp}. Similar behaviour has been in some other sectors as well, characterized by very low reflectivity near the range end and Ψ_{dp}, both time domain and spectral polarimetric, that is noisy. It is suggested that an additional smoothing routine be used that deals with such large scale (above 1km) noisy interferences, or revise the Ψ_{dp} estimation routines for possible improvement. It is also mentioned that over the 9-13km segment the $\bar{K}_{dp}^{\delta_{co}}$ is equal or even larger than the estimated K_{dp} itself.

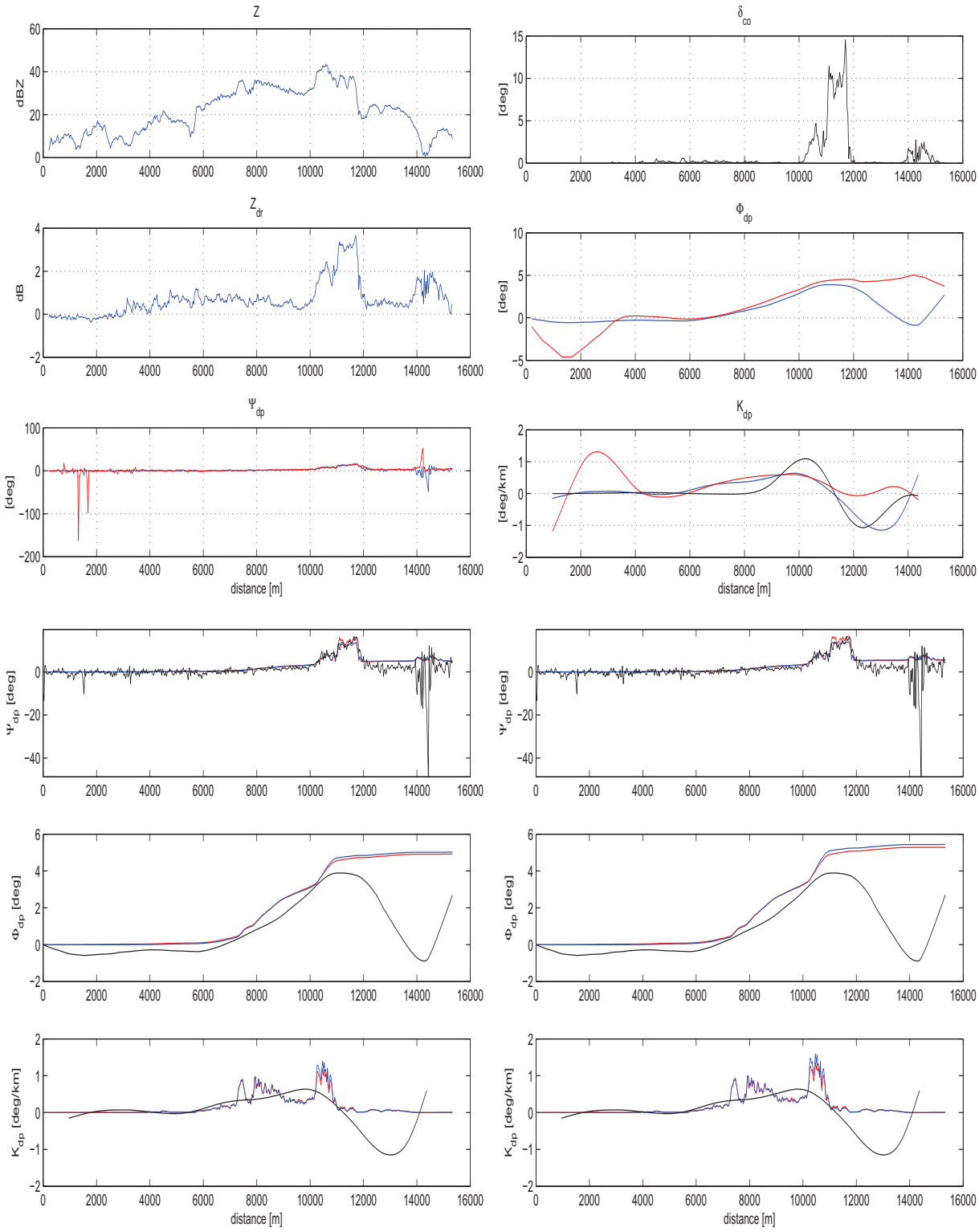

case:**7** sector:**240** In this case the spectral polarimetric Ψ_{dp} profile deteriorate when the reflectivity progressively falls below 20dBZ. In such a case, the assessment curves are more accurate for the problematic region.

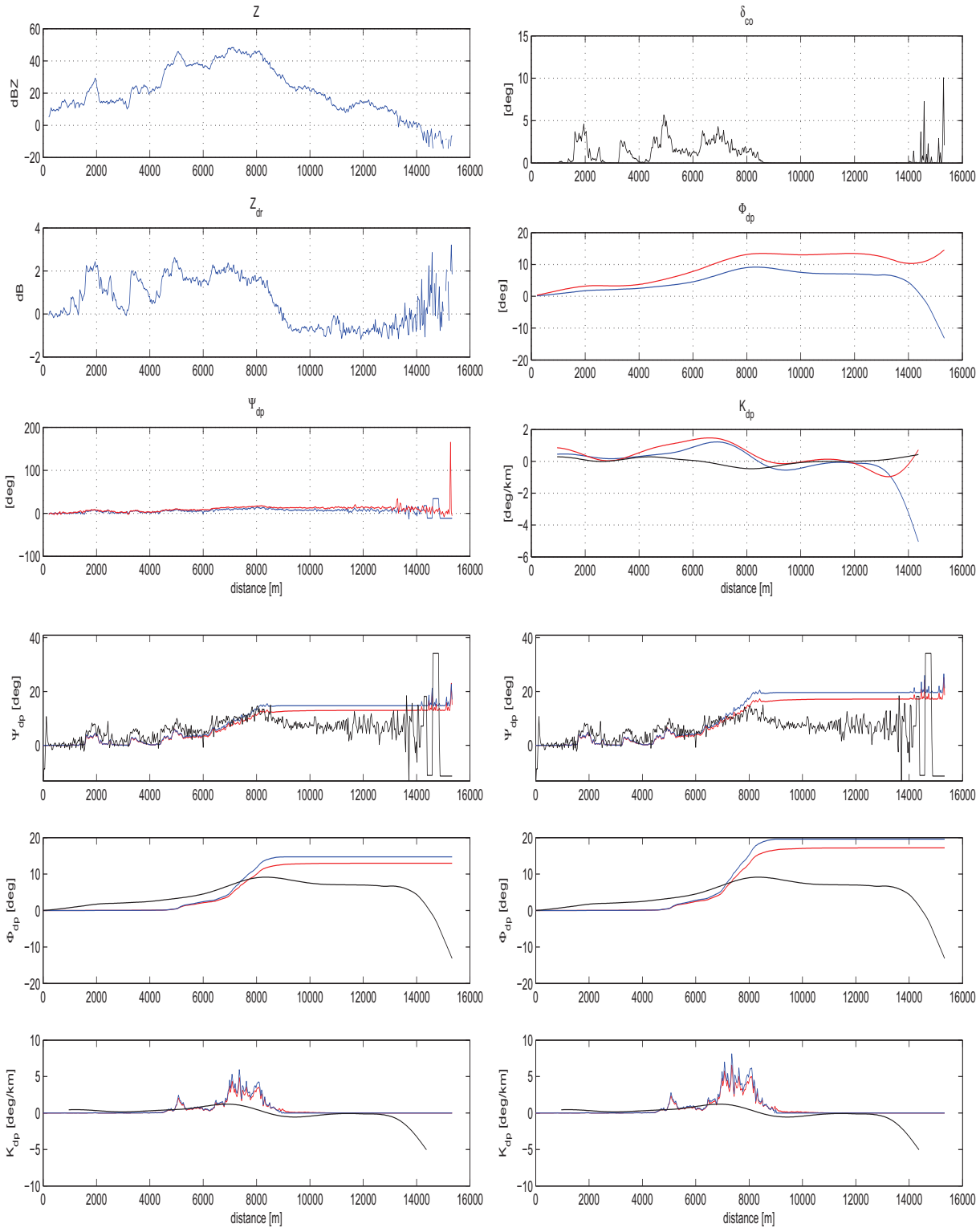

case:**8** sector:**290** This is a case of very low reflectivity and both estimation and asessement show that no K_{dp} estimation is possible. It is seen that the time domain Ψ_{dp} is severely affected, and also that the noisy Z_{dr} at 4km results in an artefact in δ_{co}.

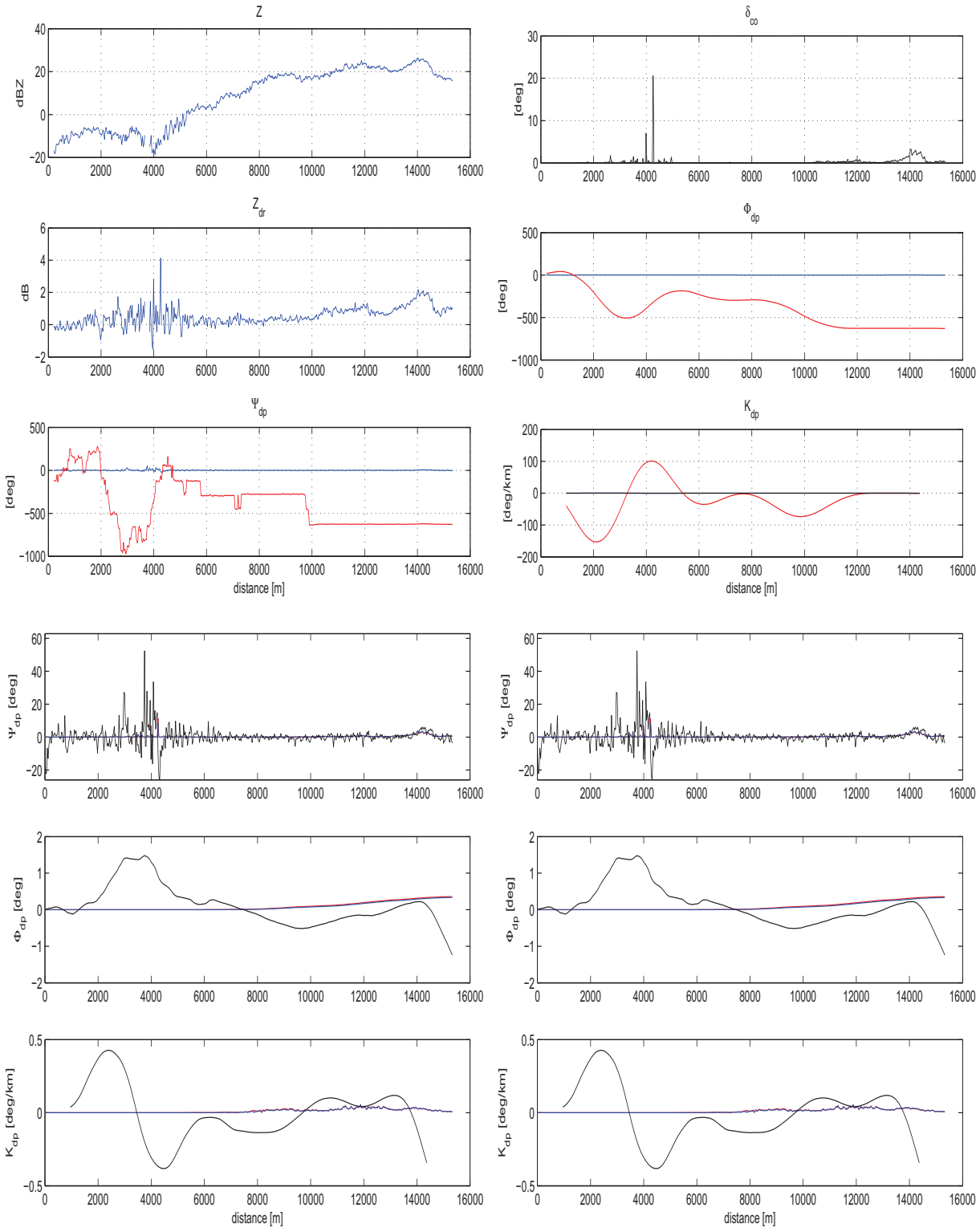

case:**9** sector:**0** This is a sector with intense rain cells near the radar. Therefore, the attenuation effects become obvious even after 2km. Attenuation correction improves considerably the agreement in the assessment, but still only up to 8km (the change in K_{dp} curves is particularly obvious). It is suggested that this case be studied more as it will increase our understanding of the limitations of the attenuation correction scheme. The high reflectivity is also combined by high values of differential reflectivity, so this a case where K_{dp} assumes considerable values over an extended range and the total Φ_{dp} phase excursion is one of the largest observed. After 12km, it is seen that the Ψ_{dp} profiles start to decrease which is not expected to occur; when K_{dp} is close to zero, the Ψ_{dp} profiles sould remain on the same level. This is an issue that has been observed in general, that is when the reflectivity is below 20dBZ the deterioration in SNR affects the Ψ_{dp} profiles in this way.

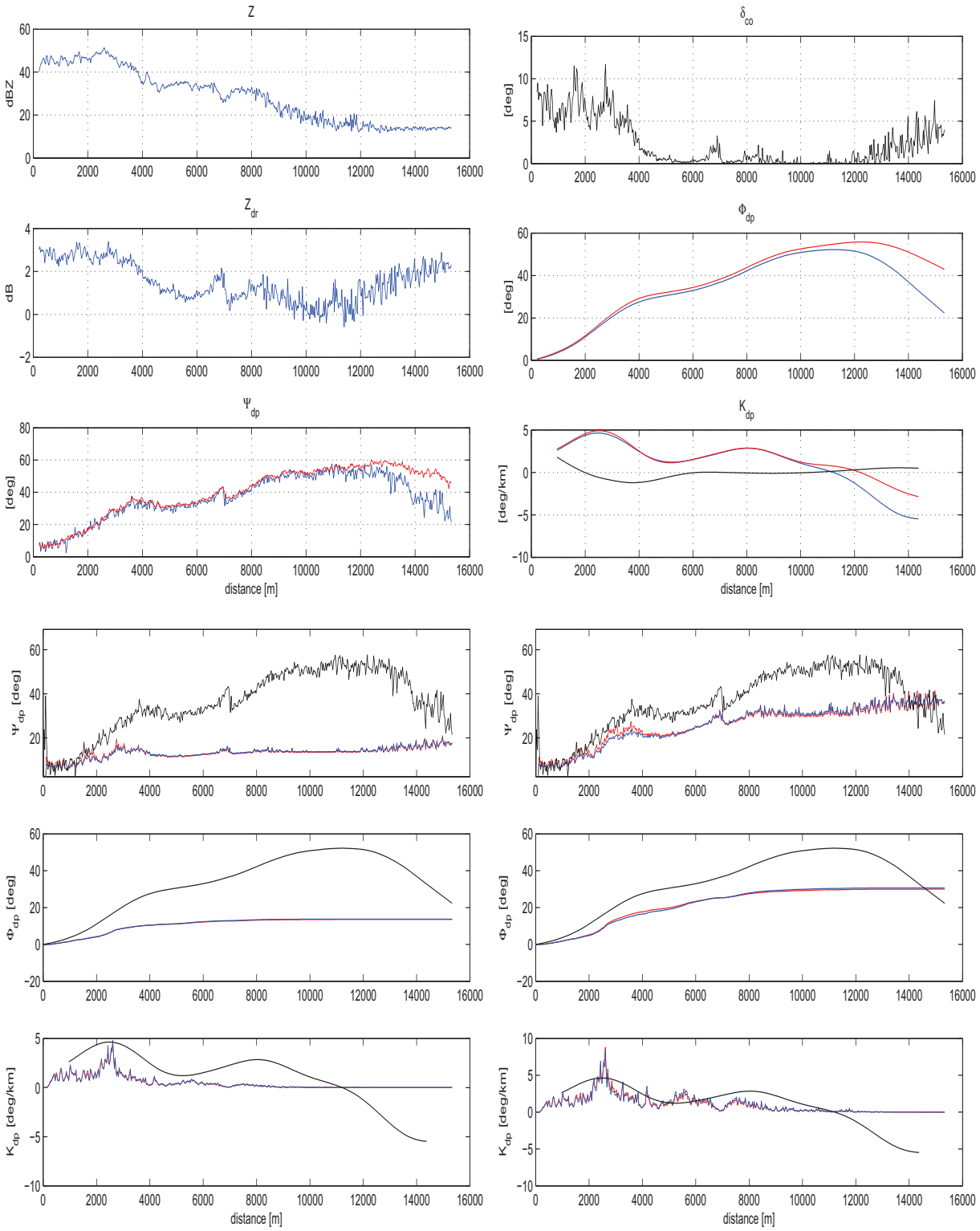

case:**9** sector:**100** This is a very interesting case in which although Z remains too low after 4km, the same does not apply to Z_{dr}. The estimated Ψ_{dp} curves appear to be non-monotonous, with two obvious negative 'bumps' between 6 and 10km, and another one between 11 and 13km. Having no reason to assume that they are due to a fault in the estimation processing, they have to be due to δ_{co} presence. However, they also appear in the Φ_{dp} profiles, which means that they were not successfuly removed. Since δ_{co} is expected to be positive, only positive 'bumps' may occur. The only logical conclusion is that there are no negative 'bumps', but **positive** 'bumps' in the remaining range segments: 2-6km, 7.5-9km, 9-10.5km and 12-16km. This is an indication that the simple $\delta_{co}(Z_{dr})$ removal scheme is insufficient in this case; perhaps a $\delta_{co}(Z, Z_{dr})$ relationship would be more appropriate. Due to incorrect Φ_{dp} profiles, the estimated K_{dp} is also erroneous (around the negative values).

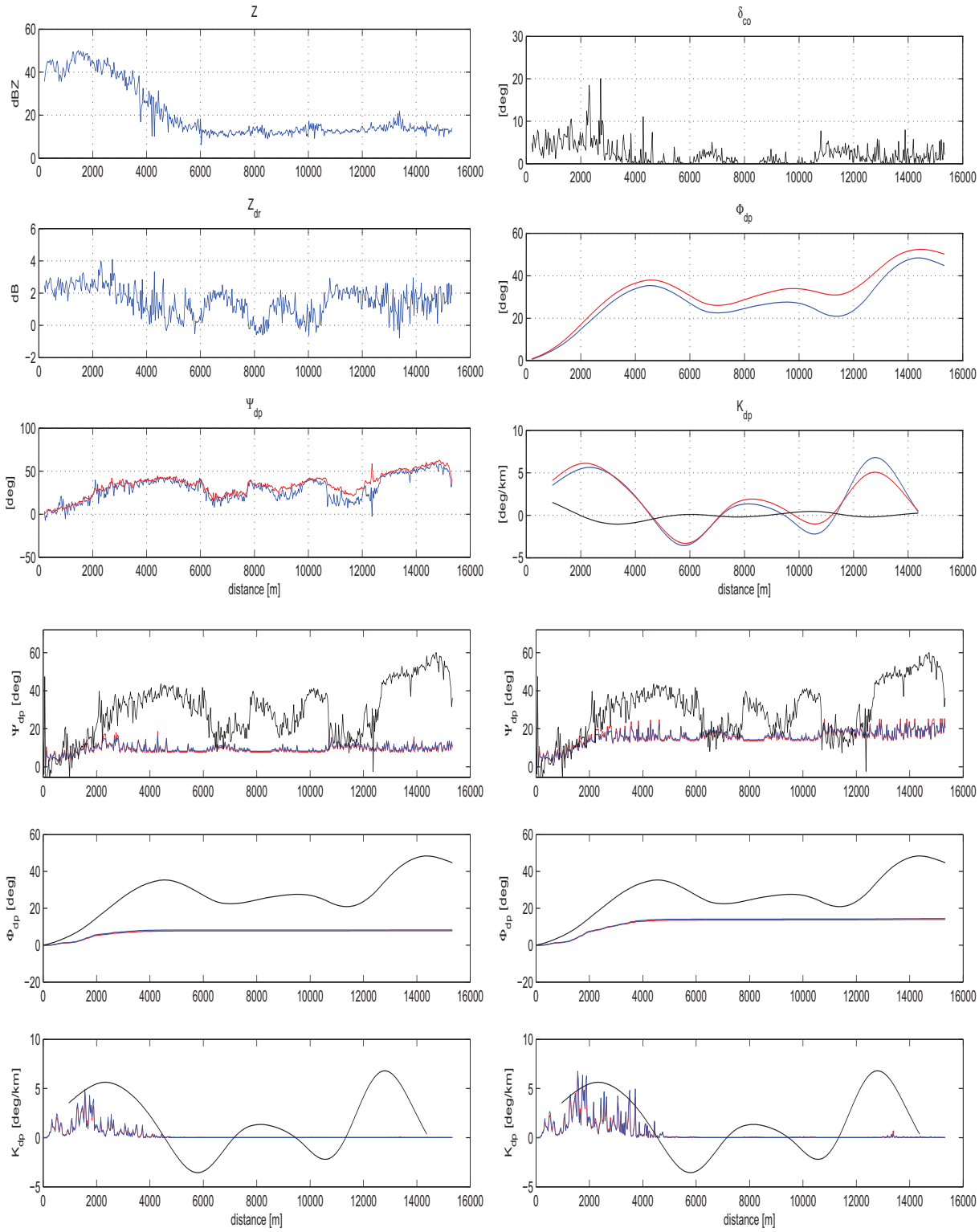

case:**9** sector:**160** This case is similar to the previous one, in that the Ψ_{dp} profiles become faulty after 7km.

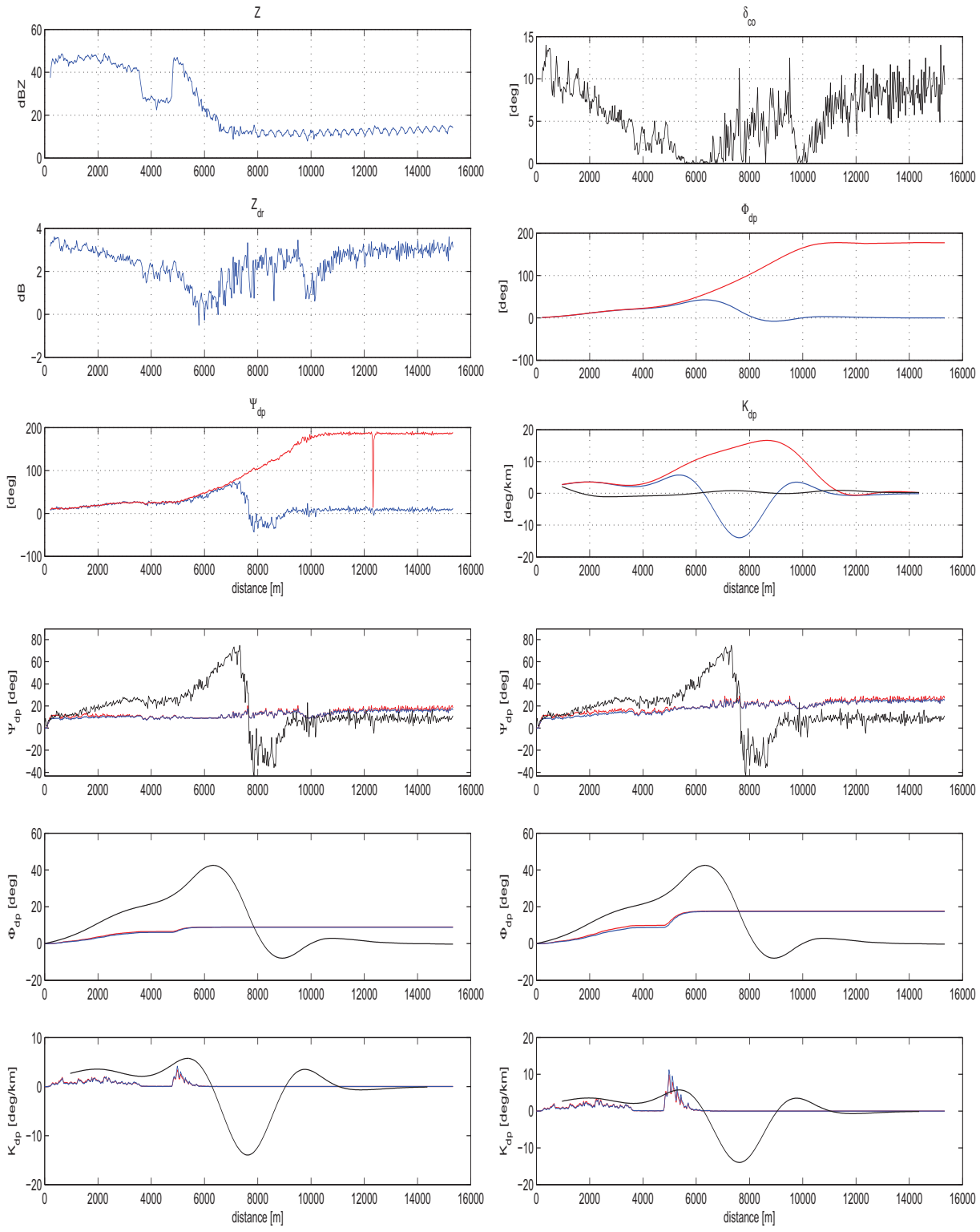

case:**10** sector:**260** In this case, the attenuation correction did result in improvement for the assessment curves (the difference in the Φ_{dp} values at end rangebin decreased from 4.5 to 3degrees) there is still not complete agreement (about 30% relative error). However, this does not imply that the estimation is erroneous. Probably this occurred for the assessment procedure, as it involves many assumptions. It is mentioned again that the assessment curves should not be viewed as a reference, but rather as the expected values. For this case, no safe conclusion can be drawn from the fact that they are not in close agreement with the estimation; instead, it is more important to consider the overall shape of the curves (where there is agreement) and the relative improvement that occured after the attenuation correction.

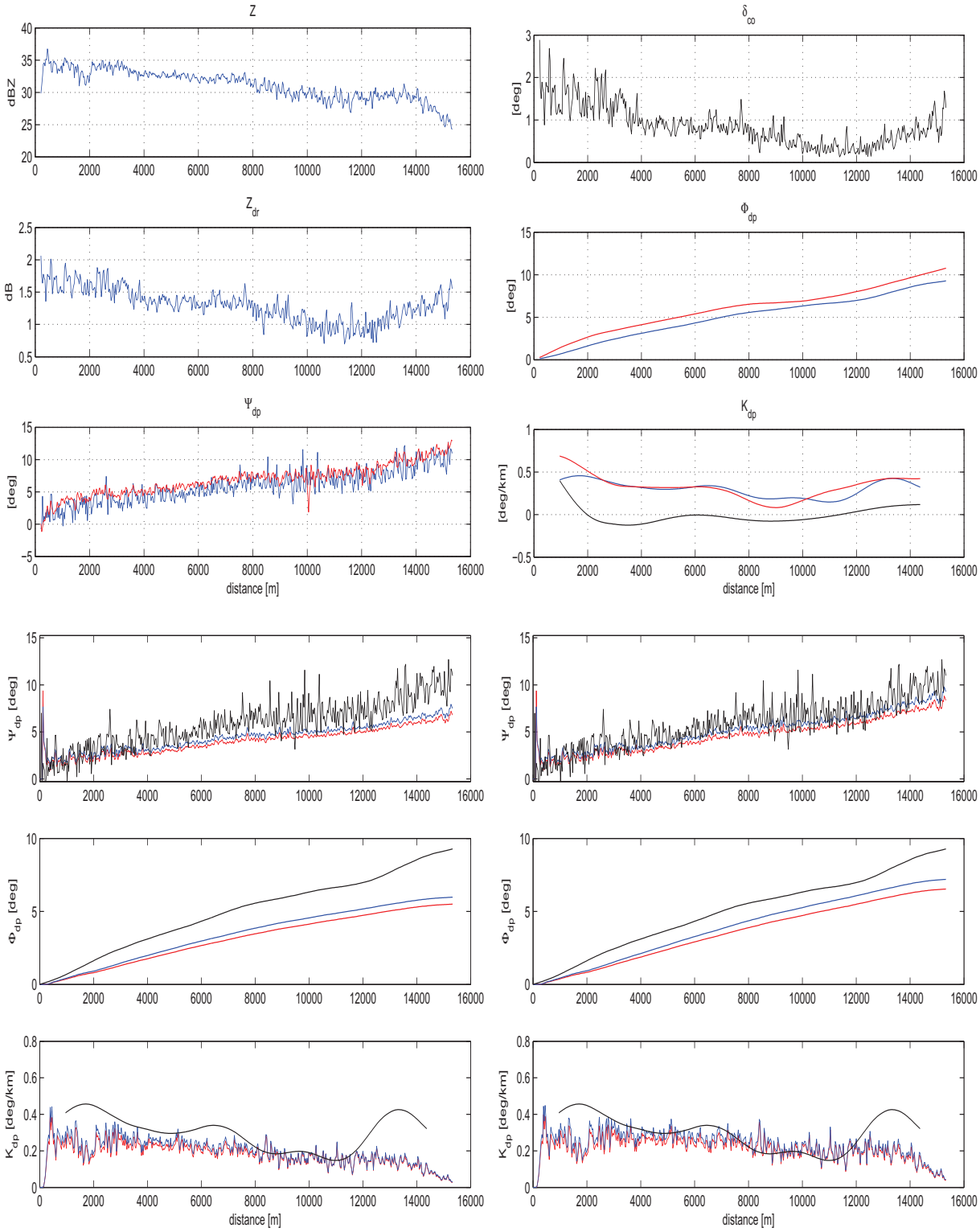

case:**10** sector:**300** In this case the attenuation correction results in worse agreement for the assessment in the region after 10km. Since the Ψ_{dp} time domain and spectral polarimetry profiles agree very well, the fault lies rather within the assessment procedure; in particularly it is believed that in this case overcompensation in the attenuation correction took place.

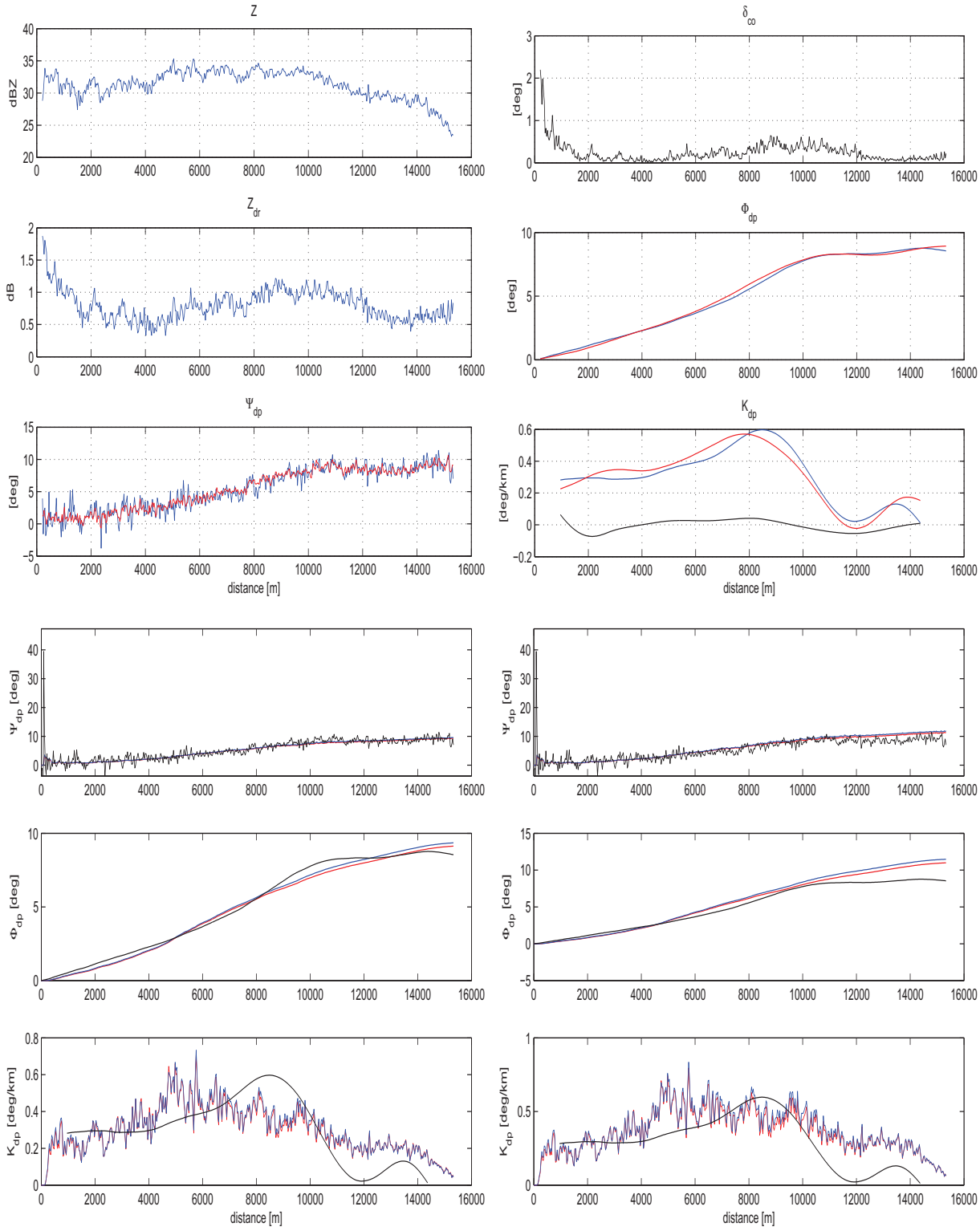

Appendix B

The issue of Z_{dr}

Although there is confidence in the correctness of measurement of Z and Z_{dr}, there is a problematic condition that affects Z_{dr}: distortion lines appear in some sectors as apparent on the PPI (Fig. B.1). At the moment, it is not known with certainty the cause of this distortion, however the safety metallic fence at the top of the Cabauw tower where IDRA is located is suspected. The problematic sectors may change from PPI to PPI (Fig. B.2). According to Fig. B1-2, it seems that the location of the problematic sectors is rather stable, and it is the intensity of the distortion effect per sector that varies. In the case shown, there is only 1 hour time difference between the two PPI; if PPI from different rain events are compared the distortion patterns are slightly less similar. In any case, no definite conclusion was reached for the behaviour of the distortion patterns. In practice, the distorted sectors are unusable as far as Z_{dr} is concerned. Until further measures are being taken, it is suggested that the Z_{dr} PPI be visually inspected in order to identify the problematic sectors and disregard them. Since they stand out at later processing stages (Fig. B.3), they can be easily detected as in our processing the Z and Z_{dr} range profiles are explicitly used. The rest of the sectors are believed to be dependable regarding Z_{dr}, although mitigation of the distorting condition is necessary in order to remove any doubts.

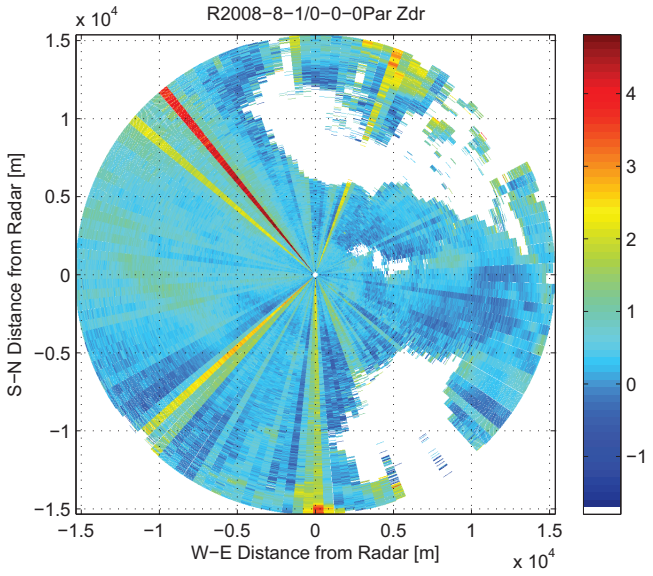

Figure B.1: A distortion line is apparent for the 310^0 sector.

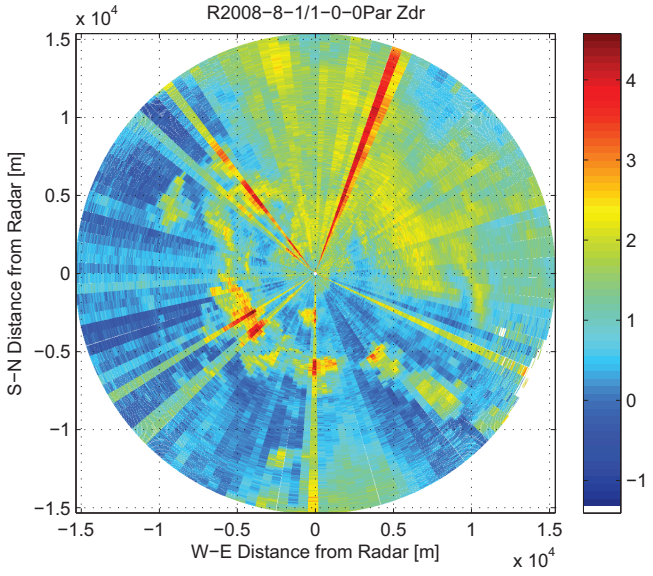

Figure B.2: A distortion line is now apparent about 20^0, while the 310^0 sector seems to be normal.

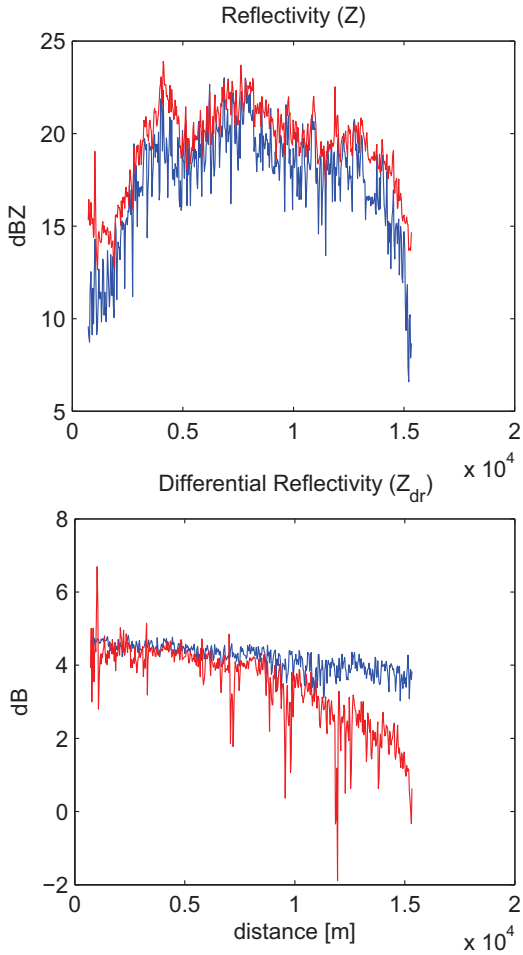

Figure B.3: The range profiles for the problematic sector of Fig. B.1. Z_{dr} takes abnormally large values while Z around 20dBZ. It is also noticed the obvious disagreement between time domain (red curve) and spectral polarimetry Z_{dr} (blue curve) which should not occur.

Appendix C

User guide for software and programs used

There are four types of IDRA datafiles:

1. **raw** (spectral) datafiles of extension .bin
2. **spectral polarimetric processed** datafiles of extension .Par.bin
3. **time domain processed** datafiles of extension .PPPar.bin
4. **noise** datafiles of extension .bin and beginning with 'N' (used for noise reduction and calibration)

The starting point is the raw and noise datafiles from which the processed datafiles are derived by using the IDRA offline processing tool Fig. C.1. The main options are:

- **Raw Data Processing**, which generates the .Par.bin from a given input raw and noise datafile (spectral polarimetric processed)
- **Pulse Pair Processing**, which generates the .PPPar.bin from a given input raw and noise datafile (time domain processed)
- **Data Visualization**, displays the radar observables as a PPI scan for a given processed datafile

The parameters **Clipping Level** and **Number of Doppler bins** are typically set to 10dB and 512 respectively. It is noted that on the left pane the temperature sensor values are shown along with additional information such as the sweep time and transmitted power of the current datafile[1]. On the right pane the individual PPI scans can be selected and saved as image files. A disk storage catalogue of all IDRA datafiles is contained in the file 'Disk content IDRA.doc' and the corresponding meteorological conditions in 'Relevant Meteorological Events IDRA.doc'. Once an event is chosen, the above processing steps have to take place for all raw datafiles corresponding to the desired time interval. At this point, the written Matlab routines may be used to derive

[1] this metadata is contained in the header of the raw datafiles

plots and results similar to the ones presented in this thesis. A detailed explanation of the function of each routine is included in each file. The main ones are:

- attenuation_correction.m, applies attenuation correction to Z and Z_{dr} profiles
- generate_dataset.m, generates a dataset of radar observables given a range for the gamma dsd parameters
- get_DSD.m, retrieves the dsd from a given Z, Z_{dr} profile
- getZ.m, used to read from .Par.bin and .PPPar.bin files
- Kdp_calc.m, performs K_{dp} estimation given a smoothed Φ_{dp} profile
- PhaseRangeProfile.m, performs weighting or averaging on the spectral Φ_{dp} in order to derive a Φ_{dp} range profile
- Phi_dp_inspector.m, computes and plots the Φ_{dp}
- PlotPhase_chris.m, is the first variation for Ψ_{dp} estimation
- PlotPhase_jordi.m, is the second variation for Ψ_{dp} estimation
- smooth1.m, smoothes Φ_{dp} range profiles
- myunwrap.m applies a custom phase uwrapping for the time domain Ψ_{dp}
- synthetic_profile.m, computes and plots the results according to the self-consistency or dsd retrieval assessment approach

The FIM simulation toolbox resides in the folder 'Scattering_Simulation' and should be included in the Matlab path, as it is called by some of the above routines. In the following, the sequence of commands used for the analysis of a certain case are given with comments on the most important variables as an example.

```
global sector case_study
sector=270;
case_study=3;
```

The `sector` variable defines the desired sector to be analyzed, in degrees. It is noticed that since the angular resolution of IDRA is about 2.5^o, when an arbitrary selection is made it will be approximated to the closest possible actual sector. This information can be viewed on the Matlab command window as output. For this example, the desired sector of 270^o is matched to the actual sector of azimuth 271.126^0. The `case_study` variable defines a specific raw data file and its associated processed data files as given in the `Phi_dp_inspector.m` file. In this case, the value of 3 corresponds to R2008-8-1_2-0-0.bin.

```
k=8;close all;[Psi1 Psi2 Psi3 Z_sp Zdr_sp Ldr_sp Z_td Zdr_td Ldr_td r
block TitlePlot]=Phi_dp_inspector(sector,10000,1,2,'no',case_study,k);
```

This command performs the calculations for the computation of Ψ_{dp} from an IDRA raw data file. The variable `k` denotes the number of near field rangebins

that will be omitted from the plots for better readability since the radar observables exhibit irrelevent values at this range. In this case the range profiles will be plotted from 8*30=240m. `Psi1` and `Psi2` are the spectral polarimetry (as computed from the raw data file) and time domain Ψ_{dp} respectively, while `Psi3` is the spectral polarimetry Ψ_{dp} as computed from the processed data file. The other output variables are the radar observables Z, Z_{dr} and L_{dr} along with some auxilliary ones. It is noticed that at this point the derived Ψ_{dp} are not correctly offset as δ_{co} is not available yet.

```
k=8;m=10;N=64;dco_coeff=[0.3719 2.8291];mode=3;
```
The variable `m` denotes the number of initial rangebins that will be disregarded from the Ψ_{dp} offset calculations. Typically, it is expected to be the same as `k`. However, an additional one is used as a degree of freedom for problematic cases. `dco_coeff` defines the parameters for the $\delta_{co}(Z_{dr})$ estimator, and `mode` the type of smoothing filter to be applied with `N` its extent in rangebins.

```
[Phi1 Phi2 Phi1s Phi2s Kdp1 Kdp2 Kdpbias]= Kdp_calc(Psi1,Psi2,Psi3,Z_sp,Zdr_sp,
Ldr_sp,Z_td,Zdr_td,Ldr_td,r,block,TitlePlot,k,m,N,dco_coeff,mode);
```
This command performs the K_{dp} calculation and the correct offsetting of Ψ_{dp} since δ_{co} is now available.

```
flag=0;
```
The variable `flag` is passed to the routines that are called two times (before and after attenuation correction) to indicate the actual processing stage. The values of 0 and 1 respectively correspond to before and after attenuation correction.

```
z_pre=10*log10(Z_sp(1:end,block));
```
This is the measured Z range profile, from the spectral polarimetry approach converted into the dB scale.
```
zdr_pre=10*log10(Zdr_sp(1:end,block));zdr_pre(isnan(zdr_pre))=0;
```
The same for Z_{dr}.

```
mu=1;[Do_dsd_pre Nw_dsd_pre Z_dsd_pre Zdr_dsd_pre]=get_DSD(z_pre,zdr_pre,mu,flag);
```
This command performs the dsd retrieval and outputs the gamma dsd parameters. As it seen, the value of μ has to be assumed.

```
Kdp_coeff=[0.0005 0.9751 0.3908];
dco_coeff=[0.3719 2.8291];
```
These are the self-consistency estimator relationships for K_{dp} and δ_{co}.

```
[Psidpdsd_pre Phidpdsd_pre Kdpdsd_pre dcodsd_pre Psidpsc_pre Phidpsc_pre
Kdpsc_pre dcosc_pre]= generate_profile(Nw_dsd_pre,Do_dsd_pre,mu*ones(1,512),
Psi1 ,Phi1s,Kdp1,Kdp_coeff,dco_coeff,flag);
```
At this point the dsd is retrieved and the self-consistency relationships are set, so this commands performs the computations for the assessment described in Chapter 6.

```
att_coeff=[0.25 0.02];
flag=1;
```
The attenuation parameters are defined and `flag` is set to indicate the attenu-

ation correction stage.

`[z_post zdr_post]=attenuation_correction(z_pre,zdr_pre,Phi1s,att_coeff);`
This command performs the attenuation correction for the Z and Z_{dr} profiles.

```
[Do_dsd_post Nw_dsd_post Z_dsd_post Zdr_dsd_post]=get_DSD(z_post,zdr_post,mu,flag);
[Psidpdsd_post Phidpdsd_post Kdpdsd_post dcodsd_post Psidpsc_post Phidpsc_post
Kdpsc_post dcosc_post]= generate_profile(Nw_dsd_post,Do_dsd_post,mu*ones(1,512),
Psi1,Phi1s,Kdp1,Kdp_coeff,dco_coeff,flag);
```
The same assessment routines are carried out, with attenuation correction included as contrasted to before.

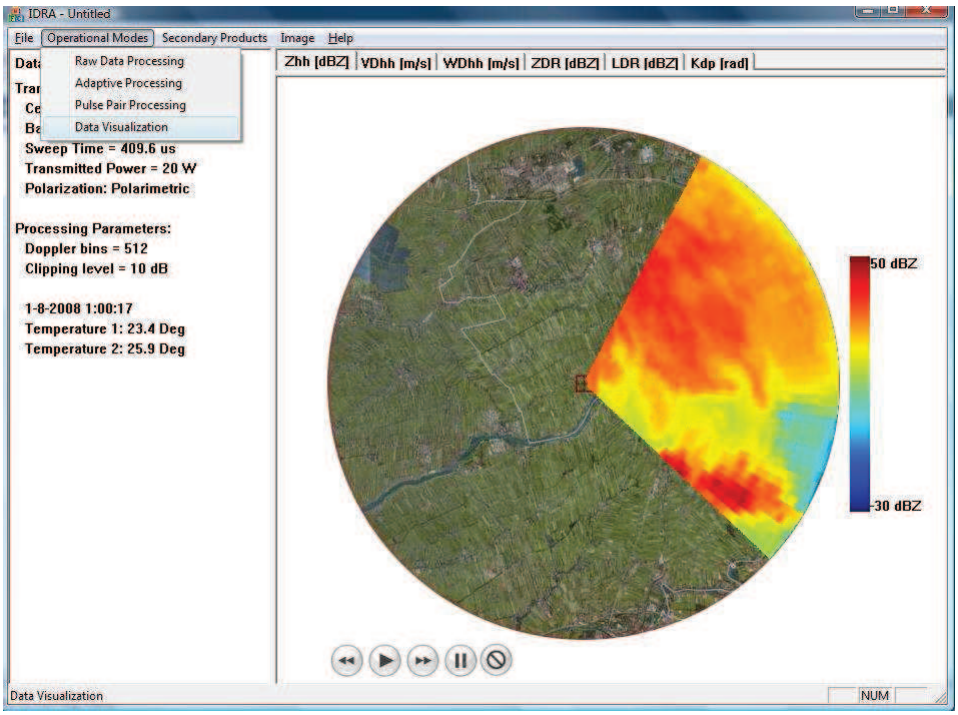

Figure C.1: The IDRA offline processing tool during visualization of the reflectivity PPI of 1 Aug 2008, 01:00:17 UTC.

Bibliography

[1] J. Figueras i Ventura, H.W.J. Russchenberg, IDRA: a new instrument for drizzle monitoring, International Geoscience and Remote Sensing Symposium, IGARSS 2007, Barcelona 23-27 July 07.

[2] Ventura, J.F.; Russchenberg, H.W.J., "IDRA: IRCTR Drizzle Radar," Radar Conference, 2006. EuRAD 2006. 3rd European , vol., no., pp.174-177, 13-15 Sept. 2006

[3] J. Figueras i Ventura, "Design of a High Resolution X-band Doppler Polarimetric Weather Radar", Ph.D. thesis, Delft University of Technology, November 2009

[4] Lohmann, U. and Feichter, J.: Global indirect aerosol effects: a review, Atmos. Chem. Phys., 5, 715-737, 2005.

[5] Polarimetric Doppler weather radar: principles and applications: V.N. Bringi and V. Chandrasekar. Cambridge University Press, ISBN:9780521623841 .

[6] Oguchi, T. Electromagnetic wave propagation and scattering in rain and other hydrometeors. IEEE Proc., 71: 10291078, 1983.

[7] Zrnić, D., and A. Ryzhkov, 1996: Advantages of Rain Measurements Using Specific Differential Phase. J. Atmos. Oceanic Technol., 13, 454-464.

[8] Ryzhkov, A., and D. Zrnic', 1996: Assessment of Rainfall Measurement That Uses Specific Differential Phase. J. Appl. Meteor., 35, 20802090.

[9] Ulbrich, C.W. Natural variations in the analytical form of the raindrop-size distribution. J. Climate Appl. Meteor., 22: 17641775, 1983.

[10] Russchenberg, HWJ, Spek, L, Moisseev, D, Unal, CMH, Dufournet, Y Chandrasekar, V (2008): On the use of spectral polarimetry to observe ice cloud microphysics with radar. Precipitation: Advances in Measurement, Estimation and Prediction (pp. 285–312), Springer Berlin Heidelberg

[11] Marchuk, V.; Yanovsky, F.J., "Use of spectral differential reflectivity at remote sensing of precipitation," Microwaves, Radar and Remote Sensing Symposium, 2008. MRRS 2008 , vol., no., pp.182-185, 22-24 Sept. 2008

[12] Unal, C.M.H., and D.N. Moisseev, 2004: Combined Doppler and Polarimetric Radar Measurements: Correction for Spectrum Aliasing and Nonsimultaneous Polarimetric Measurements. J. Atmos. Oceanic Technol., 21, 443-456.

[13] Unal, C.M.H., Spectral Polarimetric Radar Clutter Suppression to Enhance Atmospheric Echoes, Journal of Atmospheric and Oceanic Technology 2009 26:9, 1781-1797

[14] Gorgucci, E., G. Scarchilli, and V. Chandrasekar, 2000: Practical Aspects of Radar Rainfall Estimation Using Specific Differential Propagation Phase. J. Appl. Meteor., 39, 945955.

[15] Gorgucci, E., G. Scarchilli, and V. Chandrasekar, 1999: Specific Differential Phase Estimation in the Presence of Nonuniform Rainfall Medium along the Path. J. Atmos. Oceanic Technol., 16, 16901697.

[16] Scarchilli G., E. Gorgucci, V. Chandrasekar, and A. Dobaie, 1996: Self-consistency of polarization diversity measurement of rainfall. IEEE Trans. Geosci. Remote Sens., 34, 22–26.

[17] Holt, A. R., Uzunoglu, N. K., and Evans, B. G.: An Integral Solution to the Scattering of Electromagnetic Radiation by Dielectric Spheroids and Ellipsoids, IEEE T. Antennas Propag., AP-26, 706712, 1978.

[18] H.R. Pruppacher and K.V. Beard, "A wind tunnel investigation of the internal circulation and shape of water drops falling at terminal velocity in air", Quart. J.R. Met. Soc., vol. 96, 1970.

[19] Sauvageot, H., and J.P. Lacaux, 1995: The Shape of Averaged Drop Size Distributions. J. Atmos. Sci., 52, 10701083.